Charles University in Prague
Faculty of Mathematics and Physics

MASTER THESIS

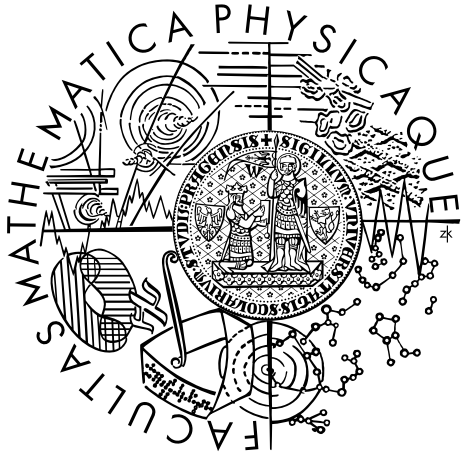

Lukáš Nádvorník

Electronic structure of graphene-based materials

Institute of Physics of Charles University

Supervisor of the master thesis: RNDr. Milan Orlita, Ph.D.
Study programme: Physics
Specialization: Optics and Optoelectronics

Prague 2011

I cordially thanks my supervisor dr. Milan Orlita and my advisor dr. Karel Výborný for their irreplaceable and continuous leadership, the setting and holding the course and their patient and friendly support. I also acknowledge dr. Ludvík Smrčka and dr. Natalya Goncharuk for the excellent theoretical consultations, Dr. Vít Novák for his supervision in transport experiments, Vlastimil Jurka, Karel Hruška and dr. Zdeněk Výborný for all the technological work and fruitful discussions. A special thanks is reserved for dr. Marek Potemski and dr. Vittorio Pellegrini with his colleagues for the organizing of my stays at LNCMI in Grenoble and at NEST in Pisa. Last but not least, I mention my simple thanks to exceptional people around me for the motivation to work and to think.

I appreciate as well the support from the Charles University, especially the GAUK No. 425111, my supervisor's grant GACR No. P204/10/1020 and other financial support from Institute of Physics, Academy of Science of Czech Republic.

I declare that I carried out this master thesis independently, and only with the cited sources, literature and other professional sources.

I understand that my work relates to the rights and obligations under the Act No. 121/2000 Coll., the Copyright Act, as amended, in particular the fact that the Charles University in Prague has the right to conclude a license agreement on the use of this work as a school work pursuant to Section 60 paragraph 1 of the Copyright Act.

In Prague, August 5, 2011 Lukáš Nádvorník

Název práce: Elektronická struktura materiálů na bázi grafenu

Autor: Lukáš Nádvorník

Katedra: Fyzikální ústav Univerzity Karlovy

Vedoucí diplomové práce: RNDr. Milan Orlita, Ph.D.

Konzultant diplomové práce: dr. Karel Výborný

Abstrakt: V posledních dvou letech byl předeslán koncept umělého grafenu, vytvořeného v běžných polovodičových 2D systémech s využitím nanolitografie na jejich površích. Takový systém by měl umožnit studium jevů spojených s částicemi Diracovského typu ve zcela neuhlíkatých materiálech. Koncept předpokládá vytvoření dodatečného potenciálu v kvantové jámě využitím nanolitografického opracování povrchu nebo lokálních elektrod. Takto generovaná modulace transformuje běžnou parabolickou disperzi na oddělené minipásy, v nichž lze pozorovat Diracovy kužely. V teoretické části zavádíme čtyři kritéria, která představují odhady parametrů technologické přípravy a příhodné experimentální podmínky. V experimentální části studujeme cyklotronovou rezonanci v heterostrukturách AlGaAs/GaAs s hexagonálním potenciálem tvořeným vyleptanými dírami. Pozorovaná vícemódová cyklotronová rezonance je diskutována s ohledem na předpokládanou přítomnost Diracových kuželů.

Klíčová slova: umělý grafen, Diracovy kužely, povrchová supermřížka

Title: Electronic structure of graphene-based materials

Author: Lukáš Nádvorník

Department: Institute of Physics of Charles University

Supervisor: RNDr. Milan Orlita, Ph.D.

Advisor: dr. Karel Výborný

Abstract: In last two years, the proposal to create artificial graphene in standard semiconducting 2D systems via surface patterning has emerged. This way, an alternative system would be created, allowing us to study phenomena related to Dirac-type particles in a fully carbon free system. The main idea of the concept assumes the creation of an additional potential in a quantum well by nanopatterning of the specimen surface or by using local electrodes. The additionally introduced modulation can transform the conventional (i.e. parabolic) energy dispersion into separated minibands with possible appearance of Dirac cones. In the theoretical part, we introduce four basic criteria that estimate appropriate technological parameters and the required experimental conditions. Experimentally, we study the cyclotron resonance of prepared heterostructures AlGaAs/GaAs with induced hexagonal potential via the etching lateral holes. The observed multi-mode resonance response is discussed with respect to the expected appearance of Dirac cones.

Keywords: artificial graphene, Dirac cones, lateral superlattice

Contents

Introduction

It happens sometimes that a certain usualness inspires the world. A simple dailiness with a rough surface and pallid gray coloured. Such an event is a kind of true exceptionality that can be intensively felt if thinking about it. It might become more powerful than very sophisticated technologies. The specialty of such a case may rise from two characteristics: simplicity and implicitness (secret). The simplicity means that It is not too far from human, not armoured behind nanotechnologies, behind unimaginable dimensions or extreme rarity (as are processors, nanolitografically prepared devices or Qbits). In contrary, Its simplicity consists in easy availability and everyday performance – for example, when you write with a crayon or paste a tape on a piece of graphite. Its implicitness rests in disregard or neglect rather than in fundamental invisibility. The experience of suddenly uncovered extraordinariness, present inside, succeeds to previous (ordinary) experience in the same (aspect). In this case, it is nothing mystical (as sometimes the advanced technologies are), it becomes only a great novelty in already well known and accepted. In my opinion, the availability and wonders in known (aspect), lead to the easily accessible deepness. And for me, such kind of easily accessible deepness is a little dangerous... and very, very tempting indeed.

It is, most likely, the background of my high motivation in the topic of artificial graphene. Natural graphene, monoatomic carbon layer of graphite, has really inspired the world community of scientists, it has affected many fields of fundamental physics, as well as the technology and the industry [1, 2]. Nowadays, graphene is a base of some types of chemical detectors, analogical processors, it serves as conducting layer in LCD monitors and in the electronic paper concept [3]. It simply uncovered (pseudo-)relativistic effects in condensed matters. Naturally, our feeling of exceptionality may be catalyzed if one realizes that in graphene, massless particles are created thanks to two main features: its two-dimensionality and the hexagonal symmetry of its lattice.

This fact was not left unnoticed. The wish for creation artificially generated massless fermions, just by mimicking the nature, was too strong and the topic too attractive. And thus, after several papers concerned with theoretical electronic bandstructures of system with a rectangular and hexagonal potential [4, 5, 6, 7, 8], the idea of artificial graphene has emerged [9, 10, 11]. Following the inner thesis, the concept of artificial graphene consists in a simulation of both graphene characteristics – our two dimensional electron gases formed in quantum well inside heterojunctions (for example AlGaAs/GaAs) could mimic the two dimensional crystal of graphene; and the symmetry of honeycomb lattice can be imitated by an additional potential. There is not only one way how to create the potential, however in every case, it requires nanotechnological processing.

The reason behind the concept is not only focused to fabricate the same as the nature. Artificial graphene, if successively prepared, can serve as very variable system to proof-of-principle experiments since the manipulation with natural graphene is not very easy. Hence, it can simulate the effect of superlattices on graphene, its strain or controlled inhomogeneities, designed defects of its lattice and so on. The potential for applications consists also in advantages of the system itself. Unlike the natural graphene, the artificial one allows to change

all parameters as we want – for example the "lattice constant" or the value of the attractive potential of each artificial "atom". These changes could provide considerably modified characteristics of the material – which is not possible (at least, not in so easy way) in natural graphene. In summary, there is plenty of reasons for the study and fabrication of such a material.

As already anticipated, this master thesis focuses on artificial graphene concept, as one of graphene-based materials. The thesis is divided in four chapters, conclusion and two appendices. The first chapter introduces the reader into the world of graphene physics, descibes the particular features of graphene and shows experiments that directly indicate Dirac-like properties of the system. This knowledge is very important for the probing of our fabricated devices. The second chapter follows the author's theoretical calculations concerning the miniband structure of artificial graphene, the examination of dimensions of Dirac cones and it formulates four crucial criteria that one has to meet to observe graphene-like physics in a conventional material. The third chapter describes in details technological processing that the author made or assisted in, and beside the known method, it reveals another unique approach to create the potential. The last chapter concerns the experiments made on artificial graphene samples, nominally, far infrared spectroscopy and photoluminiscence in magnetic field and transport Quantum Hall effect experiments. Appendices contribute by an evolution of eigen function over first Brillouin zone and a special method how to extract the concentration of carriers from shapes of relative transmission spectra. Generally, the thesis covers more then 29 months of author's work in three European Institutions (Institute of Physics of Academy of Science of Czech Republic, Laboratoire Nationale des Champs Magnetiques Intenses, CNRS, in Grenoble, France, and Laboratorio NEST, Instituto Nanoscienze CNR in Pisa, Italy) and results presented here were sent for a publication (preprint is attached in appendix C).

1. Natural graphene – final aim

Ahead of opening the theoretical part of this Master thesis, a brief introduction into current physics of graphene is given. We describe the fundamental characteristics of graphene at a basic level and introduce necessary terminology, such as Dirac cone, massless Dirac fermion or Fermi velocity. We also mention some early experiments performed on graphene, namely magneto-transport and infrared magneto-spectroscopy, in which graphene provides its characteristic fingerprint. For further details about theory, preparation and well-known experiments, we refer to author's Bachelor thesis [12].

Unique properties of natural graphene originate from its two-dimensional crystal lattice with hexagonally arranged carbon atoms [1, 2]. From the viewpoint of crystallography, graphene's structure is not a Bravais lattice, but can be viewed as a triangular lattice filled by a base of two carbon atoms. The corresponding Brillouin zone is a hexagon, see figure 1.1, with several point of a higher symmetry: Γ (center of hexagon), M (middle of sides) and K and K' (hexagon edges).

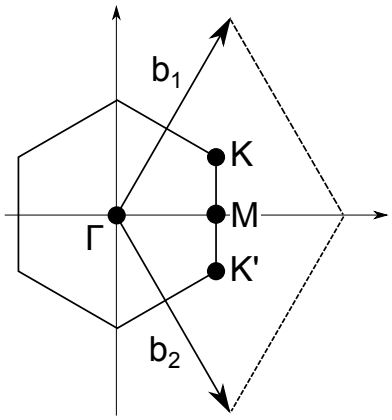

Figure 1.1: First Brillouin zone of natural graphene, with $\vec{b}_i$ base vectors of its reciprocal space. Relevant points marked.

One graphene layer, as a theoretical construction, was first considered by P. Wallace [13] in the 1947 and served as a reasonable starting point for calculations of band structure of bulk graphite. Graphene itself, as a purely 2D material, was assumed to be thermodynamically unstable those times. Following his tight-binding approach, we can limit ourselves to the hopping between nearest neighbours characterized by coupling constant γ_0. The band structure then takes as simple form:

$$E'(\vec{k}) = \pm\gamma_0 \cdot \left(1 + 4\cos^2\frac{\sqrt{3}k_y a}{2} + 4\cos\frac{\sqrt{3}k_y a}{2}\cos\frac{3k_x a}{2}\right)^{1/2}, \qquad (1.1)$$

which has been visualized in figure 1.2. a denoted the distance between two nearest carbon atoms.

Expanding equation 1.1 around the K points by $\vec{k}$, we obtain the following electronic dispersion:

$$E'(\vec{K} + \vec{k}) \approx \pm\frac{3\gamma_0 a}{2}|\vec{K} - \vec{k}| + \mathcal{O}((\vec{k}/\vec{K})^2) \qquad (1.2)$$

which is linear in $\vec{k}$, forming so-called Dirac cone. Recalling the standard expression for energy of relativistic particles, $E^2 = c^2p^2 + m^2c^4$, we immediately see that electrons in the vicinity of K points behave as massless particles, usually referred to as Dirac fermions [14]. Their velocity v_F, i.e. an effective velocity of light, is roughly 300× lower than real speed of light in vacuum:

$$v_F = \frac{3\gamma_0 a}{2\hbar} \approx 10^6 \frac{\mathrm{m}}{\mathrm{s}}. \tag{1.3}$$

To some extent, the Dirac fermion resembles neutrino, nevertheless, it has a well defined electric charge in addition.

Contrary to other two-dimensional systems, which are characterized by a parabolic dispersion law and consequently also by a constant density of states, $\rho = m/\pi\hbar^2$ (spin degeneracy included), graphene has a density of states that is linear in energy and vanishes at so-called Dirac point:

$$\rho(E) = \frac{2A_c|E - E_0|}{2\pi\hbar^2 v_F^2} = \frac{3\sqrt{3}a^2}{2\pi\hbar^2 v_F^2}|\varepsilon|. \tag{1.4}$$

From here the name "zero-gap semiconductor" originates – there is, actually, no real band gap but neither any continuous junction of the conduction and valence band. In undoped graphene, the Fermi level lies exactly at the Dirac point. The gating allows unusual and straightforward tuning between electron- and hole-like conductivity.

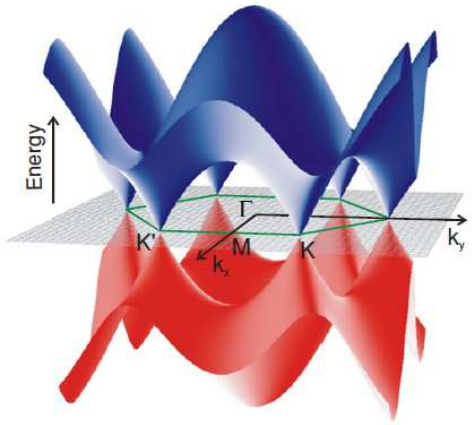

Figure 1.2: Visualization of the conduction and valence band in graphene. Dirac cones appear at K and K' point (Dirac point) in the primitive cell of its reciprocal space. Taken from [2].

If magnetic field is applied, graphene provides us with an unusual spectrum of Landau levels. In contrast to systems of massive particles, where Landau levels are equidistant and linear in magnetic field B, $E_n = (n + 1/2)\hbar eB/m^*$, Landau levels in graphene read:

$$E(n) = E_n = \mathrm{sgn}(n)\hbar\omega_c\sqrt{|n|} = \mathrm{sgn}(n)v_F\sqrt{2\hbar eB|n|} = \mathrm{sgn}(n)E_1\sqrt{|n|}, \tag{1.5}$$

i.e., they are not equidistant and scale as $\sqrt{B}$.

This relatively complex Landau level spectrum represents a nice playground for magneto-optical spectroscopy [15, 2]. Dipole-active transition are those with

$|n| \rightarrow |n| \pm 1$. Therefore, for instance, the transition $L_{-2} \rightarrow L_1$ or $L_{-3} \rightarrow L_4$ are allowed in graphene (see figure 1.3). An example of such transitions observed experimentally by far infrared magneto-spectroscopy is shown in figure 1.4.

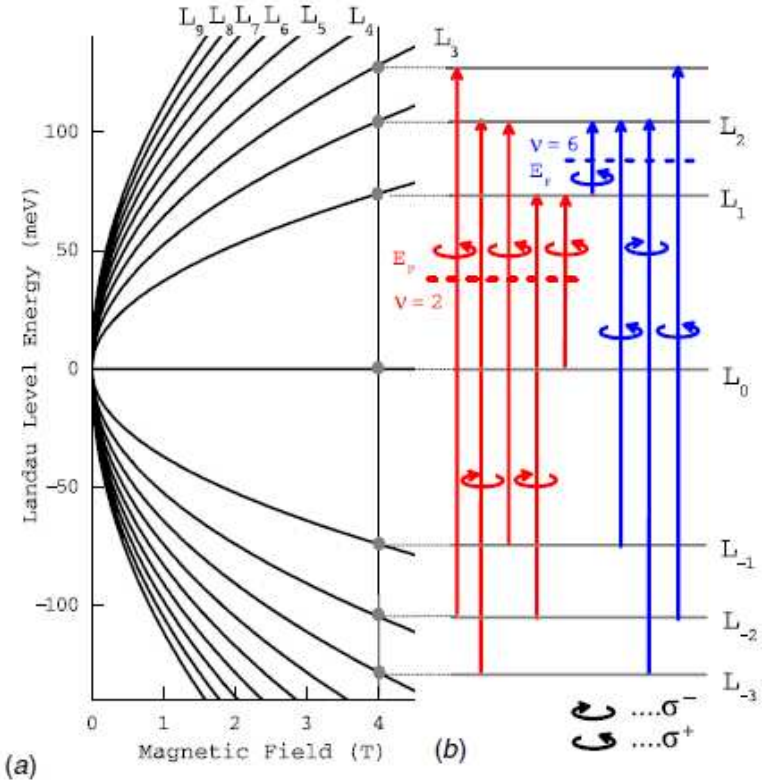

Figure 1.3: Evolution of Landau levels in graphene along magnetic field for several level index (left part). Allowed optical transitions are marked in the right part. Taken from [2]

Graphene, as well as conventional semiconductor heterostructures containing 2DEG layer, allows for observation of quantum Hall effect – fundamental magneto-transport phenomena. The quantum Hall effect is manifested by a step-like dependence of Hall resistance ρ_{xy}, contrary to classical Hall effect that implies a linear dependence of the Hall voltage on the applied magnetic field, $U_H = BI/ne$, where n is the carrier density and I stands for the current. Importantly, the steps in quantized Hall resistance have universal form, i.e. depend only n fundamental constants (e and $\hbar$):

$$\rho_{xy} = \frac{1}{i}\frac{h}{e^2} \quad \text{or} \quad \sigma_{xy} = i\frac{e^2}{h}. \tag{1.6}$$

i here indicates the number of (ballistic) edge channels in the quantum Hall regime. Since each occupied Landau level contributes one ballistic channel, the integer index i can be replaced by the integer filling factor $\nu = \frac{nh}{eB}$ (in case of the integer quantum Hall effect).

In graphene, the quantum Hall effect was also observed [14, 18]. but the lowest Landau level ($n = 0$) in this system does not depend on energy and importantly, it is shared by both electrons and holes. Therefore, the index i is now changed to $i = 4(j + 1/2)$ where j is new counting index. The prefactor 4 originates from the spin degeneracy and valley degeneracy (two Dirac points K and K'). The Hall

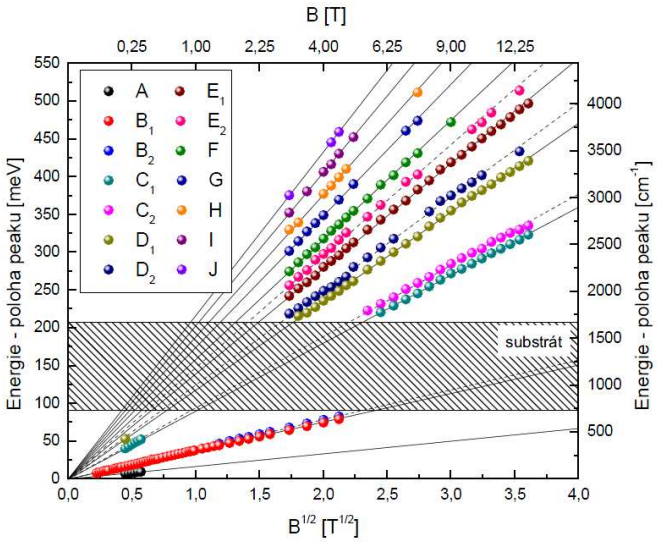

Figure 1.4: Performance of Far infrared measurements in magnetic field in graphene, taken from author's bachelor thesis [12]. Peak position, marked by points, lie precisely on $\sqrt{B}$-dependence curve.

plateaux have the same spacing but they are shifted by $\frac{2e^2}{h}$ from the origin. The half-integer quantum Hall effect, as it is usually referred to, is shown in figure 1.5 along with an analogous measurement on bilayer graphene, which exhibits another type of quantum Hall quantization.

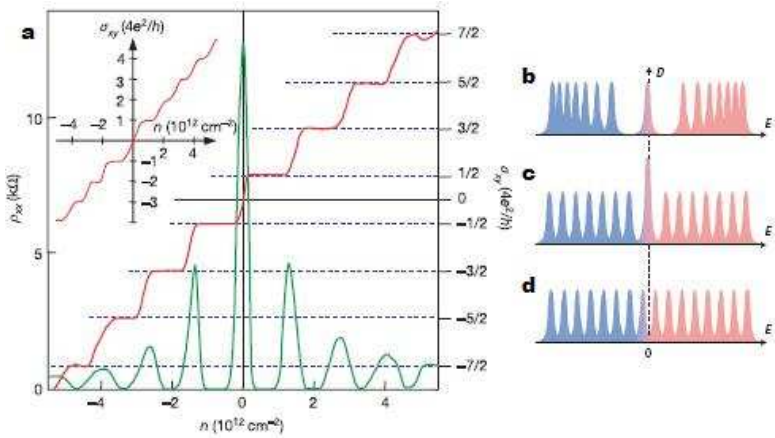

Figure 1.5: (a) Chiral Quantum Hall in graphene (central part). In inset graph displays conventional behaviour for graphene bilayer. (b) A scheme of Landau level structure in graphene monolayer, (c) in graphene bilayer and (d) in conventional material. Taken from [14, 18].

Both presented experiment are, in fact, direct proofs of Dirac (relativistic-like) nature of particles in graphene. Thereby, they will be the goal of our work – and they will strictly decide about our success in the creation of massless Dirac fermions in otherwise conventional material.

2. Theoretical estimates

Unlike natural graphene where all conceivable quantities are set at "correct" values by the nature, preparation of the artificial graphene requires an extra thought on the parameter adjusting and will be accompanied by certain nontrivial technological troubles. Intuitively, the main examples are the carrier concentration in samples or the effective amplitude of applied hexagonal perturbation. In terms of this perspective, we firstly proposed a simple numerical model which would demonstrate the technological accessibility and help us with initial steps to the sample fabrication. In the following section, a cosine model is presented and it is compared with the known properties of natural graphene, followed by the main aim of the theoretical part – formulation of four essential criteria which one has to meet to observe graphene-like behaviour in such a system.

2.1 Generation of miniband spectra

The general way how to calculate energy spectrum in a crystal, i.e. a dependence of energy of one particle state on quasi-wavevector $\vec{k}$, consists in finding a set of the lowest eigenvalues of crystal Hamiltonian in a convenient approximation. In our case, the Hamiltonian comprises the general kinetic and specific potential component

$$\hat{H} = \frac{\hat{p}^2}{2m^*} + \hat{V}(\vec{r}), \tag{2.1}$$

where m^* is the effective mass of electron in desired material (for GaAs we consider $m^* = 0.067m_0$, m_0 is the free electron mass). To construct the specific potential, one has to consider the natural graphene crystal symmetry. In figure 2.1 a typical graphene lattice and its reciprocal space are shown. The hexagonal "honeycomb-like" structure is formed by two shifted sub-lattices A and B, both of them generated by diamond-shape elementary cells defined by base vectors

$$\vec{a}_1 = \left(\frac{\sqrt{3}}{2}a, \frac{a}{2}\right), \ \vec{a}_2 = \left(\frac{\sqrt{3}}{2}a, -\frac{a}{2}\right), \tag{2.2}$$

where $a = a_{AA} = a_{BB} = \sqrt{3}a_{AB}$ is the lattice constant (that is the distance of nearest atoms of one sublattice). Such a crystal reflects in its reciprocal space the same symmetry. The Wigner-Seitz cell is now defined by any two of these three base vectors:

$$\vec{g}_1 = \frac{2\pi}{a}\left(\frac{1}{\sqrt{3}}, 1\right), \ \vec{g}_2 = \frac{2\pi}{a}\left(\frac{1}{\sqrt{3}}, -1\right), \ \vec{g}_3 = \vec{g}_1 + \vec{g}_2 = \frac{2\pi}{a}\left(\frac{2}{\sqrt{3}}, 0\right). \tag{2.3}$$

With regard to the following, four specific points of high symmetry should be mentioned:

$$\Gamma = (0,0), \ K = \frac{2\pi}{a}\left(\frac{1}{\sqrt{3}}, \frac{1}{3}\right), \ K' = \frac{2\pi}{a}\left(\frac{1}{\sqrt{3}}, -\frac{1}{3}\right), M = \frac{2\pi}{a}\left(\frac{1}{\sqrt{3}}, 0\right). \tag{2.4}$$

Two equivalent K- and K'-points are playing the crucial role in all the artificial graphene concept since the pseudo-relativistic behaviour rests in the these regions

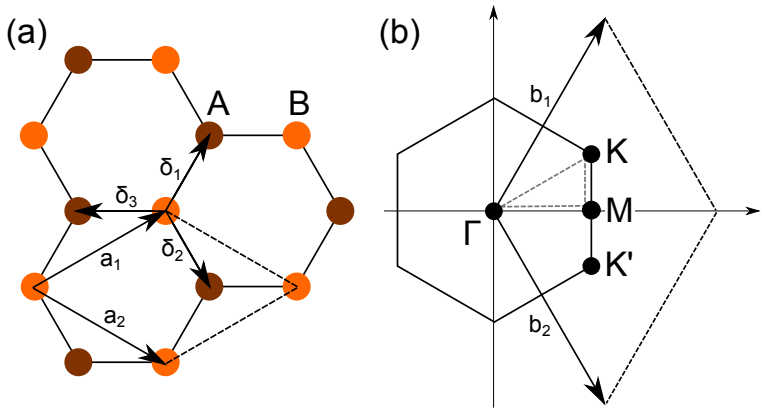

Figure 2.1: Scheme of graphene crystal lattice (a) and its first Brillouin zone in reciprocal space (b). The direct lattice is composed of two sublattices of atoms A and B, the elementary cell (delimited by vectors $\vec{a_1}$ and $\vec{a_2}$ and by dashed lines) contains one atom of each types. Analogously, the Wigner-Seitz cell contains in reciprocal space two dual "images" of these atoms K and K'. A typical path used in miniband diagrams is marked by gray dashed triangle.

of the Brillouin zone where the energy dispersion is linear [1, 2]. This will be more deeply studied in the next section. Now, it is intuitive to define the effective potential in real space (with $\vec{r}$ position vector) as a sum of cosine functions, using base vectors of the reciprocal space as anticipated by equations (2.3), thus

$$V(\vec{r} = \{x, y\}) = V_0(\cos \vec{g}_1\vec{r} + \cos \vec{g}_2\vec{r} + \cos \vec{g}_3\vec{r}). \tag{2.5}$$

Equation (2.5) is the easiest potential form approximatively describing the crystal of natural graphene, a numerical visualization is shown in Fig. 2.2.

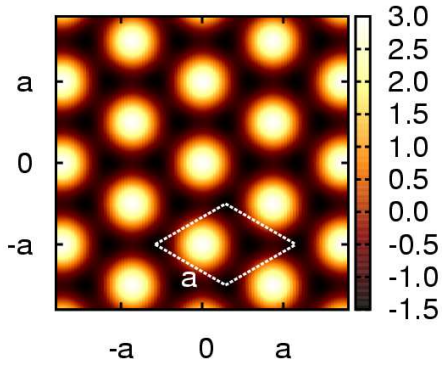

Figure 2.2: Visualization of studied hexagonal potential as of equation (2.5). Dark regions correspond to "atom positions" in real graphene, the elementary cell is indicated.

The form of chosen potential leads us to build the basis as a finite, but large enough, set of plane waves. Hence, for each point in Brillouin zone (each $\vec{k}$) the set is introduced as

$$\mathcal{B}_k = \left\{ |n_1 n_2\rangle = e^{i(\vec{k}+\vec{K}_{n_1 n_2})\vec{r}},\ \vec{K}_{n_1 n_2} = n_1\vec{g}_1 + n_2\vec{g}_2 \right\} \tag{2.6}$$

and the effective potential $V(\vec{r})$ is easy to rewrite

$$V(\vec{r}) = \sum_{\vec{K}_{n_1 n_2}} \tilde{V} e^{i\vec{K}_{n_1 n_2}\vec{r}} = \frac{V_0}{2}\left\{e^{i\vec{g}_j\vec{r}} + e^{-i\vec{g}_j\vec{r}}\right\}, \; j = 1, 2, 3. \tag{2.7}$$

Elements of the Hamiltonian in basis (2.6) are expressed as $H_{IJ} = \langle I|\,\hat{V}(\vec{r})\,|J\rangle$, where $I = \{n_1' n_2'\}$ and $J = \{n_1 n_2\}$ are multi-indices running through each $\vec{K}_{n_1 n_2}$. For the purpose of numerical solving, we transcribe the multi-index to one single index as follows: we start at Γ-point and continue to other centers of hexagons around the first Brillouin zone in clockwise direction (see the Fig. 2.3). This way, we browse all $\vec{K}_{n_1 n_2}$ up to desired distance from Γ. The counting index is then the the position of each point in this sequence. After the evaluation of H_{IJ} using

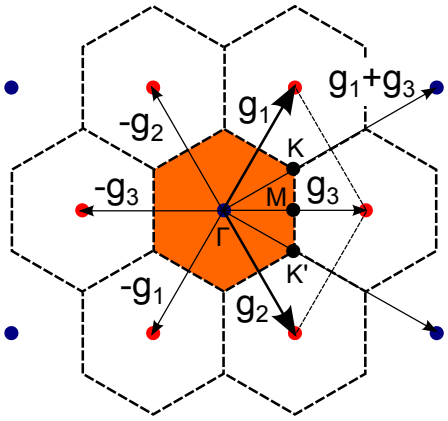

Figure 2.3: Scheme for reconstruction of the plain wave basis $\mathcal{B}_k$ when $\vec{K}_{n_1 n_2}$ is passing by all Γ-points (centers of hexagons), starting at the nearest-one.

orthogonality of bra-kets $\langle I|$ and $|J\rangle$, the final form of the matrix is

$$H_{IJ} = \langle n_1' n_2'|\hat{H}|n_1 n_2\rangle = \frac{\hbar^2(\vec{k} + \vec{K}_{n_1 n_2})^2}{2m^*}\delta_{n_1' n_2', n_1 n_2} +$$

$$+\frac{V_0}{2}\left(\delta_{n_1' n_2', (n_1 \pm 1) n_2} + \delta_{n_1' n_2', n_1 (n_2 \pm 1)} + \delta_{n_1' n_2', (n_1 \pm 1)(n_2 \pm 1)}\right), \tag{2.8}$$

where $\delta_{n_1' n_2', n_1 n_2} = \delta_{n_1', n_1}\delta_{n_2', n_2}$ are Kronecker δ.

Regarding the matrix form described by preceding formula (2.8), it is obvious that the ratio of diagonal to off-diagonal components is determined by three parameters: lattice constant a, amplitude of applied potential V_0 and effective mass m^* (which is constant in our case since we are fixed to GaAs). Since the shape of miniband spectra, as a dependence of allowed energy states on quasi momentum $\vec{k}$, will be obtained by calculating eigenvalues of the Hamiltonian, it is convenient to understand the role of the mentioned ratio. In the extreme case when the matrix is diagonal (thus the potential is equal to zero), the kinetic component prevails and the energy dispersion is perfectly parabolic, as with an ideal free particle problem or an ideal two dimensional electron gas (2DEG). Otherwise, if the kinetic component is zero or negligible against V_0, the off-diagonal potential elements dominate and the final dispersion is almost independent of $\vec{k}$ and the miniband spectrum is thereby practically flat. Appealing to intuition, the only

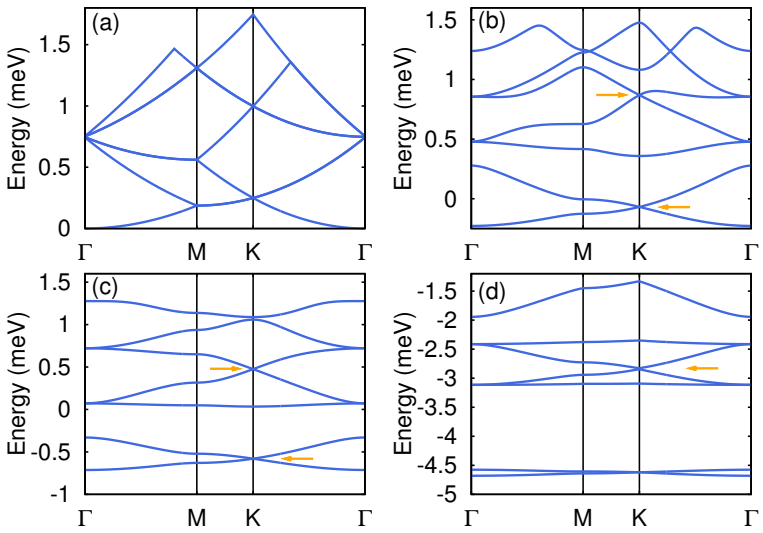

Figure 2.4: Minibands generated for several values of the parameter ζ. (a): $\zeta = 0$, dispersion of a free 2DEG. (b): $\zeta = 0.4$, first Dirac cones develops (indicated by arrow), the second one appears but remains covered by other bands. (c): $\zeta = 1$, both Dirac cones fully develop. (d): $\zeta = 4.0$, tight-binding type narrow minibands form and Dirac cones gradually flatten, ultimately becoming again unobservable. For $a = 200$nm, a,b,c, and d correspond to $V_0 = 0$, 0.4, 1.1 and 4.5meV in GaAs. The figure is taken from [19].

quantity governing the spectrum shape is the ratio of the kinetic (proportional $\sim a^{-2}$) to the potential ($\sim V_0$) energy, whereas the energy scaling of all miniband spectra is closely associated with absolute values of matrix elements. In this sense, we define the following dimension-less parameter

$$\zeta = \frac{m^*}{\hbar^2} V_0 a^2. \tag{2.9}$$

It is useful to note that up to a factor of unity, it is $\zeta \sim V_0/E_0$, where E_0 is the kinetic energy of a free electron in the K-point of the Brillouin zone.

Well converged miniband spectra were obtained by a numerical diagonalization of $\hat{H}$ in basis restricted to 36 plane waves as defined by (2.6). Changing ζ-parameter we encounter all possible situations, as shown in figure 2.4. Starting from the extremal nearly-free model ($0 < \zeta < 0.05$), when the potential is so low that the dispersion is visibly indistinguishable from the ideal 2DEG, we get to the transitional band-structures ($0.05 < \zeta < 10$), where the degeneracy is lifted and a significant splitting of minibands, especially at Brillouin zone boundaries is observed. Finally, we reach the tight-binding-like model ($\zeta > 10$) with almost completely flat minibands as typical for isolated atoms. The most important interval seems $0.5 < \zeta < 4.0$ where two visible crossing of linear part of dispersion – suggesting the occurrence of Dirac cones, uncovered by other minibands were created within lowest six minibands in K-point (and in K'-point analogously). This interesting region is the objective of the next section, but before the examination of these signs, the model itself should be verified.

Two simple methods are directly suggested to confirm the property of the model that has to offer results similar as in natural graphene. As it has been

said above, in the unperturbed or very slightly perturbed system, the dispersion is almost parabolic. The term $(\vec{k} + \vec{K}_{n_1 n_2})$ is then easy to evaluate in the special points of Brillouin zone and to compare them with the spectrum at $\zeta = 0$. To complete the idea, regarding to this term, the minibands in the Γ point should be six-times degenerated in lowest seven minibands because the kinetic term $(\vec{k} + \vec{K}_{n_1 n_2})^2$, respectively $|\vec{K}_{n_1 n_2}|$, take same values for six different pairs $n_1 n_2$ ($n_1 = \pm 1$ or 0, $n_2 = \pm 1$ or 0, except the combination $n_1 n_2 = 0, 0$). The minibands are twice degenerated for M-point ($\vec{K}_{00} = 0$ and $\vec{K}_{-1-1} = -\vec{g}_3$ with $\vec{k} = \vec{M}$) and three times for K-point ($\vec{K}_{00} = 0$, $\vec{K}_{0-1} = -\vec{g}_3$ and $\vec{K}_{-10} = -\vec{g}_1$ with $\vec{k} = \vec{K}$), referring to the figure 2.3 (we cover three lowest minibands only). With the same logic, the lowest energy for $\vec{k}$ laying on the line $|MK|$ has to be twice degenerated, as well as above the line $|K\Gamma|$. Continuing this train of thoughts, one can predict degeneracy and simple shape of all the dispersion spectrum and compare it with the numerically generated one. Such a verification has been made and no discrepancy was observed.

Not only the ideal 2DEG but also the perturbed modeling should be verified. For simplicity if we take into account only two lowest minibands, their splitting ΔE in M-point is determined by perturbation theory as

$$\begin{vmatrix} \Delta E & V_0/2 \\ V_0/2 & \Delta E \end{vmatrix} = 0, \tag{2.10}$$

where $\Delta E = E_0 - E$ is the energy shift from the unperturbed eigen-energy E, which gives $\Delta E = \pm V_0/2$, thus the size of created gap is V_0. As comparing with our numerical results two limitations of the estimate should be emphasized: first, V_0 has to be a weak perturbation against kinetic component E_0, so it is valid for low ζ only, and second, the interband coupling with other minibands is required to be minimal which leads to low ζ as well. Such a comparison of theoretical and numerical splitting is presented in figure 2.5. Regarding the dependences

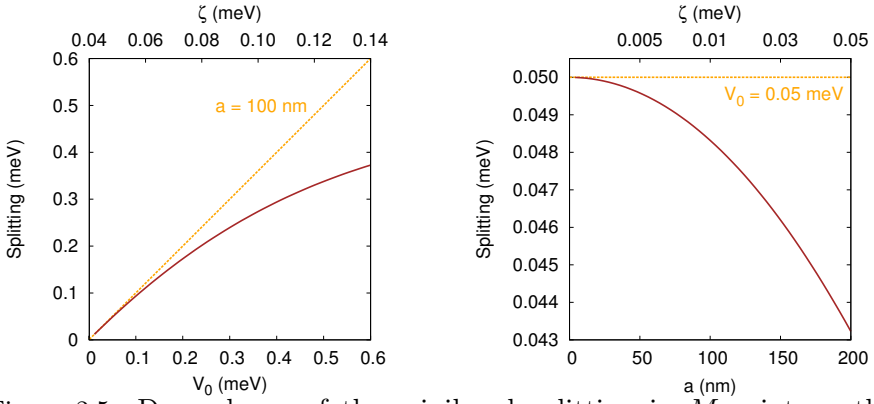

Figure 2.5: Dependence of the miniband splitting in M-point on the potential (leftside) and on the "superlattice constant" a (rightside), with a marked ideal curve (orange dashed). The numerical curve deviates from the ideal-one as ζ is increasing. Since ζ depends quadratically on a, the deviation is faster in this case. We emphasize that the y-axis scale is very tiny in the right figure.

of splitting correlation with V_0 and a in M point, a good approach to assumed behaviour is obvious when we go to lower ζ. To further investigate the model properties and checking them against natural graphene, we focus now on the main features in spectra - on probable Dirac cones.

2.2 Eigenfunctions as a proof

Along with obtaining miniband spectra in figure 2.4 that suggest the presence of two cones, two additional checks should be realized in numerical analysis – firstly to verify the relativistic nature of energy dispersion in this part of Brillouin zone (which are the linear dependence on $\vec{k}$ and isotropy close to K-point), and secondly to characterize the effective dimensions of the cones where the deviation is still acceptable. In this section, we show an exploration of eigenfunctions corresponding to the region of interest (K and K' points), and in the next section, the effective size of cones is investigated.

An example of miniband visualization over the interesting part of Brillouin zone directly suggests the cone-like character of studied features (see 2.6-left), contrary to the miniband crossing shown in figure 2.4(b) in the top right part which is forming not a cone but a "ditch" only (compare with figure 2.6-right). Moreover at first view, these cones-like structures have linear lateral surface and they are isotropic in $\vec{k}$-space (this aspect is quantitatively examined in section 2.3). Now, we will compare numerical eigen-functions generated close to K-points with the analytical ones. Following Ch.-H. Park and S. G. Louie [4], we sketch the derivation of analytical eigen-functions and use them as a starting point in our Dirac cone examination.

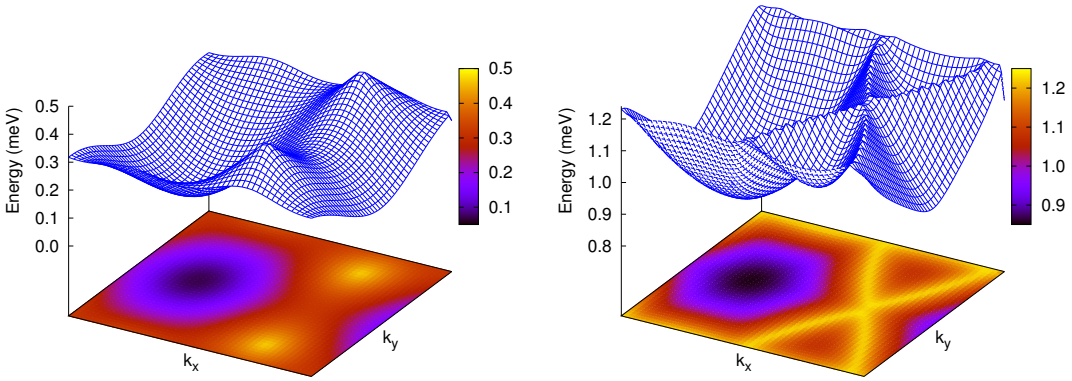

Figure 2.6: Surface plots of minibands. Left: The fourth miniband creating two obvious cone structure in K-points (yellow regions on the flat projection) and parabolic minimum in Γ-point (black region), configuration of parameters is identical as in figure 2.4(c), i.e. $\zeta = 1$, $a = 200$ nm. Right: the sixth miniband forming a ditch only, even if it looks like a possible cone crossing in figure 2.4(b) ($\zeta = 0.4$, $a = 200$ nm).

Let consider the basis of Hilbert space composed of three plane waves (the model takes into account only three dispersion bands) in form

$$\mathcal{B} = \left(e^{i(\vec{K}_1+\vec{k})\cdot\vec{r}}, e^{i(\vec{K}_2+\vec{k})\cdot\vec{r}}, e^{i(\vec{K}_3+\vec{k})\cdot\vec{r}} \right), \tag{2.11}$$

where $\vec{K}_n$ is a wave vector pointing to three K-points forming the angle 120°. Taking the Hamiltonian $\hat{H} = \hat{H}_0 + \hat{H}_1$, uncommonly we start with $\hat{H}_0$ as an unperturbed part formed by a matrix containing off-diagonal elements V_0 only,

and then $\hat{H}_1$ is the kinetic component viewed as a perturbation, represented by a diagonal matrix with a $\vec{k}$-vector originating in K-point. Eigen-values of $\hat{H}_0$ are $-V_0$, $-V_0$ and $2V_0$ which denote a twice degenerated miniband (Dirac cone) and one split off miniband. Since we are focused on Dirac cone present in two degenerated bands only, we find the following condition for V_0 and $\vec{k}$

$$\hbar v_0|\vec{k}| < V_0 < \frac{3\hbar^2 K^2}{2m^*}, \tag{2.12}$$

where the first inequality guarantees that we stay in linear part of dispersion not far from the K-point (hence $\hat{H}_1$ is still a weak perturbation) and the second is a request on very small coupling with the third miniband. In this situation, we neglect influence of the third split off miniband and reduce the matrix $\hat{H}_1$ to 2×2 in Hilbert space spanned by two eigen-vectors (belonging to the eigenvalue V_0) of $\hat{H}_0$ as follows

$$\hat{H}_1 = \hbar\frac{v_0}{2}\begin{pmatrix} -k_x & -k_y \\ -k_y & k_x \end{pmatrix}, \tag{2.13}$$

with $k_x = |\vec{k}|\cos(\theta_{\vec{k}})$, where $\theta_{\vec{k}}$ is the angle between $\vec{k}$ and the x axis. This can be rewritten as

$$\hat{H}_{eff} = \hbar\frac{v_0}{2}(k_x\sigma_x + k_y\sigma_y), \tag{2.14}$$

which is just the effective Hamiltonian of graphene for $\vec{k}$ close to K-point expressed using two Pauli matrices σ_x and σ_y. The group velocity of states described by (2.14), called Fermi velocity v_F, is given by

$$v_F = \frac{v_0}{2} = \frac{\hbar|\vec{K}|}{2m^*} = \frac{2\pi\hbar}{3m^* a} \tag{2.15}$$

and is a half of the group velocity of free 2DEG v_0. It is appropriate to note that v_F is dependent only on $1/a$ and $1/m^*$ and not on V_0. We focus more deeply on v_F in the next section.

Eigen-values of $\hat{H}_{eff}$ denoted in equation (2.14) are

$$E(s,\vec{k}) = s\hbar\frac{v_0}{2}|\vec{k}| \tag{2.16}$$

and its eigen-functions

$$\left|s,\theta_{\vec{k}}\right\rangle = \frac{1}{\sqrt{2}}\left|\uparrow\right\rangle + \frac{1}{\sqrt{2}}se^{i\theta_{\vec{k}}}\left|\downarrow\right\rangle, \tag{2.17}$$

where $s = \pm 1$ is a band index and states $|\uparrow\rangle$ and $|\downarrow\rangle$ are pseudospin eigen-states of σ_z. They correspond to situations when all electrons are strongly localized near atoms of sub-lattice A, or B, respectively,

$$|\uparrow\rangle = \frac{1}{\sqrt{3}}e^{i3\pi/4}\left(1, e^{i2\pi/3}, e^{i3\pi/4}\right)^T, \quad |\downarrow\rangle = \frac{1}{\sqrt{3}}e^{i3\pi/4}\left(1, e^{-i2\pi/3}, e^{-i3\pi/4}\right)^T, \tag{2.18}$$

expressed in the original basis (2.11). To visualize these eigen-states, we shown in figure 2.2(a-d) their symmetrical and antisymmetrical combinations, i.e., the state (2.17) with $\Theta_{\vec{k}} = 90°$ and $-90°$. Controlled by the $\vec{k}$-vector orientation

(it means to the $\theta_{\vec{k}}$), electrons are either localized in the middle of two neighbouring "atoms" of sublattice A and B, or in a channel over "atom" arm-chair. Immediately, we can compare the analytical solution, figure 2.2(c) with a numerical output of the model, which is plotted in figure 2.8(a), and we state that in sufficiently low distance from K-point and with V_0 not too large (the criteria started in the equation 2.12) very similar features are numerically generated (the figure is located in appendix B). By letting the $\vec{k}$-vector go around the K-point (with $|\vec{k} - \vec{K}| \ll |\Gamma K|$) and so passing through six main axes of crystal symmetry, all six symmetrical and antisymmetrical functions were reconstructed. Although the ideal conditions for this observation are quite strict – the radius and V_0 have to be small enough, the correlation of highly idealized and radically two-miniband-reduced analytical solutions with the numerical-one, taking into account the coupling with 36 other minibands and the spacial effect of non-zero $\vec{k}$, it is a very good demonstration of the occurrence of Dirac cones in this region, as it is in real graphene.

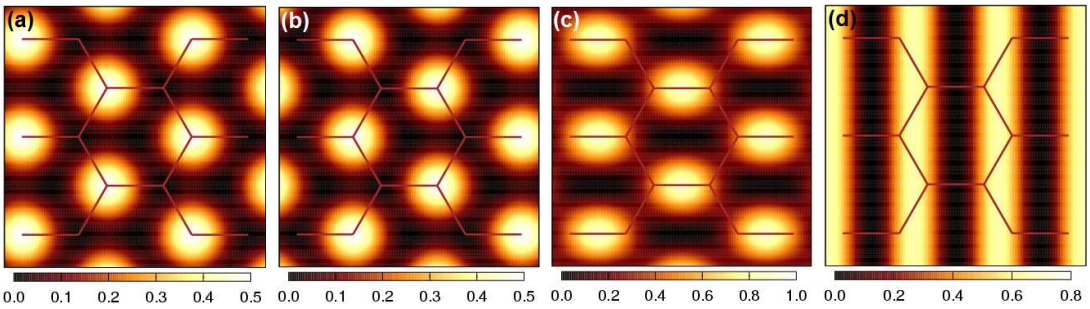

Figure 2.7: Modulus square of eigen-states in real space (a): $|\uparrow\rangle$, (b): $|\downarrow\rangle$, (c): and their symmetrical $\left|+, \theta_{\vec{k}} = 90°\right\rangle$ and (d): antisymmetrical $\left|+, \theta_{\vec{k}} = -90°\right\rangle$ combination as explained in the main text. It is necessary to emphasize that for other $\theta_{\vec{k}} = 210°$ and 330°, the eigen-states looks identically as in (c), only rotated by 60° or 120° – in other words, the it is occupying one of the remaining two pairs of hexagon sides. We note that the symmetrical combination is normalized to 1.

The dependence on rising V_0, i.e. ζ, or larger $\vec{k}$ will now be analyzed. Looking at figure 2.8(a-d), where such a dependence is shown, one finds the correlation with one expects from the spectra: as the V_0 is increasing, electrons are more and more localized in "atom" positions and the system is merging to tight-binding model of completely isolated "atoms". Otherwise if $\vec{k}$ is leaving the linear region of the effective cone and moves towards Γ-point, the extrema of eigen-functions are quickly decaying into a practically flat density of probability of localization and become almost a plane wave corresponding to the region of parabolic dispersion.

To complete the view, we should observe another low-laying minibands in K-point. Although corresponding analytical solution is not available, a simple prediction can be taken. Regarding to the third split miniband, in the range of very low ζ, its eigen-state should represent localization of electrons in the last high-symmetry point of the Brillouin zone (when pseudospin-states are occupying atoms of sublattice A and B) – the central region, i. e. the Γ-point. The eigen-function is expected to be symmetrical in $\vec{k}$-space because of the symmetry of third minibands close to K-point, see figure 2.9(a). This region is also a complement to the area of all possible eigen-state combinations of first and second

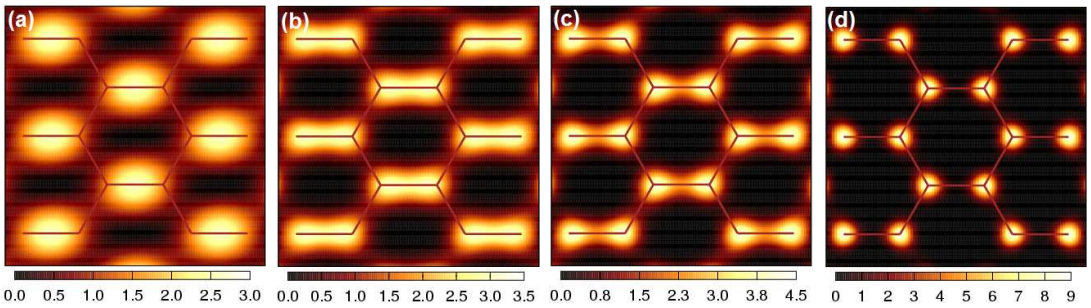

Figure 2.8: Square of eigen-vectors generated by the model for a small radius 1/1000 of the distance $|\Gamma K|$ and $\zeta = 0.01$, 0.4, 1.0 and 4.0, referring to (a-d) respectively. As ζ increases, the model is transforming from the nearly-free to tight-binding-one (compare with 2.4). We note that the colorbar scale is changing.

miniband. In this range of ζ, the description by three minibands, as presented above, is valid and the sum of all eigen-states should uniformly cover all the reciprocal space (which corresponds well with the nearly-free point of view). If we increase ζ and shift the model to the tight-binding-like situation, the function is now completing the others to a different form, see figure 2.9(b), when the central part is depopulated contrary to "atoms" and their joint-segments. Concerning the second Dirac cone, a typical shape of second harmonic is expected and due to its nature – the symmetrical combination of two pseudo-spin states, the final square of the wavefunction has three maxima in place of the only one corresponding to the first Dirac cone. Visualizations of mentioned eigen-states are shown in figure 2.9(c,d).

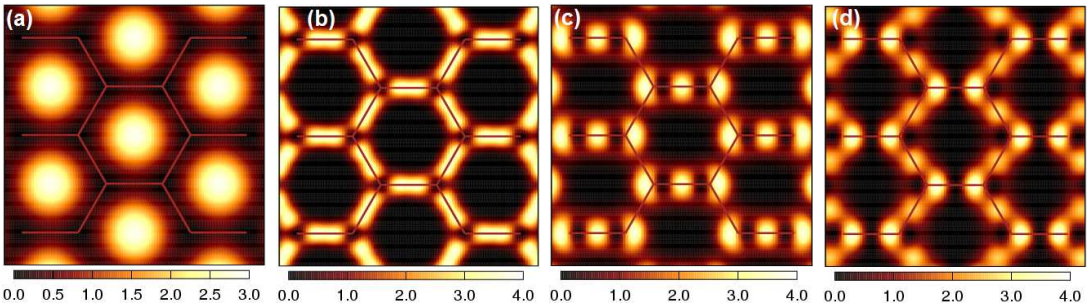

Figure 2.9: Square of eigen-functions in radius 1/100 of the distance $|\Gamma K|$ corresponding to the third (a,b) and fourth miniband (c,d). (a): the function taken with $\zeta = 0.4$ is a complement to the other possible configuration of eigen-states in first and second band (compare with 2.8(b)), thus it is now covering all the reciprocal space. (b): the same situation for $\zeta = 4$, where the sum of eigen-functions of all three bands creates a different tight-binding structure (see figure 2.8(c)). (c) and (d): Symmetrical and antisymmetrical combinations of pseudospin eigen-states corresponding to the second cone (compare with the first cone 2.2(c,d)). The colorbar scale is changing.

2.3 Effective dimension of Dirac cones

The ability to define the effective range of linearity in the dispersion spectrum could seem to be crucial since, in principle, adjust the Fermi level to cross the Dirac cone, i.e., the dispersion in its approximatively linear part. At the beginning, let's notice that the simplicity of model, which is not reflecting the real profile of the potential and preparation of samples in general, and the experimental difficulty to adjust the Fermi level with a great precision make a precise examination of Dirac cones complicated. Nevertheless such an estimate, even made using a simple model, should be useful to the understanding the dependence of the deviation from the linear-part and of size of cones on two main parameters – the ζ and the radius from K-point. Firstly, an analysis based on overlaps between two eigen-functions will be presented, followed by a group-velocity-based point of view, and finally the isotropy of cones will be shortly discussed.

The standard definition of overlap between two wave functions introduced as a scalar product in Hilbert space is not a suitable form in our case since it gives zero for two plane waves

$$\int \psi_1^* \psi_2 d^2r = \int e^{-i(\vec{k}'+\vec{K}_{n',m'})\vec{r}} e^{i(\vec{k}+\vec{K}_{n,m})\vec{r}} d^2r = 0 \tag{2.19}$$

if $\vec{k}' \neq \vec{k}$ or $\vec{K}_{n',m'} \neq \vec{K}_{n,m}$ (the integration is taken over all space). Hence we use a new quantity to investigate the wave-functions. This modified overlap is defined in the simplest way as

$$\left\langle e^{i(\vec{k}'+\vec{K}_{n',m'})\vec{r}} | e^{i(\vec{k}+\vec{K}_{n,m})\vec{r}} \right\rangle = \delta_{n'n}\delta_{m'm}. \tag{2.20}$$

In the new definition (2.20) we reduce the integration area and integrate only over one elementary cell. This way, the overlap (2.19) starts to differ from zero since the in the new range we do not integrate over the complete period of harmonic function in the integrand. Next, we neglect the dependence of the overlap on $\vec{k}' - \vec{k}$ since we focus mainly on the limit $|\vec{k}' - \vec{k}|a \ll 1$.

Now regarding the form of eigen-states around K-point in the equation (2.17), we deduce that the term $\langle +1, \theta_{\vec{k}1}| + 1, \theta_{\vec{k}2}\rangle$ is equal to 1 for $\theta_{\vec{k}1} - \theta_{\vec{k}2} = \Delta\theta_{\vec{k}} = 0$ and equals 0 for $\Delta\theta_{\vec{k}} = \pi$. The non-extremal overlap is intuitively governed by a harmonic cosine function due to the complex exponential in the equation (2.17). Since wave-functions are, in general, calculated up to (undetermined) overall complex prefactor, the meaningful quantity is the absolute value. Explicit calculation using (2.17) yields $|\cos(\Delta\theta_{\vec{k}}/2)|$.

Numerical results, obtained by the modified scalar product of eigen vectors in the basis of plane waves, are shown in figure 2.11 (against ζ) and 2.10 (against radius r, distance of $\vec{k}$ from the K-point). It can be seen that as the Dirac cone is more imperfect (when ζ is decreasing or the radius r is increasing), overlaps are more deviating from $|\cos(\Delta\theta_{\vec{k}}/2)|$. It seems to be difficult to define a sharp boundary of the cone because the way, how much this type of deviation influences the electron behaviour, cannot be easily predicted, however, we can find the radius r when the linear dispersion starts to deform fast to other type of dispersion. With respect to our further experimental results, we can set the limits for $\zeta = 0.4$ and 1.0 within the first and second cone as $r_{1^{st}} \approx 1/3$ and $r_{2^{nd}} \approx 1/5$ of distance

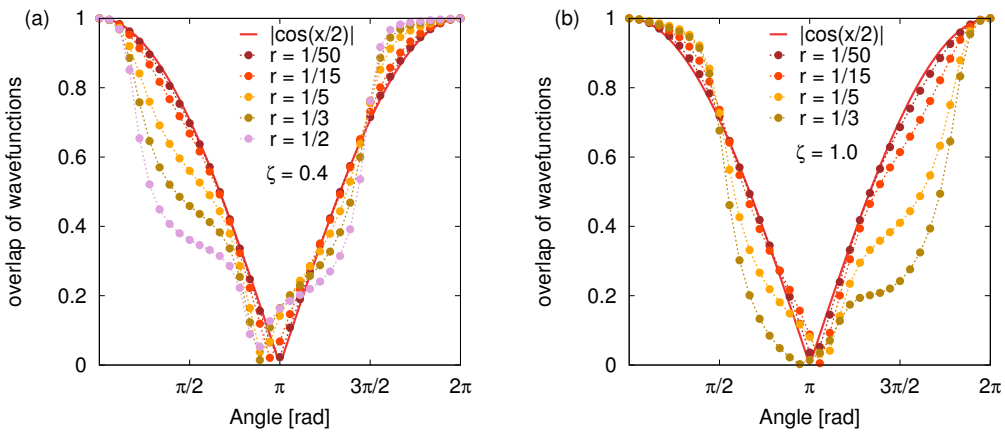

Figure 2.10: Overlaps of wave-functions (a) taken from the first cone at $\zeta = 0.4$ and (b) from the second-one at $\zeta = 1.0$ as depending on the radius from K-point. The indicated ratio corresponds to the part of $|\Gamma K|$ distance.

$|K\Gamma|$, respectively. Regarding the dependence on ζ, see figure 2.11, the first cone is fully developed at $\zeta \approx 0.4$ and the second-one at $\zeta \approx 2.0$ whereas overlaps do not change to much when ζ is over this value.

The evolution of the Fermi velocity on r – the main characteristic of the linear dispersion, is a good candidate for a limiting factor of Dirac cone size. In general, the linear part of dispersion has the group velocity $v_F = \frac{1}{\hbar}\frac{d\varepsilon(\vec{k})}{dk}$ equal to a constant. Hence, we can indicate the maximal radius of the cone according to a point where v_F starts to considerably differ from the constant.

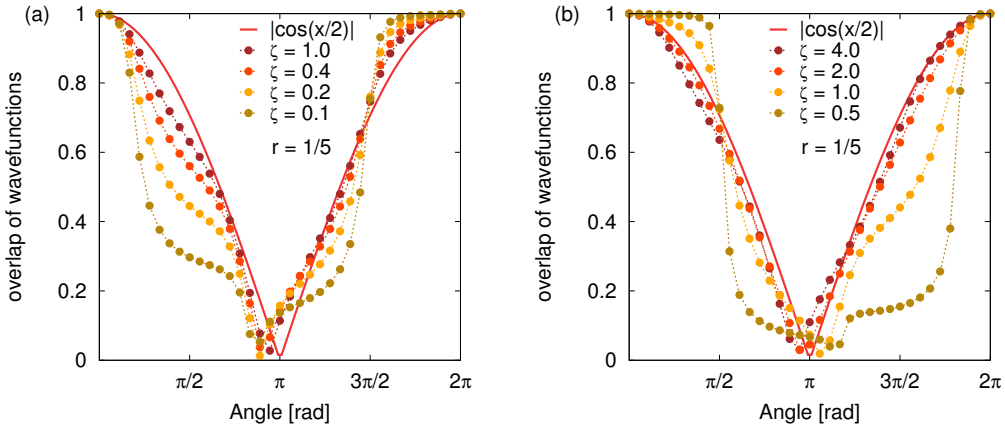

Figure 2.11: Overlaps of wave-functions generated around (a) first and (b) second Dirac cone at $r = 1/5$ of $|\Gamma K|$. It seems plausible to say that cones are fully developed at $\zeta = 0.4$ and 2.0, respectively, since the perfection of the behaviour decelerates quickly.

As one can see in figure 2.12, the final Fermi velocities $v_F = 2.4 \times 10^4$ and 4.8×10^4 m/s in K-point is exact for all ζ, as expected by (2.15) for the first and second cone with $a = 150$ nm, nevertheless the profile of v_F is not flat around this point. In low ζ after the cone is developed enough, a large constant plateau is created but v_F is then decreasing (ev. increasing) in the proximity of Dirac cone. It means that the cone has majority of its surface linear but the vertex is

slightly deformed into a paraboloid. Increasing ζ, we suppress this behaviour and obtain a perfectly flat dependence, implying a nearly perfect cone. Upon further increase of ζ, the plateau is falling down and the dispersion has to slow down its group velocity to reach the correct value of v_F in K-point. One can argue that this parabolic deviation is small as compared to the dispersion near Γ-point, for example, and the global shape is conical as well. An overall conclusion is that the first cone does not finish its growth completely at $\zeta = 0.4$, as suggested by overlaps, and the ideal ζ value for both of cones is $0.7 < \zeta < 1$. The maximal radius is estimated as $r_{1^{st}} \approx 1/3$ and $r_{2^{nd}} \approx 1/5$ of the distance $|\Gamma K|$. Finally, we have to note that in very large ζ, the v_F in K-point is not remaining the same but it is slightly decreasing despite the prediction (2.15) which is not dependent on $V_0 \sim \zeta$. The reason is that the derivation of mentioned equation is done by the first order perturbation theory assuming the basis of three plane waves (2.11). Nevertheless, our numerical calculations are made in the basis of 36 waves, thus the effect is caused by mixing of higher bands. Analytically, this shift of v_F can be described by the second or higher order of the perturbation theory, as made in [9].

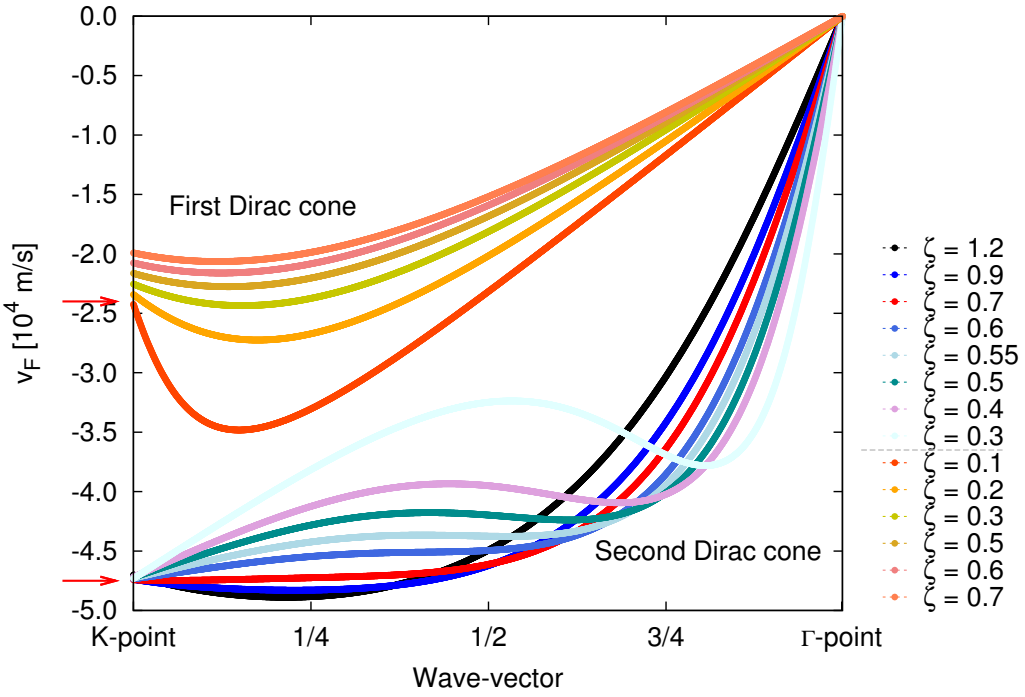

Figure 2.12: Fermi velocities v_F against the position between Γ and K-point for the first and second Dirac cone (first and fourth miniband, respectively), $a = 150$ nm. Red arrows indicate the theoretical ideal v_F in K-point: -2.4×10^4 and -4.8×10^4 m/s, the gray dashed line separates the legend for each cone. The optimally flat dependence is shown by red curve for the second cone. Slight v_F shift is notable in higher ζ for the first Dirac cone. Obviously, the best values for the cone shapes are $0.7 < \zeta < 1$.

At the end of this section, after observing the homogeneity of v_F, the cone isotropy should be also commented. The ideal Dirac cone has circles as its isoenergetic contours (points in reciprocal space with the same energy), however, even

in natural graphene a massive deformation, called trigonal warping, is observed when getting farther from the K-point (see [13]). It is caused by the intuitive fact that at large distances the situation is not the same in different directions – there are three carbon atoms which deform the band to a triangular-shaped one. The same phenomenon will appear in our model whereof intensity is suitable for the determination of the cone size as well. We used the lower part of both cones and visualized them in the horizontal projection, so now, the key parameters are the maximal radius r and ζ. Looking at figure 2.13, one can clearly observe the reducing of the trigonal warping as ζ increases or the radius decreases.

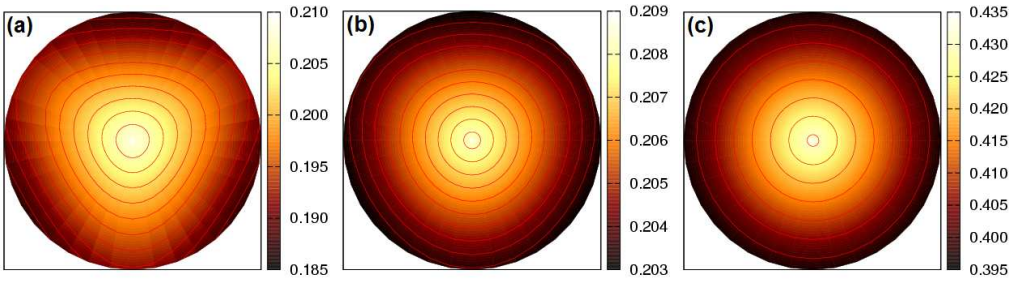

Figure 2.13: Examples of top views on the center of Dirac cones. (a): the first cone with $\zeta = 0.1$ and $r_{max} = 1/15$ of $|\Gamma K|$, (b): the first cone with $\zeta = 0.1$ and $r_{max} = 1/50$, and (c): the second cone at $\zeta = 1$ and $r_{max} = 1/15$. The trigonal warping is reducing at lower r and hifger ζ.

To determine the size, isoenergetic contours have been fitted by circles, as suggested, and the sum of residues of the fit was plot against parameters ζ and r. Nevertheless, as reported in figure 2.14, no special point (for example a local massive gradient) in the dependence on radius r was observed and the tendency is linear thus the maximum acceptable value of parameter r cannot be determined naturally by the curve profile. The only way how to find it is to select a threshold of the sum of residues. Otherwise, the dependence on ζ is more significant – decreasing of the trigonal warping with increasing ζ is stopped around $\zeta = 0.8$ and increases again. This behaviour is corresponding with the evolution of v_F in 2.12 for too large ζ and support the ideal choice of $0.7 < \zeta < 1$.

2.4 Four criteria – experimental basis

We have already identified two Dirac cones in spectra, investigated their properties and compared the electron behaviour with natural graphene. It is now appropriate to conclude all these theoretical efforts and to find a convenient link to the experimental part of the thesis. We condense the knowledge into four crucial criteria that have to be met for the accessing Dirac fermions in semiconductor superlattices. A fulfillment of these criteria is not, naturally, a guarantee that a practical observation will succeed but offers to us a good guideline in technological and experimental point of view.

1. *Favourable miniband structure* – recalling figure 2.4 and comments related to it, the first obvious criterion has already been noticed. It is the appropriate adjusting of ζ parameter to obtain a miniband structure containing a large, well developed Dirac cone(s) which is not "covered" by other branches of

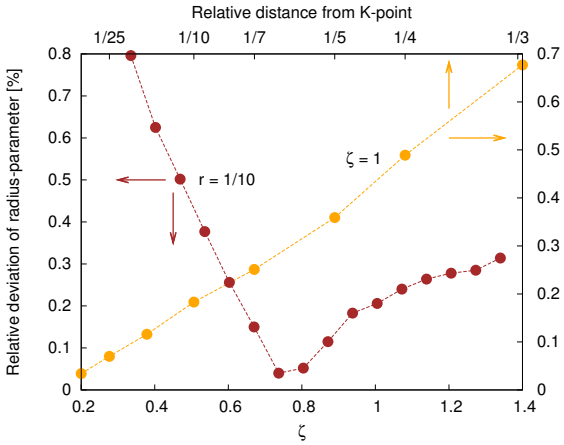

Figure 2.14: A fitting of isoenergetic contour by a circle with the radius as a fitting parameter. The standard deviation (in %) is plotted againts ζ and the diameter r. While the dependence on r is linear and does not offer any natural boundary of the cone, as the ζ parameter is changing the evolution is non-linear and occurs a minima near $\zeta = 0.8$. This fact is in accordance with conclusions concerning v_F (the figure 2.12).

the miniband dispersion. Disregarding the fine details discussed in section 2.3, the linear part is accessible in mentioned range $0.5 < \zeta < 4.0$ for the second Dirac cone and $0.2 < \zeta < 2.0$ for the first one, that corresponds to $0.6 < V_0 < 4.5$ meV and $0.2 < V_0 < 2.3$ meV for the "superlattice" constant $a = 200$ nm, respectively. The way how to relate V_0 with the actual technology is one of main subjects of the next chapter. The parameter $\zeta \approx 0.8$ was suggested as an ideal choice whereas both cones are well developed and have the best inner profile (see the preceding section).

2. *Fermi level positioning* – graphene-like properties are, in particular, caused by its Fermi level positioned just in the linear part of the energetic dispersion. This happens when the carrier concentration n, or the Fermi level E_F, in a sample is adjusted to cross one of the exposed Dirac cones. For $\zeta = 1.0$ and the first and second cone, see figure 2.4(c), it means to set $n \approx 0.5 \times 10^{10}$ and 3.3×10^{10} cm^{-2}, but for $\zeta = 4.0$ the second cone requires more favourable $n \approx 6.5 \times 10^{10}$ cm^{-2} (see the Appendix A to more details). If one reduces the "superlattice" constant a with ζ remaining the same, the system offers identical miniband shape (including Dirac cones) – only shifted in energy (the spectrum is outspread), see the comment to the definition of ζ (2.9). For example the configuration $\zeta = 0.9$, $V_0 = 4$ meV and $a = 100$ nm implies $n \approx 1.7 \times 10^{10}$ and 1.4×10^{11} cm^{-2} for the first and second cone. From the technological point of view, the second cone provides more favourable perspectives because of more easily accessible n.

3. *Low disorder* – under realistic conditions, such an ideal electronic dispersion as calculated in section 2.1 is smeared by several mechanisms present in the system. Two main types are the irregularity of the induced potential (see next chapter 3) and the presence of impurities, scatters and other inhomogeneities in the 2DEG layer. While the effect of the first mentioned disorder is complicated to quantify, the second-one can be estimated by

the condition for its mean free path $l_e = \hbar\mu\sqrt{2\pi n/e^2} \gg a$. Since for $\mu = 10^5$ cm^2/(V·s) (our typical mobilities after all technological processing) and $n = 10^{11}$ cm^{-2} it is $l_e \approx 500$ nm, this criterion is not too strict. We note that it is a necessary but not sufficient condition only.

4. *Careful probing* – the last important criterion concerns the experimental conditions, especially T and B, which must not influence the system too much. In the following measurements, Landau level transitions are the key optical probing method. If one wants to observe graphene-like behaviour the modulating potential has to be the main governing effect and the cyclotron quantization plays the role of a scanning means only. It implies the condition $\hbar\omega_c \gg E_{DC}$, where $\omega_c = \frac{eB}{m^*}$ and E_{DC} is Dirac cone size in energy, thus the cone is too large to contain minimally two Landau levels (between them transitions are realized). Since $E_{DC} \sim 0.3$ meV (for $\zeta = 1$, $a = 200$ nm) and $\hbar\omega_c/B \sim 1.7$ meV/T, tolerable magnetic fields are hundreds of mT at most. Analogously, the ambient temperatures have to satisfy $kT \gg \hbar\omega_c$ that may mean the sub-kelvin range.

Concluding this chapter, we demonstrated that an ideal cosine perturbation deforms parabolic dispersion of 2DEG to the extent that it leads to the appearance of two well exposed Dirac cones. These cones have a non-trivial inner structure depending on the applied perturbative potential and they can retain their linear dispersion as far as 1/5 – 1/3 of the distance $|\Gamma K|$ from the K-point. Following four essential criteria, comprising a good choice of the potential, an appropriate concentration of carriers, a low disorder and low magnetic field and temperatures, one might be on a right way towards the first artificial graphene preparation ever made.

3. Technological preparation

The idea to create artificial graphene consists in mimicking nature. There are two basic characteristics of graphene: it is two-dimensional and has a hexagonal symmetry. The first of them is easy to imitate by the (quasi-)2D electron gas (2DEG) created at a heterojunction or in a quantum well. Such structures, for example aluminum gallium arsenide in contact with gallium arsenide (AlGaAs/GaAs), are nowadays straightforwardly available with a relatively high quality thanks to recent developments in molecular beam epitaxy (MBE) and well understood as well. The 2DEG is created as a very thin layer just on the junction, see figure 3.1(a). The electrons are donated by a doping layer separated by a spacer tens of nanometer wide. This modulation-doping technique allows to spatially separate electrons from their (ionized) donors and to suppress the scattering on them. In result, the mobility of electrons in 2DEG can easily exceed 10^6 cm^2/(V·s).

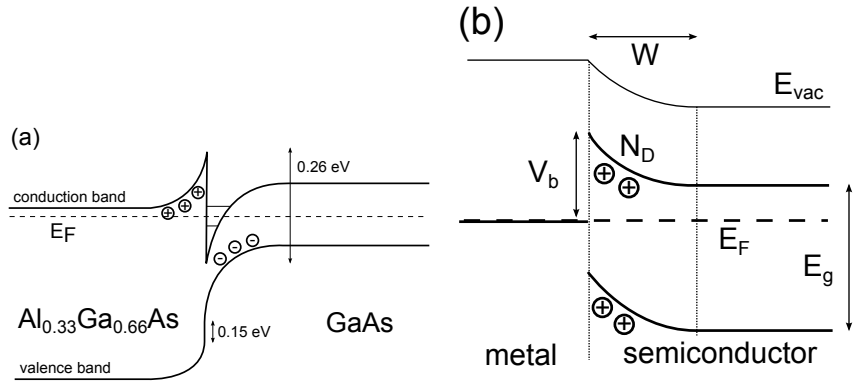

Figure 3.1: Band diagrams. (a): The bandstructure in equilibrium near the heterojunction contact, solid lines in the triangular well show bottoms of individual electronic sub-bands created by spatial confinement of electrons in 2DEG. (b): The semiconductor–metal contact, i.e. the Schottky barrier.

In the first section of this Chapter, we present three ways how to mimic the second aspect of graphene – the hexagonal lattice, induced by a lateral superlattice introduced in Chapter 2, and then steps in technology necessary to prepare our samples for both, optical and transport experiments. Especially, the electron beam lithography, the dry etching and metal sputtering will be mentioned as well as the ohmic contacting of 2DEG or designing the Hall bar geometry. In this sense, the chapter covers the second phase of the way towards artificial graphene which the author of this thesis and his collective had passed.

3.1 Methods of creation and control of potential

The performed simulations imply necessity to create lateral modulation of the strength of a few meV. The potential minima then play the role of artificial carbon atoms and thus electrons loose original parabolic dispersion, as presented in chapter 2. In principal, there are several methods to do that, and during our work, we have practically explored three of them.

The easiest way is to deform electron concentration locally by a metallic contact, i.e. to create a Schottky barrier on the surface of the heterostructure, see Figure 3.1(b), which locally depletes density of electrons. Such a barrier has a characteristic width of

$$w \approx \sqrt{\frac{2\varepsilon_S V_b}{eN_D}}, \tag{3.1}$$

where N_D stands for concentration of donors and other (negatively) ionized impurities. The dielectric constant in GaAs/GaAlAs structures reaches $\varepsilon_S \approx 13\varepsilon_0$ and the barrier height is typically $V_b \sim 0.5$ eV. This implies the width of the depleted region about $w \sim 250$ nm for $N_D \sim 2 \times 10^{16}$ cm^{-3}. In this way, the effect is strong enough to create lateral modulation of the 2DEG that is located 100 and 115 nanometers under the surface in our heterostructures (see figures 3.2a,b). In our samples, the 2DEG contains electrons provided by two heavily Si-doped δ-layers located between the surface and the heterojunction ($N_{\delta-Si} \sim 10^{12}$ cm^{-2}), which significantly screen the surface-induced modulation of 2DEG. Nevertheless, the real simplicity of production was the reason why the metal-semiconductor method was used in the technological beginning.

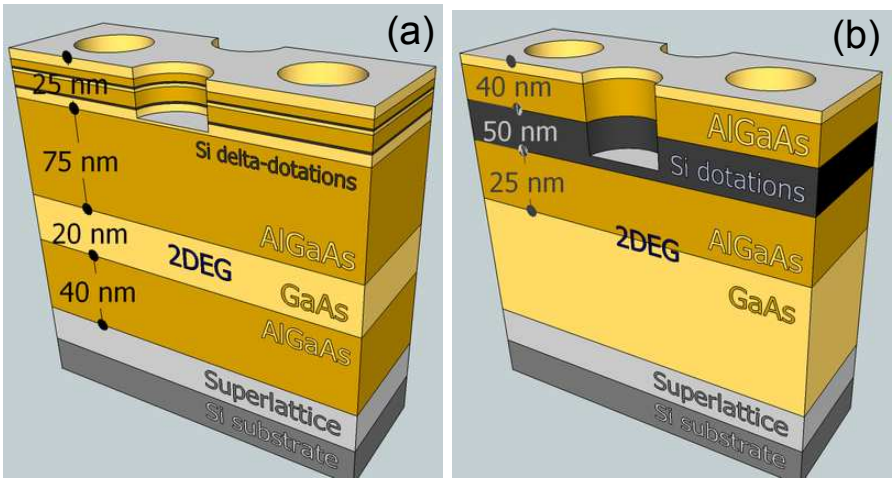

Figure 3.2: Schemes of wafer cross-sections. (a): wafer 1 where 2DEG is formed in 20 nm wide quantum well 100 nm under the surface, and (b) wafer 2 with a triangular well containing 2DEG in the depth of 115 nm.

The second possibility consists in the modulation of the specimen surface by etching, which locally changes distribution of electrons between surface states, Si-layers and 2DEG. In our non-etched structures, the surface states are saturated via first Si-doped δ-layer, whereas the second one fills the 2DEG. The local etching thought the first δ-layer has following three impacts on our structures, three effects appear in the system: (i) the removed doping layer is no more saturating the surface states, (ii) the density of states on the damaged surface is increased (iii) the reduced distance of 2DEG from surface induces its saturation directly from 2DEG. All three effects result in a local decrease of concentration in the 2DEG layer that can be formally represented by the effective potential V_0, introduced in Section 2.1. Such a process is expected when we use the lateral modulation of the surface by etched holes (antidots) in the required symmetry – the antidot represents a decrease of concentration that means the maximum of the repulsive potential. According to figure 2.2 on the page 9, the symmetry has

to be triangular (the lightest regions). The correlation between the depth of holes d and V_0 is not exactly known but we expect that its is monotonous in certain limits (as holes are deeper V_0 increases). In the next chapter, this correlation has been found experimentally and is concerned as one of main results of this work.

The most sophisticated method is extension of the first one and supposes a local gating of the sample. Unlike the hole etching that produces only one permanent V_0, the top gate allows us to tune V_0 in a certain range. Such an electrode composes of a metal planar gate with long metal needles attached on its bottom and reflecting the hexagonal or triangular potential (according to expected bias). Needles touch the surface and create a local electrostatic potential, while the plate on top of them keeps needles at the same potential (see figure 3.3). Besides the mentioned tunability, this design offers us another advantage – the electrode does not introduce any mechanical disorder as the etching and thereby the mobility remains unaffected. On the other hand, this design does not allow us to create lateral modulation with a period shorter than is the depth of 2DEG and the obtained potential profile has to be numerically calculated (Laplace problem with defined boundary condition), as shown later on. The use of samples with a very shallow 2DEG as well as a proper design of the gate shape is then crucial. Naturally, the top gate covering all the active area of the sample is usable for transport experiments. Presented structure should be further fitted with a back gate that will provide us with an independent tuning of the electron density. This way, the first two criteria introduced on the page 20 can be controlled directly during the experiment.

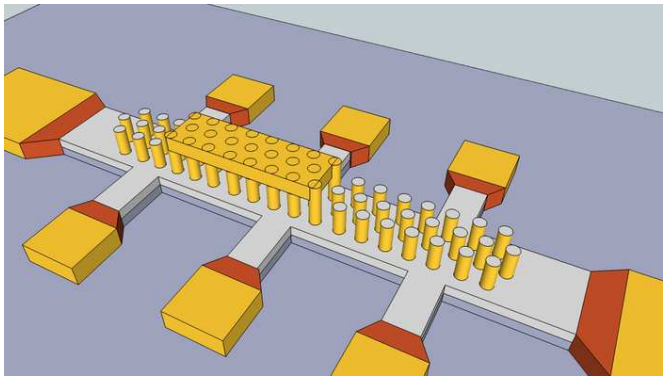

Figure 3.3: Since ζ depends quadratically on a, the deviation is faster in this case. We emphasize that the y-axis scale is very tiny in the right figure.

Three presented ways to create and control the potential of artificial graphene correspond to real steps done in technology. The first method, based on Schottky-type contact, was used in the beginning, nevertheless no reasonable results were observed in (transport) measurements. Probably, the effect of δ-Si doping layers was as strong as predicted and the Schottky barrier had influence only on very shallow part of the sample and the 2DEG remained not modulated. Therefore, this method has been left and the second proposal has been realized. As shown in several optical and transport experiments, this approach indeed leads to lateral modulation of 2DEG, see chapter 4. The third procedure is the most sophisticated and demanding. For the tunability and complex control of the system one has to pay a lot – new technology and processes require plenty of time and human

force. The fabrication of such gates is currently in progress and the state-of-art is presented in section 3.3. Hence, all the experimental results were obtained with samples processed by the second method. The following text provide details about preparation of the samples via this second approach.

3.2 Optical samples

In this section, we summarize the important technological steps necessary to prepare artificial graphene samples for infrared magneto-spectroscopy measurements. We refer to them as to "optical" samples. These steps involve the composition of used heterostructures, the electron beam lithography, as well as the dry etching and final "make-up" of our samples. In general, specimens for optical studies are easier to prepare since the only requirements are reasonable samples lateral dimensions (exceeding the wavelength of the probing light, i.e. hundreds of microns) and in case of a transmission configuration also substrate transparency (undoped substrate necessary).

For our purpose, we used $Al_{0.33}Ga_{0.66}As$/GaAs heterostructures MBE-grown on a GaAs substrate with the composition shown in figure 3.2(a,b). Two type of structures have been used: the first one has a quantum well 20 nm wide located located 100 nm under the surface. The electrons are provided by two δ-Si layers (14 nm and 24 nm under the surface). In the second wafer, the 2DEG is located nearby the heterojunction 115 nm deep below the surface and 50 nm wide Si-doped region is placed in the depth of 40 nm. Both structures are capped by a thin GaAs protecting layer.

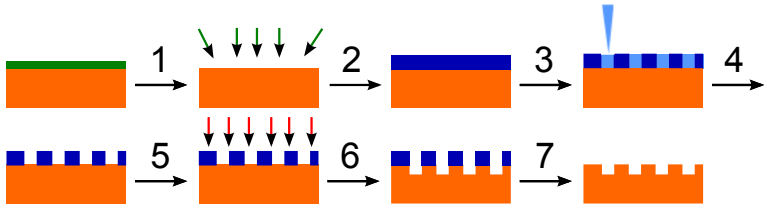

Figure 3.4: Process of electron beam lithography. Step 1: O_2 plasma etching of surface oxides, step 2: sample surface coated with resist, step 3: electron beam exposition changes chemical properties of exposed area, step 4: resist developing (washing out the exposed/unexposed area, according the type of resist), steps 5 and 6: dry Ar^+ + $SiCl_4$ plasma etching, resist mask is etched out very slowly, step 7: resist removal in the acetone solution.

To laterally modulate the 2DEG via the second discussed method, we used the electron beam lithography (EBL). The principle is analogous to the standard optical (UV) lithography – an electron sensitive resist is put on the sample and exposed to the electrons. Unlike the optical lithography, no mask (equiv. stamp) is used and lateral resolution is provided by a narrowly focused electron beam "writing" on the resist. This resist is coated on samples surface cleaned from oxides by oxygen plasma (fig. 3.4, step 1) – 100 Watts and 300 Pa for 2 minutes have been empirically found as fully sufficient. The resist exposed to electron beam modifies its internal structure by polymerization (depolymerization) for the positive (negative) resist and becomes dissolvable (hardened) compared to unexposed

resist. The sample is then placed into the developer solution that removes all the exposed and unexposed areas for the positive and negative resist, respectively. Such a procedure (see figure 3.4, steps 2–4) creates a resistive polymer mask on the surface and enables other planar technologies. Although the finest resolution of used EBL is about 8 nm (the beam radius is 2 nm), the resist thickness significantly reduces this resolution. The electron beam penetrating through the resist layer is successively laterally extended and electrons effectively expose larger and larger area. Simultaneously, the thickness of the resist cannot be arbitrarily low, since e.g. the dry etching partially removes the polymer. The the minimal thickness (100 nm in our case) is then directly related to the power and duration of this etching. With the least necessary resist thickness, the real resolution of EBL is approximatively 40 nm. This leads to an unpleasant limitation – the minimal diameter of holes is 50 nm and their distance 70 nm. In our present experiment, only samples with hole diameters 60–80 nm and $a = 200$ nm were used due to practical reasons, since the time required for the exposition of the 1 mm^2 area is proportional to the quantity of holes (tens of hours for one sample). A SEM image of such a developed resist mask is shown in figure 3.5(a).

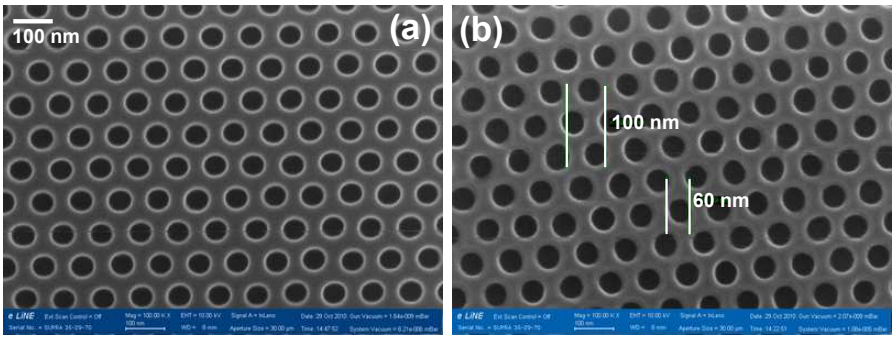

Figure 3.5: Scanning electron microscope microphotography of (a) the exposed and developed resist mask (we use a reference patterned area since the SEM procedures might re-expose the mask) and (b) the etched holes on the surface.

Holes were produced by dry plasma etching using the ICP apparatus from Oxford Instruments (steps 5 and 6 in figure 3.4). The process consists in the argon bombardment and the directional $SiCl_4$ chemical plasma etching. The sample with a removed oxide layer (the step 1 in figure 3.4 can be also done just before the etching) is placed into the chamber on a Silicon or stainless chuck and its surface is activated by long-run Ar^+ bombardment (in our case: 12 minutes, power 8 W, $\sim$ 80 V, pressure 2 mTorr, strike pressure 30 mTorr). Afterwards, the own etching is realized using the ratio Ar:$SiCl_4$ 10:2 with power 9 W, pressure 4 mTorr, strike at 30 mTorr and the ICP acceleration 10 W for the stainless chuck and the ratio 10:1 with power 6 W, pressure 2 mTorr, ICP 0 W for the silicon one. The important difference between the two kinds of chucks consists in oxidation. The silicon chuck is more susceptible for the oxide creation which has to be therefore removed by hydrofluoric acid before its next use. Moreover, the metal chuck is not so reactive and catalytic as the silicon one and the etching is thus advancing slower even at higher powers. And just relatively slow etching at high powers implies more stable conditions and more precise results. For both chucks, a correlation between etching duration and the depth of holes was found to

be linear, reaching 40–80 nm/min and 30–45 nm/min for the silicon and stainless chucks, respectively. An SEM image of such an etched surface is shown in figure 3.5(b).

Results of performed etching were verified by two techniques. Regarding the known thickness of the resist, the resulting depth of holes can be determined by the DEKTAK device without sacrificing the possibility to etch further if the present holes are not deep enough. Thanks to a 25 μm wide tip it can scan the surface and restore the surface profile with the z axis precision of a few nanometer. For this purpose, special specimens (called "satellites") are etched together with every sample. Each satellite contains several rectangularly-shaped holes with varying edge length. Such a profile of the surface, still partially covered by polymer mask, serves as a trustful indication of the real etched depth (see figure 3.6(b)). After the wanted depth is achieved, the resist on the sample is stripped off in acetone (figure 3.4, last step). If not, the sample is not stripped and etching continues and another satellite is used. As the real depth of narrow holes is easy to measure directly, we can, alternatively, cleave the satellite structure and observe the cross-section using the electron microscope. Such a particularly precise but demanding measurement is shown in figure 3.6(a) and was done for each prepared optical sample.

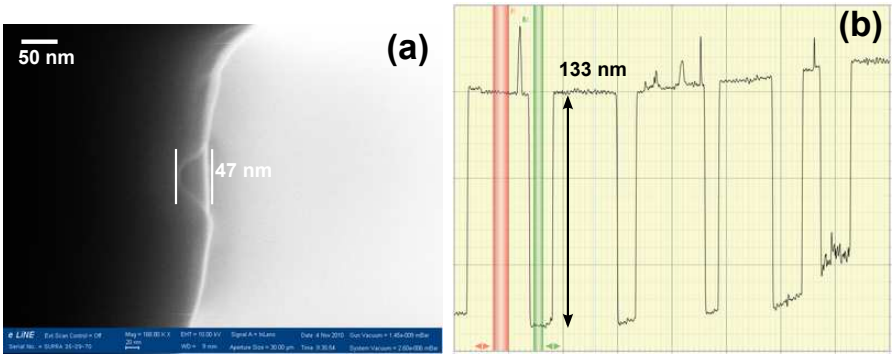

Figure 3.6: Direct and indirect method to determine the depth of etched holes. (a): A SEM image of a cross-section of a patterned sample. For this purpose, we used an additional control field of holes. (b): DEKTAK measurement of large reference holes (30 μm diameter).

The patterned area was surrounded by a gold window that defines optically active surface of the sample. This golden frame is made of 50 nm thick layer of pure gold and was created by the thermal vapour deposition over a developed mask. This time, an optical lithography was applied. After the deposition, the sample was placed into a beaker with acetone that lifted off gold layers sitting on the remaining resist, as schemed in figure 3.7, last step. The final structure is shown in figure 3.8. Logically, if the metal layer is thicker then the resist no lift off is enabled.

Specific parameters of prepared and studied samples are listed in table 3.1. Here, we do not mention samples finally not explored experimentally. The samples A and B based on the wafer 1 while the sample C on the wafer 2. The carrier concentration n and the mobility μ are derived from transport measurement using the method presented in the chapter devoted to experiments. The final depth of holes varies among the samples that allows us to estimate the correlation between

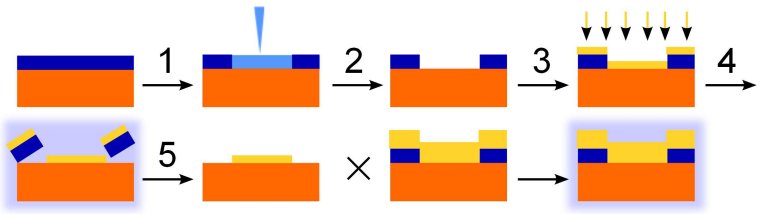

Figure 3.7: Process of the lift off. Step 1: exposition of the resist layer, step 2: developing, step 3: vapour deposition of metal (AuTi or AuGeNi in our case), steps 4 and 5: lift off in an acetone solution. The deposed layer has to be thinner than the thickness of the resist, otherwise the lift off is not possible or all the metal layer will be lift off.

the depth and the potential amplitude V_0. These important characteristics are also listed in the table 3.1.

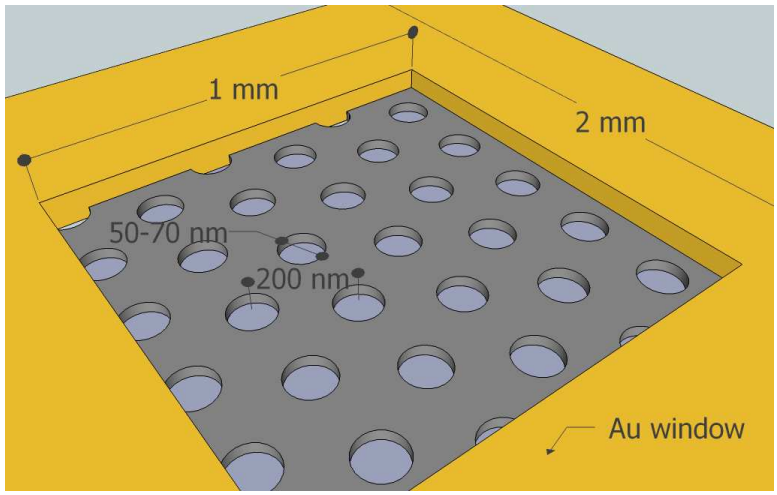

Figure 3.8: Schematic of an optical sample with golden window. Diameter of holes is not in scale.

Sample	n ($\times 10^{11}$ cm^{-2})	μ ($\times 10^6$ cm^2/(V·s)	$d_{\mathrm{dots}}/d_{\mathrm{2DEG}}$ (nm)
A	<1	>0.7	15/100
B	<1	>0.7	20/100
C	1.4	0.5	48/115

Table 3.1: Basic characteristics of samples in the discussion. The certain incertitude of n and μ for samples A and B originates from the difficult electric contacting of the wafer 1.

3.3 Transport samples

The transport measurement on samples prepared by the following method studies quantum transport phenomena – the Quantum Hall effect (QHE) and the Shubnikov de-Haas oscillations (SdHO). Usually, the Hall bar configuration is used, as shown in figure 3.9(a), which enables to measure the voltage drop along and across the current channel. The region outside the Hall bar is etched out so

deeply that 2DEG is completely removed in this area. Both current and voltage contacts were created using standard Au/Ge/Ni alloy and expended by a gold contacting plate. These bonding plates allow us to create contacts to the Hall bar via micro-bonding machine, see figure 3.9(b).

The preparation of Hall-bar structures includes several etching phases. During the first one, the Hall-bar structures is isolated (using a negative resist mask). The artificial graphene structure is created in the second phase, when the main channel is hexagonally patterned by etched holes analogously to optical samples.

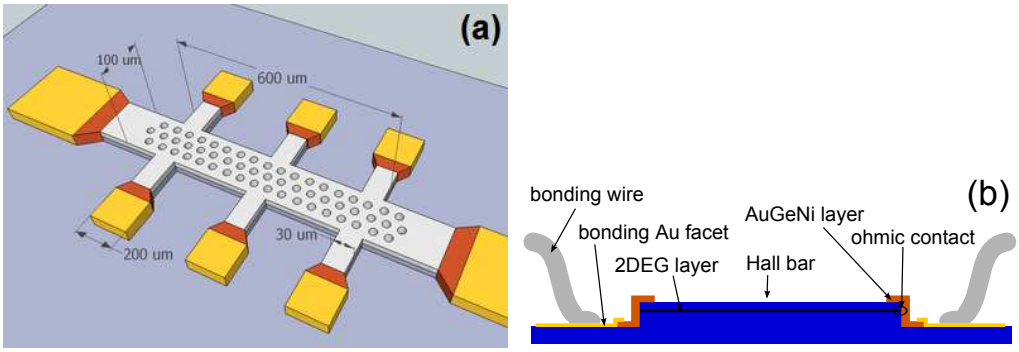

Figure 3.9: Schematics of Hall bar design. (a) Visualization of one of realized Hall bar configurations. Brown colour designates the ohmic contacts, the golden one bonding plates. (b) Hall bar cross-section. The AuGeNi alloy contacts 2DEG through Hall bar edges.

In detail, the ohmic contacts are deposited using $Au_{88\%}Ge_{12\%}$ target with a Ni slices. Due to a poor adhesion of gold on GaAs, a thin Ti layer ($\approx$ 10 nm) is deposited prior the main contact layer composed of 90 nm AuGeNi. After the lift off (that implies the resist thickness more than 100 nm), contacts are annealed in reducing atmosphere, namely in the forming gas H_2 + N_2, to prevent oxidation of contacts during the annealing (450°C for 5 minutes with the rampe 100°C/min). Thanks to it, the alloy AuGe does not only interfuse with nickel but also foms "dendrites" that contact better the 2DEG layer. Within this procedure, the visual morfology of contact is important – empirical rule says that before the annealing the surface should be golden grey and glossy and it should not tear when scratching (that means a good adhesion to the surface). The contacts become reddish brown, dull and rough after annealing (see figures 3.10(a,b)).

The deposition of golden bonding plates is straightforward procedure equivalent to the preparation of gold windows in the optical samples (we refer to the image of a final Hall bar structure in figure 3.11(a)). Gold is used because of its softness useful for the micro-bonding. First, the sample is glued onto a chip-carrier by an epoxy resin that is resistant against low temperatures and easily dissolvable in acetone. Second, after several hours of hardening, the chip-carrier is set into the bonding device equipped by a thin needle with 15 μm thick aluminum wire. Bonding contacts between the chip-carrier and the sample are interconnected semi-manually (motions of the hand are transferred into very tiny motions of the tip). For the wire mounting, ultrasound is used – the wire is squelched and impacted into the soft gold plate, see figure 3.11(b). Such a prepared chip-carrier is then manually soldered onto a holder by indium melt and silver wires.

Since this Master thesis is mainly focused on optical measurements, the transport was understood as a complementing experiment. A number of samples with

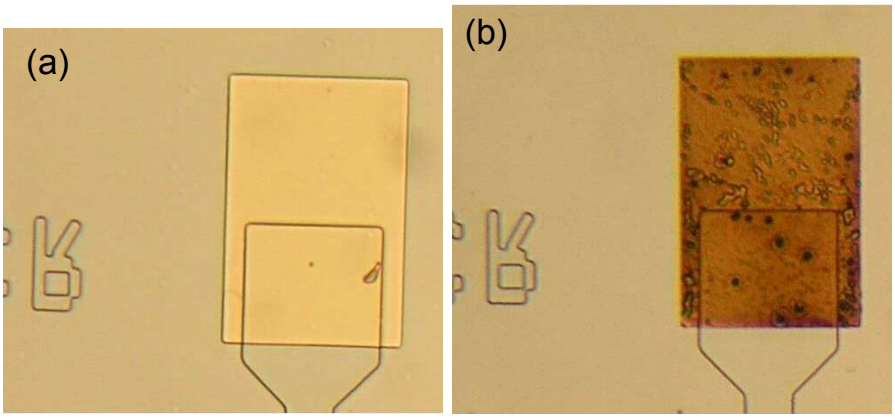

Figure 3.10: Comparison of AuGeNi layer (ohmic contacts) before and after the annealing process. The morphology and visual control are the first and fast verification that the 2DEG is well contacted.

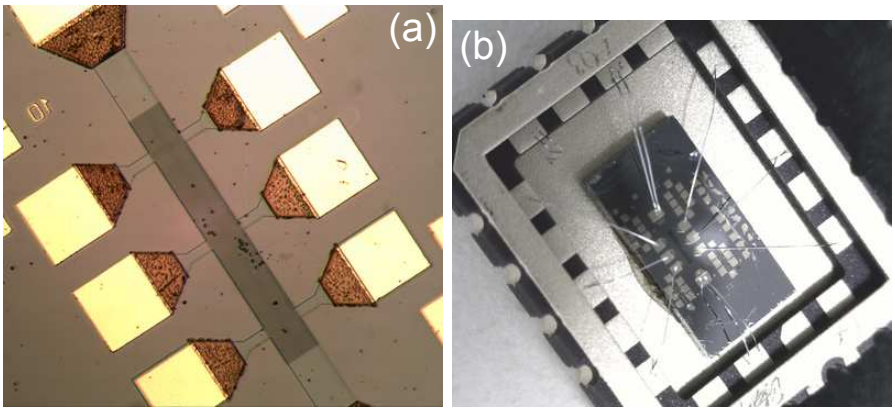

Figure 3.11: Finalization. (a) Image of a final Hall bar. On the main channel a hexagonal pattern is visible due to the change of surface optical properties. (b) Photography of a chip carrier bonded with a glued sample.

unpatterned Hall bar was probed to choose the most convenient wafers with respect to the carrier concentration and mobility. Several of them were used to study impact of patterning and surface etching on properties of 2DEG, as reported in chapter 4. Certain samples with hole-patterned Hall bar served for magneto-transport measurements on artificial graphene. For this purpose, we designed 100 μm wide and 600 μm long (unpatterned) Hall bars that have been first used to characterize the wafers and later on hexagonal patterning via etched holes was added.

In the future work, several concepts of sample architecture might be explored. In particular, special samples allowing both, optical as well as transport experiments can be prepared. In such a case, the whole area of the samples will be patterned and Hall bar structures will created locally by deep narrow ditches. In ideal case, both experiments can be performed simultaneously. If only transport experiments are of interest, significantly more advanced design can be used, as discussed in the next subsection.

3.4 Needle electrode

So-called "needle electrode" or "needle-like gate" design is a long term concept allowing us to change continuously and independently two principal parameters governing the artificial graphene – the effective potential $V_0 \sim \zeta$ (the criterion 1 started in the section 2.4) and the position of the Fermi level (criterion 2). The carrier concentration can be tuned using a back gate. If both other remaining criteria are satisfied (disorder and low B and T), the ideal configuration can be reached by varying V_0 and n just during an experiment. When successful, properties of artificial graphene should emerge.

Encouraged by promising results obtained on optical samples, we have started the first realization of such an advanced structure. Since every new technology is generally very time-consuming and to the end unpredictable, only an incomplete realization of gates can be presented here. No transport experiments have been done yet.

Schematically, the process is similar, nevertheless, more complicated than the creation of a simple Hall bar. This time, large holes for ohmic contacting are etched first through open windows in the positive resist layer (figure 3.12, step 1). Without any resist removal, the AuGeNi contact is deposited (step 2). After stripping the resist (step 3), we anneal contacts as described above and check that the 2DEG is well ohmically contacted. For this purpose, one can use a point-contacter that connects opposite AuGeNi gobbets and measures the resistance. It should exceed 10-20 kΩ at room temperature. It is followed by another etching of deep ditches, which separate newly created Hall bar from the other part of the sample (step 4). When successfully accomplished, the samples are again coated by another positive resist and holes are exposed on the main channel (step 5). Now, a thin adhesive layer of titan (10 nm) and a sufficiently thick layer of gold is deposited. That creates a gold plate with narrow needles over the Hall bar where the electrostatic effect of the plate is lightly screened by the polymer mask between needles (step 6). This part causes most of our technological obstacles as reported below. Instead of lift-off, another negative resist deposition follows (step 7) and all parts outside the Hall bar and bonding plates are removed by

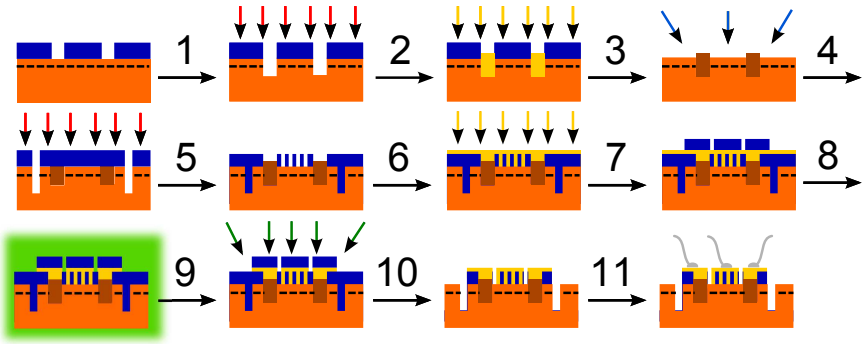

Figure 3.12: Process of needle gate creation. 2DEG is marked by the vertical solid line. Step 1: Etching of large holes for ohmic contacts, step 2: deposition of AuTi over the same (unremoved) mask, step 3: stripping of resist in acetone and annealing of contacts, step 4: another resist layer deposition, exposition and developing, followed by etching of deep ditches that separate the Hall bar from the rest of material, step 5: stripping the old resist and deposition of another one, area above ohmic contacts is opened, hole pattern above the main channel is exposed and developed, step 6: AuTi vapour deposition, step 7: deposition and lithography of negative resist that finally covers only the top gate (the main channel) and area around ohmic contacts (will form bonding facets), step 8: wet etching of gold and titan, steps 9 and 10: O_2 plasma etching of all uncovered resist, step 11: bonding of facets and contacting the top gate.

EBL. Using the solution of iodide in potassium iodide (KI), we wet etch the gold layer and using 40% HF with 40% NH_4F in the ratio 7:1 we dissolve the titanium layer, only the covered areas remain (step 8). Now, we proceed to the dry plasma exposition (oxygen plasma, 300 W, 500 Pa for 20 minutes) that lightly burn the rest of the resist and cannot destroy or lift-off the electrode, as the acetone bath would (steps 9 and 10). In figure 3.13, the final gated Hall bar is shown. Before the transport measurements, the gold contacting plates and the top gate are bonded to a chip carrier (step 11).

The missing experience with the preparation of a sophisticated gate lead to problems in the step 6. Some of them are easy to overcome – for example, the control of the pattern uniformity and the same length of all needles. In this case, we develop a procedure how to inspect the bottom of the electrode. The sample is put upside-down on a slightly heated Si wafer with deposited SU resist ($\sim 90°C$) that becomes gluey. After cooling down, when the sample surface is well glued, all is inserted into solution of 10% H_2SO_4 and 30% H_2O_2 for several hours. When all GaAs and AlGaAs is dissolved, the remaining resist between needles is removed in barrel O_2 plasma. We obtain the needle electrode nicely spread on a silicon wafer, figure 3.14(a), which allows us to examine the quality of needles using the electron microscope. In top view, one can observe their periodicity and thickness, see figure 3.14(b), the isometric orientation serves to inspect the length.

In our case, another problem emerged. As shown in figure 3.15(a) taken by the electron microscope, golden needles break and fall down on the surface if the resist filling the space between needles is burn-out. Such behaviour might mean that the AuTi deposition has not been uniform. The needle is not homogeneous

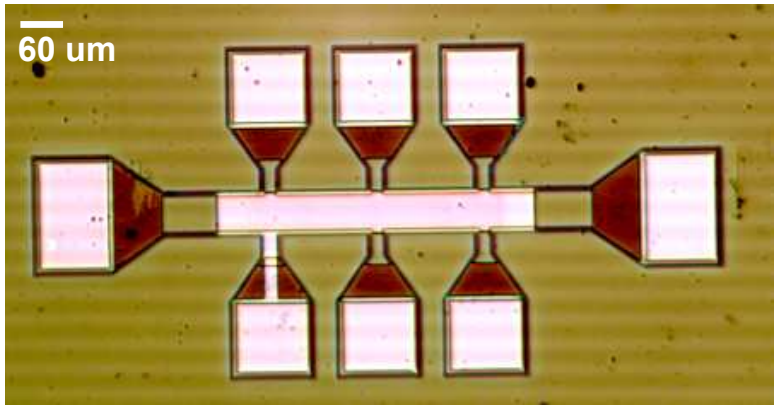

Figure 3.13: Optical microscope photography of a final Hall bar with a needle gate above the main channel. One of the facets, served early as a contact for the longitudinal resistance measurements, is now used as a gate control (lower left).

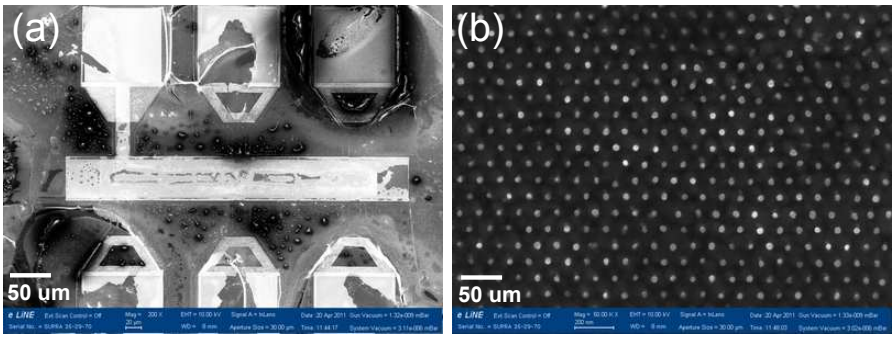

Figure 3.14: SEM images of bottom side of needle gate. (a): Overall view on the needle gate glued to a wafer, lightly damaged by the GaAs etching and transporting. (b): Detail on needle bottoms – still surrounded by the remaining resist.

along its length but constricted or even interrupted once or several times. Figure 3.15(b) shows that deposited gold forms surprisingly large grains, sometimes even larger than the diameter of the hole for the needle. Two solutions are suggested and currently explored – first, a Au-Ti-Au-Ti-Au sandwich structure could be deposited, since gold and titan have different lattice constant and grains could not grow up to this size, or second, another metal could be used for the gate – for example platinum, which does not create grains.

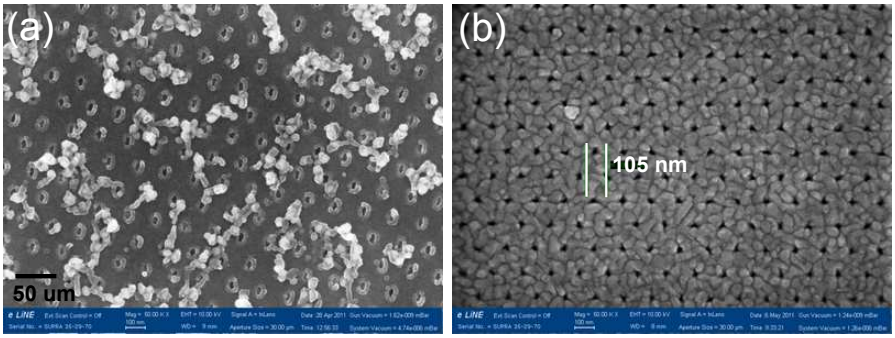

Figure 3.15: Bottom views on the needle gate after removal of the remaining resist. (a): All needles are broken and downfallen on the gold plate. (b): Comparison of the size of gold grains and the diameter of holes.

Along with the technology, a simple estimate of the potential created by needle electrodes might be useful. We have simplified the problem to one dimension and numerically solved the following Laplace equation

$$\Delta_{x,y}\Phi = 0, \tag{3.2}$$

where $\Delta_{x,y} = \frac{\partial^2}{\partial x^2} + \frac{\partial^2}{\partial y^2}$. There is only one boundary condition, the needle electrode keeps a final constant potential, see 3.16(a). We concentrated on region 40 nm below the needles, where 2DEG is located in a new generation of samples. The equi-potential curve near the 2DEG (dashed line) has a typical cosine profile. If one does not carry about the absolute value of the voltage on the gate, but only about the cosine amplitude introduced in this depth, several observations related to the electrode shape can be made. If the length of needles exceeds the distance between each other (i.e. the "lattice constant" a), the potential amplitude practically does not depend on this length. The ratio between a and the diameter of needles is crucial. Since the period a should be kept as low as possible (to get the Dirac cone higher in energy and to operate in higher concentrations), the only indeed tunable parameter is the needle diameter. The lowest technologically achievable needle thickness is 30 nm, which lead to the relative amplitude of several % of the mean value, see figure 3.16(b).

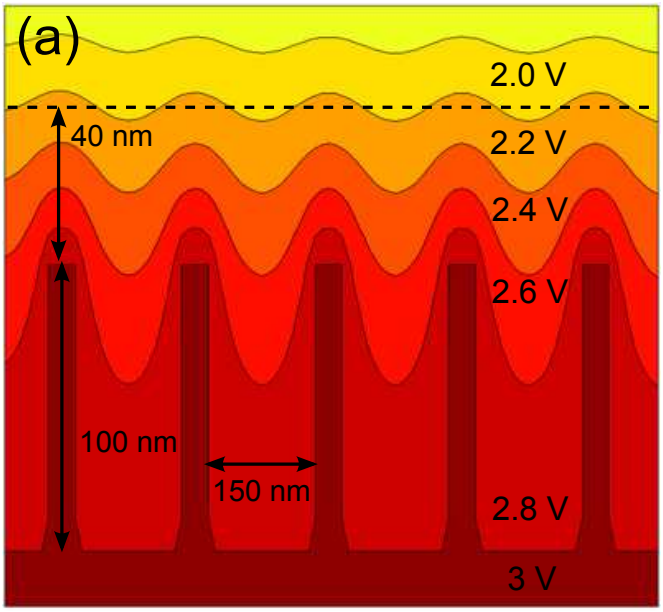

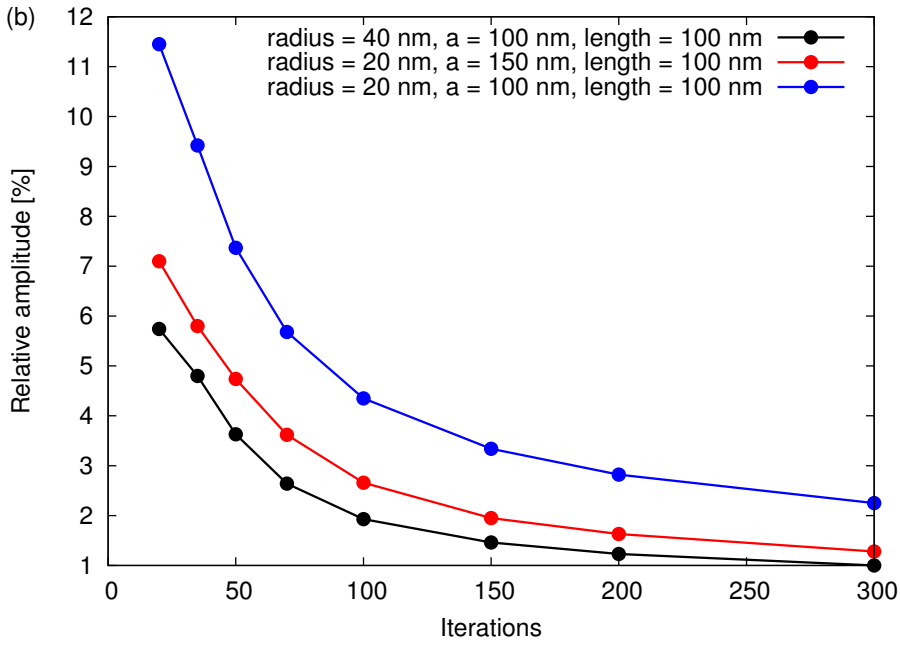

Figure 3.16: Visualization of the potential created by the needle electrode. (a): Solution of Laplace equation for marked design. Position of 2DEG is represented by the dashed line where a cosine-like dependence is evident. (b): Relative amplitude of the potential created in the depth of the 2DEG (40 nm) against the number of iteration. According to electrode configuration, several well converged values are shown. Unfortunately, the relative amplitude should reach several percentiles in accessible designs.

4. Experiments

In this chapter, we focus on three experimental methods that were used to probe a number of samples prepared by the dry etching process described in chapter 3. As optics, it mainly covers the far infra red (FIR) transmission Fourier spectroscopy of Landau levels and the photoluminescence (PL) spectroscopy of Landau levels, both in magnetic field. In the transport arrangement, we benefited from the low temperature electronic measurement of the quantum Hall effect (QHE) and the Shubnikov-de-Haas oscillations (SdHO) within the Hall bar geometry (as commented in the last chapter as well). Although these three experiments represent the main and very discussed part of the experimental work, other numerous non-trivial and time-consuming measurements had to be accomplished to support the presented ones. It concerns the transport characterization of every sample set, the probing of contact quality or checking technological troubles and difficulties. As that this work is not seen anytime, the author reminds it here.

The presented experimental work has been done in several institution within Europe. The FIR spectroscopy has been taken at National Laboratory of High Magnetic Fields in Grenoble with the dr. Milan Orlita's supervision, the photoluminescence spectroscopy at NEST Institute of Scuola Normale Superiore in Pisa under dr. Vittorio Pellegrini's supervision and the electronic transport at Institute of Physics at Academy of Science of Czech Republic with tight cooperation with dr. Vít Novák.

4.1 FIR: experimental background

Unlike other kinds of spectroscopy, the Fourier spectroscopy does not use a dispersion element, such is a grating or a prism, which spatially split the incident light by its wavelength, which is thus processed as monochromatic. Thanks to a numerical analysis, hereby Fourier transformation, a wide spectral range is obtained just after one scan of polychromatic light. In general, the Fourier transformation connects a time dependence with a frequency dependence of the signal intensity by the following expression

$$S(\omega) = Re \int_{-\infty}^{\infty} I(x) e^{2\pi i \ x\omega} d\omega. \tag{4.1}$$

The time dependence of the signal is obtained using the Michelson's interferometer. The main polychromatic beam is split into two branches by a beamsplitter, where the length of one of these branches is periodically modified by a moving mirror. Therefore, the resulting intensity after the interference depends on the Δx position of the mirror. The position is then easily connected with the time dependence with respect to the mirror speed. Applying the Fourier transformation, we get a spectral range where its length is defined by the maximal Δx and other optical aspects (characteristics of beamsplitters, light sources, windows etc.). The resolution of such a spectrum is closely connected with the discrete character of the problem. Only a finite number of mirror positions are taken into account, so the steps $n \cdot \delta x = \Delta x$ produce non-zero intervals in the spectral output, $m \cdot \delta\omega$. For further information, one refers to the author's bachelor thesis [12].

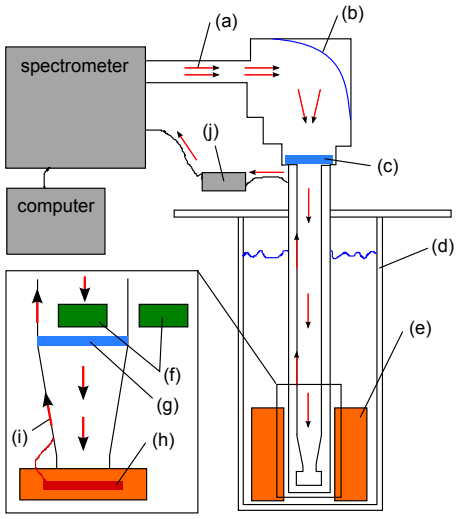

Figure 4.1: Scheme of the experimental setup. The radiation exits the spectrometer (a) and is focused by parabolic mirror (b) into the probe through entering window (c). The probe is placed in the cryostat (d) filled by liquid helium and pumped down to $T = 1.7$ K. The cryostat is equipped by superconducting coil (e), the sample (f) is placed in Faraday configuration. Here, the light transmits through the sample (f) or reference and continues to the input window (g) at the bolometer (h) where it is collected. Then wires (i) transfer the electric signal to the preamplificater (j) and further to the spectrometer/computer.

The used setup consisted of a Fourier spectrometer controlled by a computer and coupled to a probe plunged into a helium-pumped cryostat equipped by superconducting coils. The low energy edge of the used spectrometer was $\hbar\omega \approx 3$ meV and its resolution was mostly set to 0.125 meV. As a source of light, a mercury lamp and a globar were used, providing black body radiation with maxima at approximately 10 meV and 25 meV, respectively, as beamsplitter, two types were employed – T222 and Mesh250. The probe, represented in figure 4.1, was a tube equipped by a removable part supporting the sample, the detector and connecting electrical wires. The parabolic mirror focused the radiation into the tube through a white polyethylene window. The white window transmits a part of visible light, which excites the electron density in the quantum well (originally with very low carrier concentration due to the etching, for the quantification of this phenomenon, see section 4.4). If the black polyethylene is mounted, an optical fiber has to be used in to illuminate the sample and enhances the electron density. The second method was useful when the white window provides too high electron density and the sample did not fulfill the criterion 2 (see section 2.4). The light transmitted through the sample or reference is absorbed by the composite silicon bolometer. The signal is then amplified and processed by the computer. The used superconducting coil provides the field up to 13 T. The cryostat is filled by liquid helium that can be pumped down to the temperature of 1.7 K.

After the Fourier transformation of the obtained signal, a relative transmission $T(k, B)$ with respect to the spectrum taken at $B = 0$ T is calculeted

$$T = \frac{S(k, B)}{S(k, B = 0)} \tag{4.2}$$

At higher magnetic fields, the dependence of the bolometer on the applied field becomes relevant and can be corrected by reference spectra

$$T = \frac{S(k,B)/S_{\mathrm{ref}}(k,B)}{S(k,B=0)/S_{\mathrm{ref}}(k,B=0)} \tag{4.3}$$

The reference is mostly a simple hole in metal plate with a radius comparable to the sample size.

4.2 FIR: results and discussion

From a number of samples probed by the FIR transmission spectroscopy, the convenient carrier density has been found in samples: A, B and C, as introduced in the end of section 3.2 and in table 3.1. These are characteristics taken from parent wafers before the processing. After several first measurements, we found that electron densities have considerably decreased in majority of samples after the processing. To increase the carrier density and to get into a predicted range of suitable concentrations, we used the white polyethylene window or optical fiber illumination by the visible light. Such an additional excitation (permanent or short flashed) produced a new (quasi-)stable density. These new electron concentrations have been estimated from shape of cyclotron response, as described in appendix A. The obtained values are summarized in the following table 4.1.

Sample	wafer	n ($\times 10^{11}$ cm^{-2})	μ ($\times 10^3$ cm^2/(V·s)	$d_{\mathrm{dots}}/d_{\mathrm{2DEG}}$ (nm)
A	1	0.8	130	15/100
B	1	0.8	110	20/100
C	2	1.8	95	48/115

Table 4.1: Characteristics of samples under experimental conditions. Values were inferred from shape analysis of transmission spectra, see appendix A. We note that new electron densities are very close to the range 0.6 – 0.7 cm^{-2} predicted by criterion 2, see the end of section 2.4, as well as mobilities $> 10^5$ cm^2/(V·s), criterion 3.

To complete the final arrangement of samples, an interference problem has to be discussed. As we used the wavelength of hundreds of μm, the Fabry-Perot-like interference appeared between back and front side of sample and caused a disturbing noise over all spectral range of interest. Unfortunately, an additional grating and wedging of back side was not very efficient. However, the followed effect was mostly more intensive than this interference background.

Now, we proceed to the probing of cyclotron resonance by Fourier spectroscopy in far infrared spectral range. A standard spectrum of an unpatterned sample, our reference, shows well-defined Lorentzian peaks. Since the Landau level spectrum is

$$E_c(\omega, n) = \hbar\omega_c(n + 1/2) = \hbar\frac{eB}{m^*}(n + 1/2) \tag{4.4}$$

and the allowed transition respects the rule $\Delta n = \pm 1$, the energy consumed by the experimentally traced excitation is $\Delta E = \hbar\omega_c$. Indeed, the real dependence of energetic position of cyclotron peak is linear on the magnetic field – as one can see in figure 4.2.

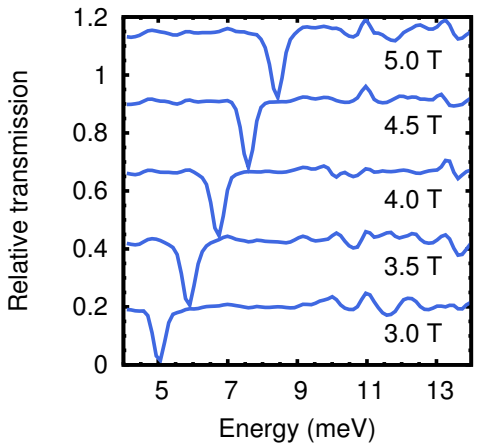

Figure 4.2: FIR transmission spectra for unmodulated reference sample. Single Lorentzian peak lies exactly on $\hbar\omega_c$ and no splitting appears, as commonly observed.

Our examined patterned samples exhibit a different behaviour. As shown in figure 4.3, an obvious double or multiple peak response appears at low magnetic field. These characteristic modes occur at energies above $\hbar\omega_c$ and their deviation from the main transition peak becomes stronger with decreasing B. This splitting of the cyclotron resonance mode into more components vanishes in high fields, but it happens at different fields in different samples, i.e., the splitting definitely depends on the strength of modulation potential (different depth of etched holes).

Without doubt, the lateral superlattice affects noticeably the spectra. Although the effect produces the internal double or multiple mode structure of the original single peak, the changes are not so dramatical as we would expect in case of clear formation of Dirac-like electronic bands. Regarding relatively small deviations from linear tendency of ideal 2DEG and the vanishing of the effect as $1/B$ in limit of high magnetic field, even a brief observation of spectra suggests a perturbative behaviour. Thus, the potential generated by the superlattice creates a considerably weaker effect than Landau level quantization, its strength V_0 becomes only a perturbation comparing to the level spacing $\hbar\omega_c$, suggesting $V_0/\hbar\omega_c$ as a small parameter. Therefore, due to the perturbative behaviour of observed effect of our modulation, due to the breaking the criterion 4 (low magnetic field and low energy spectral range) started in section 2.4, we fail to observe graphene-like physics in our samples.

However, the perturbative effect of the superlattice can be nevertheless exploited. Developing a perturbation theory can provide relevant conclusions about present effective potential. Such knowledge is very useful for design of new sets of samples in future. Benefiting from the perturbation approach of X. F.Wang, P. Vasilopoulos et al. [5], the unperturbed energies $E_n = \hbar\omega_c(n + 1/2)$ are, due to the hexagonal potential, broadened into bands

$$E_{n,\kappa_x,\kappa_y} = E_n + V_0 e^{-2\beta^2/3} L_n(4\beta^2/3) \times \left\{ 2\cos\beta^2(\kappa_x + \tfrac{1}{\sqrt{3}})\cos\tfrac{\beta^2\kappa_y}{\sqrt{3}} + \cos\tfrac{2\beta^2\kappa_y}{\sqrt{3}} \right\} \tag{4.5}$$

where $\beta^2 = 2\pi^2\ell_0^2/a^2$, $\ell_0^2 = \hbar/eB$ and $\vec{\kappa}$ belongs to the hexagonal first magnetic Brillouin zone (see the visualisation in figure 4.5a). Now, energies of dipole-

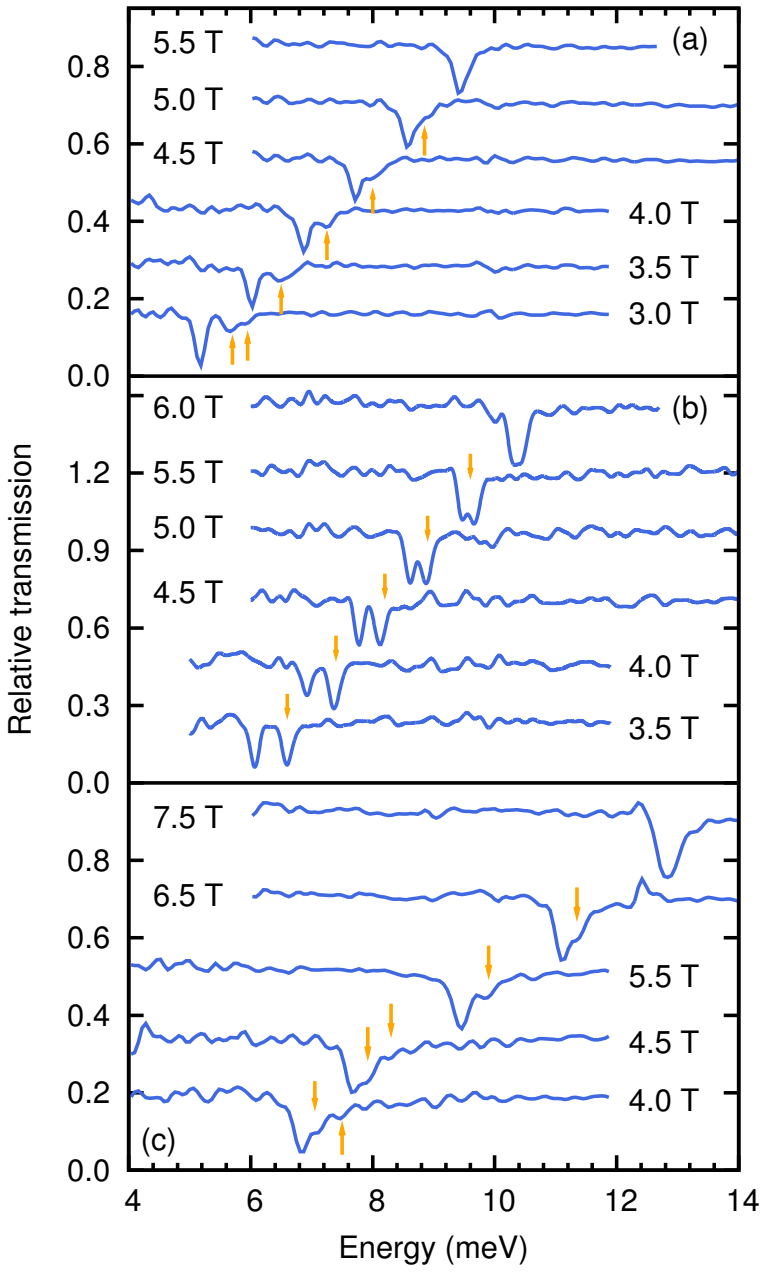

Figure 4.3: Relative magneto-transmission spectra of studied samples A ($d_{\text{holes}} \approx 15 - 25$ nm, $d_{\text{2DEG}} = 100$ nm), B ($d_{\text{holes}} = 20$ nm, $d_{\text{2DEG}} = 100$ nm) and C ($d_{\text{holes}} = 48$ nm, $d_{\text{2DEG}} = 115$ nm) in parts (a), (b) and (c), respectively. The multi-mode character of cyclotron resonance absorption vanishes with the increasing magnetic field at $B \approx 5, 6$ and 7 T in the sample A, B and C, respectively. All spectra are shifted vertically for clarity by 0.15, 0.25 and 0.2, respectively.

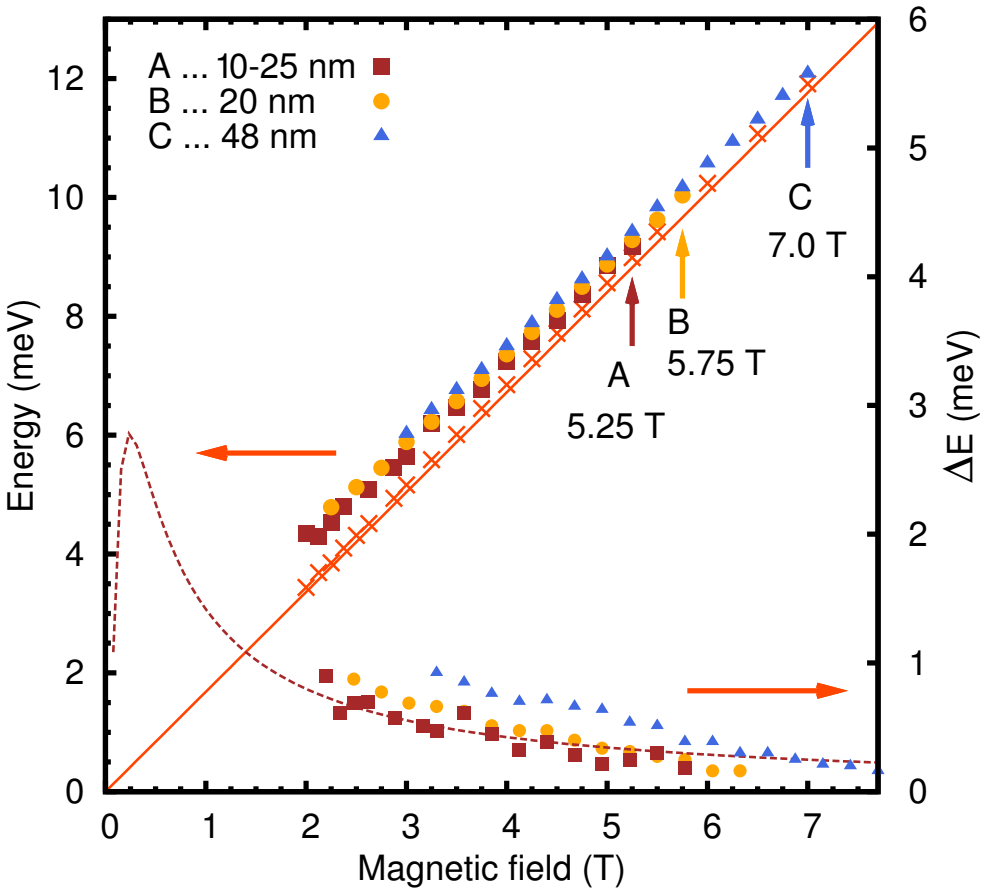

Figure 4.4: Fanchart of transitions observed in studied specimens A, B and C, cf. in figure 4.3 (left vertical axis): Vertical arrows depict magnetic fields at which the multi-mode character of CR absorption vanishes. The position of the main CR peak in spectra taken on the sample A is marked by crosses. The straight line corresponds to the theoretical CR-line position with an effective mass of $m^* = 0.067m_0$, which has been derived from measurements on reference (unpatterned) sample. Lower part of the figure (right vertical axis) shows derived values of CR-line splitting ΔE. The dashed line corresponds to the fit of ΔE for the sample A based on the theoretical model discussed in the text.

allowed optical transitions are $\Delta E_{n+1,n} = E_{n+1,\kappa_x,\kappa_y} - E_{n,\kappa_x,\kappa_y}$, which can be rewritten by recurrence formulae for Laguerre polynomials L_n, see reference [20]. As we deal with relatively low electron densities and filling factors $\nu = nh/eB < 2$ (that means only the first Landau level is occupied for $B > 1.7$), we may consider $n = 0$ only. Since $L(x)_1 - L(x)_0 = -x$, the term $\Delta E_{1,0}$ becomes easy to express

$$\Delta E_{1,0} = E_{1,\kappa_x,\kappa_y} - E_{0,\kappa_x,\kappa_y} = \hbar\omega_c - \frac{4}{3} V_0 \beta^2 e^{-2\beta^2/3} b(\kappa_x, \kappa_y) \tag{4.6}$$

where $b(\kappa_x, \kappa_y)$ denotes the curled bracket of Eq. (4.5).

The optical transition energy $\Delta E_{1,0}$ enters the transition probability $P_{0\to1}(\omega)$ as: [21]

$$P_{0\to1}(\omega) = \frac{2\pi}{\hbar} \int \frac{d^2\kappa}{(2\pi)^2} |\langle 1, \kappa_x, \kappa_y | p_{0\to1} | 0, \kappa_x, \kappa_y \rangle|^2 \delta(\Delta E_{1,0} - \hbar\omega), \tag{4.7}$$

where ω is the photon energy and $p_{0\to1}$ is momentum operator containing the pre-term $e\vec{A}/m$. If we neglect this dipole transition matrix element, the observable optical characteristic features correspond to van Hove singularities in the joint density of states (jDOS)

$$J_{0\to1}(\omega) = \int \frac{d^2\kappa}{(2\pi)^2} \delta(\Delta E_{1,0} - \hbar\omega) f_{0,\kappa_x,\kappa_y} (1 - f_{1,\kappa_x,\kappa_y}) \tag{4.8}$$

which reflects the occupation of involved electronic states: the initial state $n = 0$ occupied and the final $n = 1$ empty, for each $\vec{\kappa}$. Such condition is expressed by the Fermi-Dirac occupation factor f. At filling factor $\nu < 2$, $P_{0\to1}(\omega)$ becomes a band with a width

$$w(B) = 6 V_0 \beta^2 e^{-2\beta^2/3} \tag{4.9}$$

that depends on the magnetic field only. The band is generally centered around the cyclotron energy $\hbar\omega = \hbar\omega_c$. If the ν decreases, the width decreases as well since electrons occupy smaller and smaller area of magnetic Brillouin zone of the first Landau level ($n = 0$). In the limit of high magnetic fields, only a small part of the $\vec{\kappa}$-space is occupied. The band is transformed back into delta function $\delta(\omega_c)$ and only transition with $\omega = \omega_c$ are allowed.

Equation (4.9) provides a reasonable basis for interpretation of the evolution of peak-to-peak distances presented in figure 4.3. These data follow the magnetic field dependence of $w(B)$ allowing to extract the values of V_0 for the particular sample. It should be noted that the peak splitting observed in experiments probably does not correspond to the full width w as calculated using equation (4.9) because the lower edge of the absorption band is suppressed for $\nu < 2$ (this is the case of $B > 2$ T and $n < 10^{11}\mathrm{cm}^{-2}$).

However, other features of the absorption band also scale as $cw(B)$, where $0 < c < 1$ is a constant. These features, i.e., the lower and upper edge and logarithmic singularity in the middle of band, are shown in Figure 4.5a,b and correspond to the indicated transitions of the broadened Landau bands E_{n,κ_x,κ_y}, i.e., γ, α and β, respectively. The first states that become depopulated upon the filling factor dropping below two (that is when the magnetic field is increased) are those close to the top of the band. Hence, the transitions α are the first ones to disappear from the absorption spectra. We note that the Zeeman splitting ε_z is roughly $50\times$ lower than the LL broadening at $B = 2$ T, $\varepsilon_z = ge\hbar/2m_0B \approx 0.05$meV.

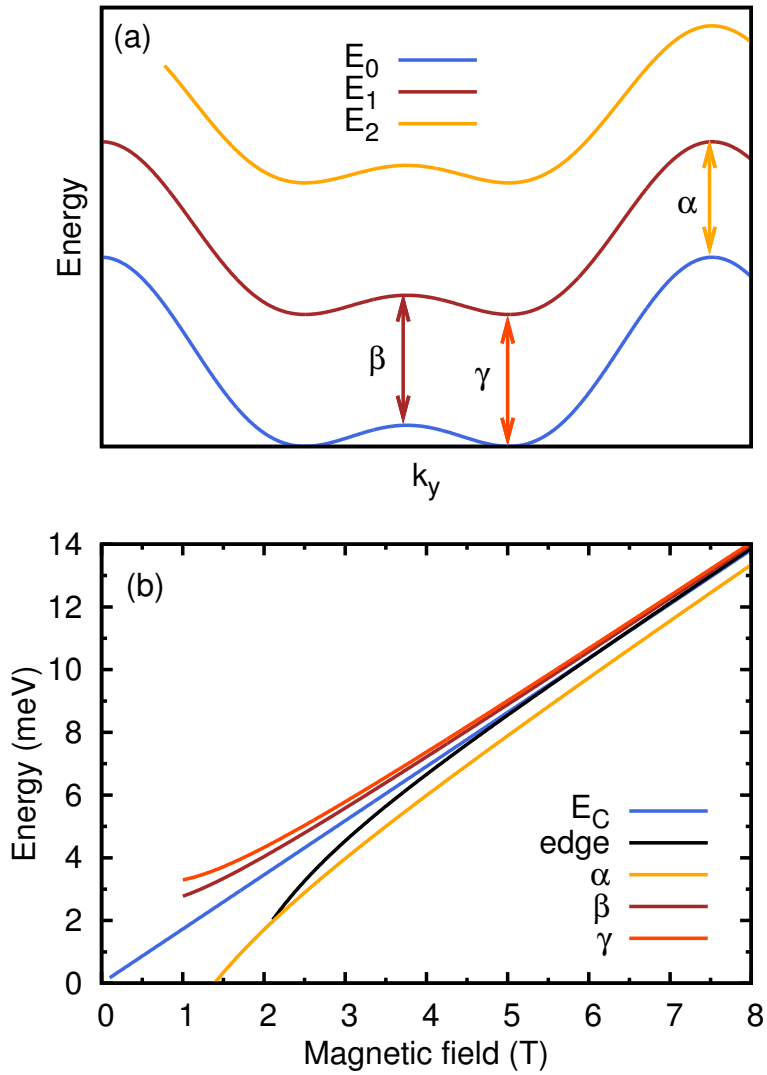

Figure 4.5: Part (a): Schematic plot of three lowest lying Landau levels broadened into bands due to the lateral hexagonal modulation. Transitions originating in van Hove singularities in the joint density of states $J_{0\to1}(\omega)$ are marked by α, β and γ. Whereas α and γ are the band edges, β is the logarithmic singularity corresponding to the saddle point between two neighbouring minima of ΔE_{10} in $\vec{\kappa}$-space (as shown in the top panel). Part (b): Magnetic field dependence of α, β, γ jDOS singularities. "Edge" shows the lowest in energy allowed transition, as defined by the position of the Fermi level (for $n = 5.0 \times 10^{10}$ cm^{-2}). $E_c = \hbar\omega_c$ is the cyclotron energy.

For the remaining two features β and γ, our form of the potential $V(x, y)$ would imply $c = 1/9$. However, we believe that the feature β which leads to a logarithmic van Hove singularity in the jDOS, may be easily smeared out. Another candidate for an absorption feature is the Fermi edge (transitions from the states close to E_F to the next Landau band) which is also shown in the lower panel of Fig. 4.5. Although the Fermi edge does not precisely scale with $w(B)$, it always appears at frequencies $\omega \approx \omega_c$ hence $c \approx 1/3$. The values of V_0 inferred from fitting our data, assuming that the splitting of the CR mode corresponds to $\frac{1}{3}w(B)$, are shown in table 4.2 alongside with the corresponding ζ. As can be observed, the obtained values match surprisingly well into the range required by the criterion 1 ($0.5 < \zeta < 4.0$, see section 2.4), but on the other hand, the superlattice effect is still a perturbation compared to Landau level quantization. In this meaning, reduction of superlattice constant a is convenient since such system would lead to higher ζ (and n) and more favourable ratio $V_0/\hbar\omega_c$.

Sample	d_{holes}	d_{2DEG}	V_0	ζ
A	15-25	100	2.2 meV	2.4
B	20	100	3.5 meV	3.1
C	48	115	4 meV	3.6

Table 4.2: Potential amplitude V_0 and the corresponding dimensionless parameter ζ for samples A, B and C as derived by fitting our data using $\frac{1}{3}w(B)$, equation (4.9). The etching depths and the distances from 2DEG to the sample surface are also listed.

The double peak feature observed at lower magnetic fields is also a reminiscent of confined-magneto-plasmons (CMP) [22]. This fact motivated us to perform a control experiment that would exclude this possible interpretation. In an infinite 2DEG system at zero magnetic field, particular plasma oscillations can be observed [23]. These oscillations of wavelength $\lambda = 2\pi/q$ are described by the dispersion $\omega_p(q) = \sqrt{e^2nq/2m^*\varepsilon_r\varepsilon_0}$. According to previous experiments [24], the dispersion in non-zero magnetic field is governed by a combination of cyclotron frequency ω_c and CMP frequency $\omega_p(q)$, $\sqrt{\omega_c^2 + \omega_p^2(q)}$. In a metal stripe of width W, the wave-vector is given by $q = \pi/W$. Other numerical simulation [25] show, in fact, whole series of CMP modes at frequencies $\omega > \omega_c$ that corresponds to integer multiples of basic wave-vector $q = \pi/W$.

Now, if we consider our hexagonal modulation as an array of stripes with $W = a$, the fundamental energy of first CMP mode can be, in a bold approximation, estimated roughly as

$$\omega_{CPM} = \sqrt{\omega_c^2 + \frac{\pi e^2 n}{2m^* a\varepsilon_r\varepsilon_0}} \approx \omega_c + \frac{\pi en}{4Ba\varepsilon_r\varepsilon_0}. \tag{4.10}$$

Here, a first hesitation starts when one is able to fit the formula (4.10) to our data surprisingly well, but the needed carrier density is $n \approx 2.5 \times 10^{10}$ cm^{-2}, thus a density four times smaller then is present in tested samples. To make us sure that the CMP dependencies look similar only accidentally, we performed the following experiment. The sample B was successively illuminated by optical fiber to excite more electrons to the 2DEG layer and its FIR response was measured after each step. As can be seen in figure 4.6, the peak splitting obviously decreased as

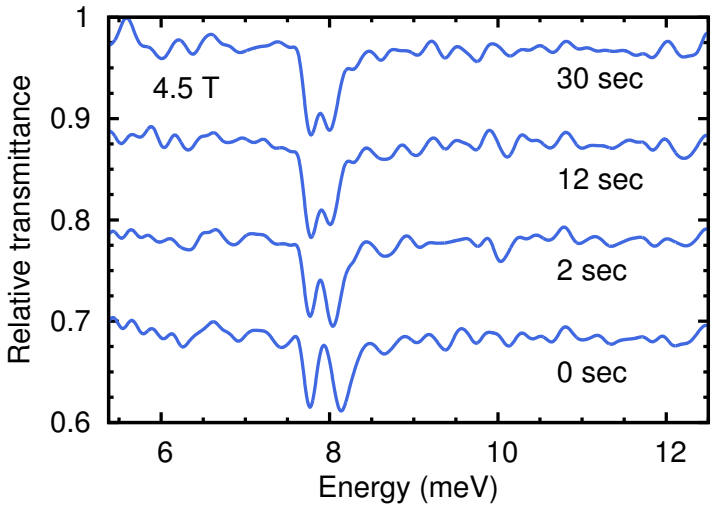

Figure 4.6: Magneto-transmission spectra taken on the sample B at $B = 4.5$ T and four different carrier concentrations. The density has been subsequently increased by exposing the sample to visible light for the indicated times, where corresponding concentrations are 7.0×10^{10}, 8.0×10^{10}, 9.0×10^{10} for additional illumination time 0, 2, 12 seconds, respectively. The highest illumination does not produce any increase of density since the system is already saturated. The spacing of observed modes clearly decreases with the carrier density. No other reaction to the highest illumination underlines the right correlation between the splitting and the concentration. The spectra are shifted vertically for clarity.

the density increased (the true correlation between the illumination and electron density was proved by fitting the spectra shapes using the numerical method described in appendix A). However, equation (4.10) fails to explain the observed behaviour whereas according to CMP theory, $\omega_{CPM} \sim \sqrt{n}$. Notwithstanding that the formula is derived from a very approximative approach, the observed contra-variant tendency of $\omega_p(n)$ in theory and in experiment considerably makes the CMP theory unreliable for this purpose.

Concluding this section, FIR transmission spectroscopy revealed a multi-mode cyclotron response as a clear effect of lateral superlattice, nevertheless, the experiment did not disclose any evidence of Dirac-like electronic bandstructure due to the small parameter $V_0/\hbar\omega_c$ (criterion 4 not fulfilled). The perturbative character allowed us to find a correlation between the depth of holes and the effective potential V_0, necessary for any theoretical estimate. The lesson taken from the experiment suggests that a reduction superlattice constant a would be best way for our future work.

4.3 Photoluminescence

Samples B and C were also probed by photoluminescence (PL) spectroscopy with the aim of enlarging the spectral range and uncover the behaviour bellow 2 T. Samples were placed into a cryostat equipped by an incoming and outcoming window, a movable holder for samples, CCD infrared camera to control the sample position and a system of lens and other optical elements. The near infrared signal

was generated in prepumped laser at wavelength $\lambda = 797$ nm (below the band gap od $Al_{0.33}Ga_{0.66}As$). After exit from the resonator, the light continues through focusing and guiding elements, and is reaching a neutral gray filter which reduces the laser power to $P \approx 50$ μW. A larger value might heat the sample. When the light comes into the cryostat and is absorbed by the sample, it produces an excitation of electrons from valence band to a higher part of the conduction band (and creates pairs "electron-hole"). Thanks to intraband relaxations, excited elec-

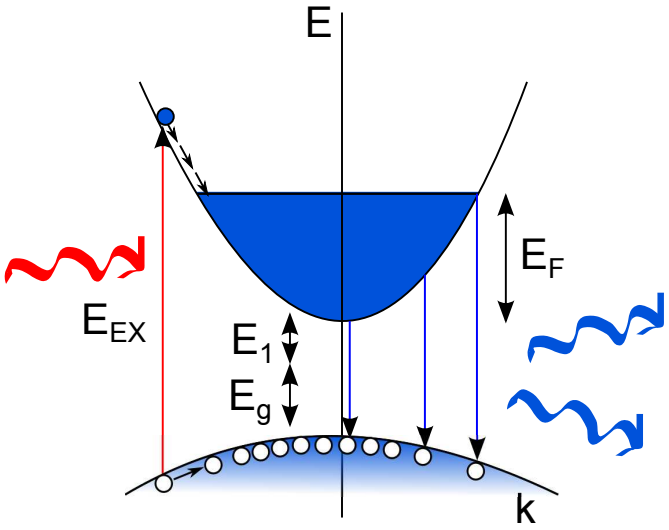

Figure 4.7: Scheme of photoluminescence process. Incoming light (red colored) causes an excitation and hole-electron pair creating. The excited electron relax to lower energies in conduction band, from where it recombines with a hole and emit diffusive light (blue colored). Quasi-stable Fermi level position is then related to the width of PL spectra at zero magnetic field.

trons termalize, analogically in the valence band. The inter band recombinations of electrons and holes is referred-to as luminescence. Unlike the incident laser beam, the emission light is isotropic. Thereby, it is necessary to tilt the sample holder which reflects the incident beam out of the next optical way. The emission light continues then out of cryostat and is analyzed by a grating spectrometer, having spectral range $\Delta E \approx 8$ meV, i.e., $\Delta\lambda \approx 4$ nm.

An example of PL spectra for sample B in the range of fields $0 < B < 3$ T is shown in figure 4.8. Before further comments, let us focus now on the spectrum at zero magnetic field. Unlike the FIR experiments, where the determination of carrier concentration requires the fitting of spectra and analyzing their area (see appendix A), the PL provides an easy method how to define the electron (and as well as hole) density. Since before excitation, the quantum well occurs a low electron concentration, after excitation the density of electrons exceeds the density of holes. In such case, the spectral width of PL response, would be limited by holes distribution in the valence band. However, the valence band is usually full of disorder states where a hole can be localized. As it is spatially confined, its wave packet is wide spread over $\vec{k}$-space and thus it can recombine with electron at every $\vec{k}$. Therefore, the concentration of holes is not a limiting factor and the width of PL spectrum corresponds to the energy position of Fermi level (calculating from the bottom of the conduction band), as schemed in figure 4.7. Assuming now

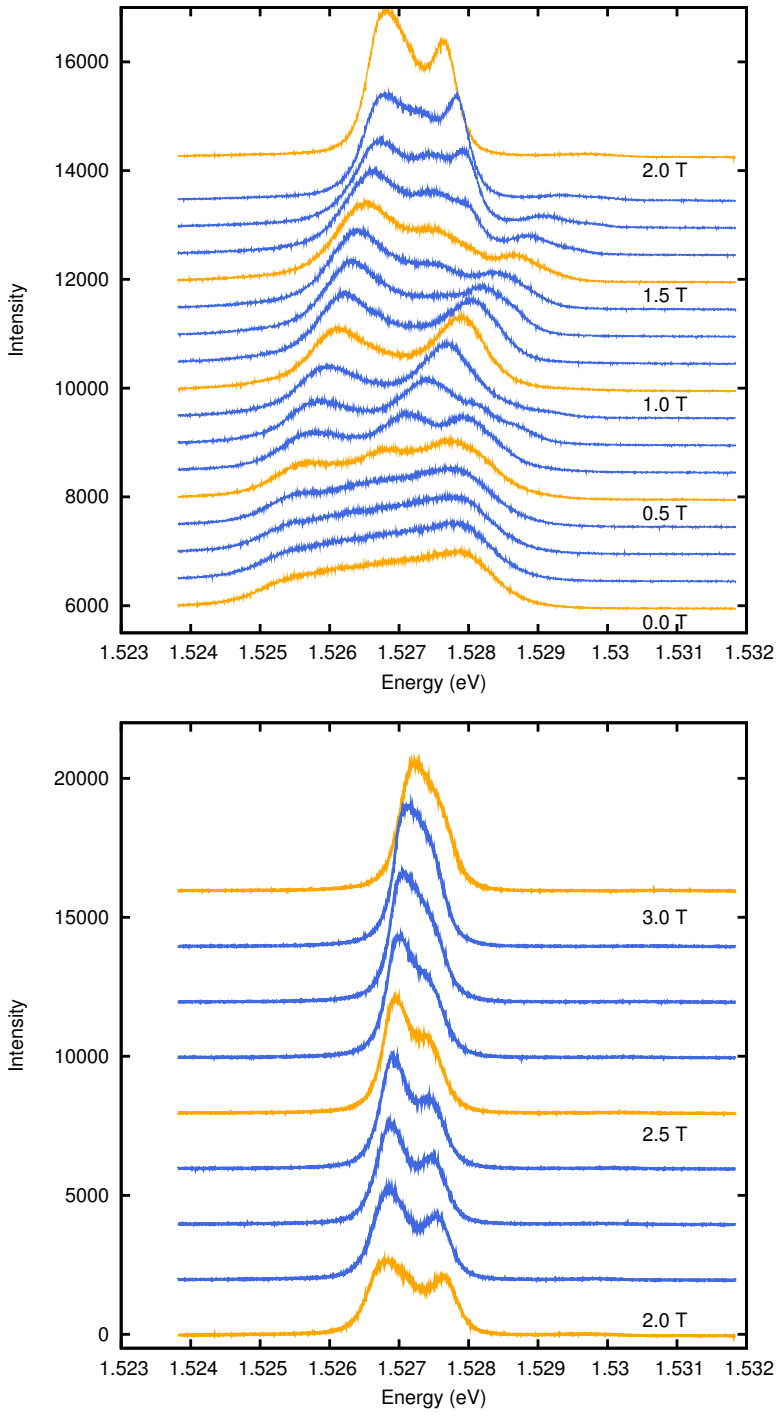

Figure 4.8: Photoluminescence spectra in magnetic range $0 < B < 2$ T (upper) and $2 < B < 3$ T (lower). Splitting due to the superlattice effect appears at ≈ 3 T as a obvious double peak feature. Orange curves designate 0.5 T steps.

that the 2DEG is ideal and its dispersion is completely parabolic, we determine the carrier density dn thanks to the known density of states in 2DEG as follows (including spin degeneracy)

$$dn = \mathrm{DOS}(\varepsilon)d\varepsilon = \frac{m^*}{\pi\hbar^2}E_F. \tag{4.11}$$

According to the spectrum at $B = 0$ T, whereof width is approximatively 3 meV, we obtain $dn \equiv n \approx 0.8 \times 10^{10}$ cm^{-2}. So very similar concentration as observed in FIR experiments. It is necessary to note here that found n is not the dark concentration present in the sample. In the same way as the concentration in FIR was determined by additional illumination by visible light, the density in PL is a quasi-equilibrium of pumping excitation and recombination. However, it represent the actual concentration during the experiment, so that experimental conditions can be, in such meaning, supposed as very similar.

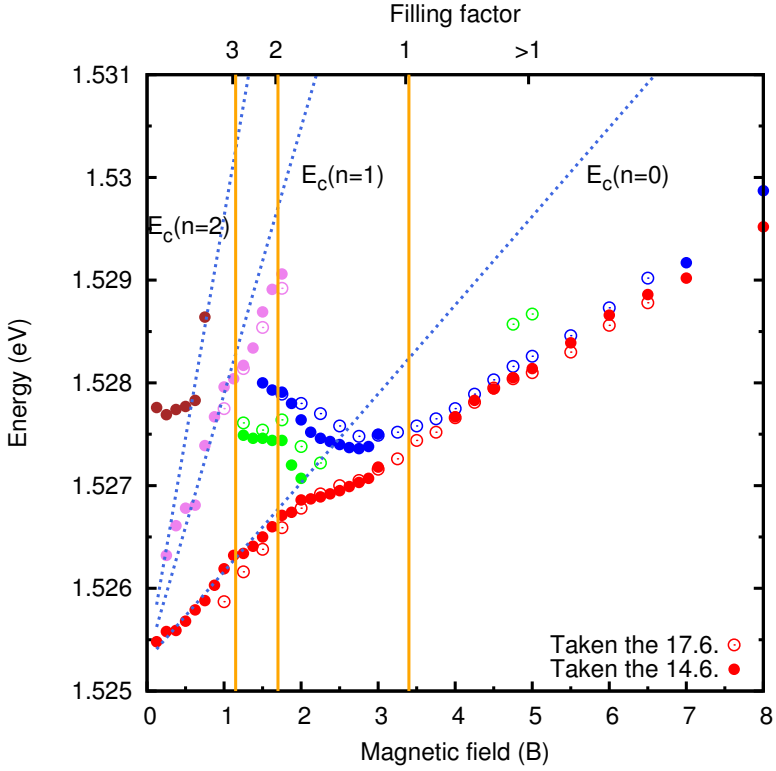

Figure 4.9: Fanchart of transitions in PL spectra. Filled and empty point denote peaks (taken in two days), dashed line represent Landau levels in magnetic field and orange vertical line the boundary between different filling factors. A significant splitting of the transition from Landau level $n = 0$ (red points) is obvious at two points.

In overall view on presented data – now in nonzero magnetic field (so Landau levels are forming), we immediately find a strong and obvious splitting of main PL peak (corresponding to recombination from $n = 0$ Landau level) at 3 T and below, down to 1.5 T. Another branch appearing at 1.5 T corresponds to the second Landau level ($n = 1$), and the feature below 0.625 T may be a signature of the third one. Specific positions of peaks are displayed in figure 4.9. In this fanchart, full and empty point represent two successive independent measurements, dashed

lines are theoretic assumptions of Landau level evolution in magnetic field

$$E_{n=0} = E_g + E_1 + E_1' + E_c = E_g + \frac{\hbar^2\pi^2}{2m_e^* d^2} + \frac{\hbar^2\pi^2}{2m_h^* d^2} + \hbar eB\left(\frac{1}{m_e^*} + \frac{1}{m_h^*}\right), \quad (4.12)$$

where $E_g \approx 1.52$ eV is bandgap at 1.7 K, E_1 and E_1' are ground states in quantum well for electrons and heavy holes and $d = 20$ nm is the width of quantum well. Vertical orange lines separate different filling factors in the system (top axis). Red points designate main PL peak which is then split (blue points). Green points may mean another splitting connected with other jDOS features introduced in the previous section. Violet points then well describe the second Landau level evolution followed by brawn one performing a strange behaviour close to the third Landau level position. That can be, however, an artifact resulting from complicated decomposition of spectra at low fields.

In summary, the sample B exhibits the same effect of the lateral superlattice in its PL spectrum, and can be interpreted in the same way as results in previous section 4.2. The amplitude of splitting at 2 T, for example, is the same as the inferred form FIR data, i.e., ~ 1 meV.

Besides the splitting, supporting our interpretation, the PL data show another expected behaviour – the position of main peak (red points) does not follow the theoretic tendency in magnetic field above 2 T, so approximatively below filling factor $\nu < 2$. The slope of this tendency is considerably smaller. Similar phenomena can be seen, in careful view, in violet point at $\nu < 3$. Such a behaviour has been observed in high magnetic field in many cases, for example [26], nevertheless, the phenomena has not been theoretically explained up to present day.

4.4 Transport

Transport experiments were the corner-stone of our technological preparation of samples. Not very time-consuming measurement in low temperatures provides fast and easy characterization of samples, following parameters like the electron density, mobility or conductivity of 2DEG layer. In this sense, these experiments were often accomplished during the fabrication phase. After it, when optical measurement are dominating the experimental work, the transport served as an additional method to verify wafer characteristics when processed. The electronic transport will become very useful at the moment when needle-gated samples are prepared. Then, the transport will be the only and powerful experimental method.

With respect to relatively low carrier concentration in optical samples (without additional illumination), we wondered what was the effect of etching holes on the average carrier density in the quantum well. We started with already contacted and prepared samples with a Hall bar design – but without any patterning. For these samples, quantum Hall effect (QHE) and Shubnikov-de Haas oscillations (SdHO) were measured. Then, an additional nanolithographical patterning was added, as described in details in chapter 3. In next measurements on these structures, we searched for changes in SdHO.

In fact, minima in SdHO (ideally, zero longitudinal resistivity) appear when the transport skips from diffusive to ballistic. In this situation, the current is

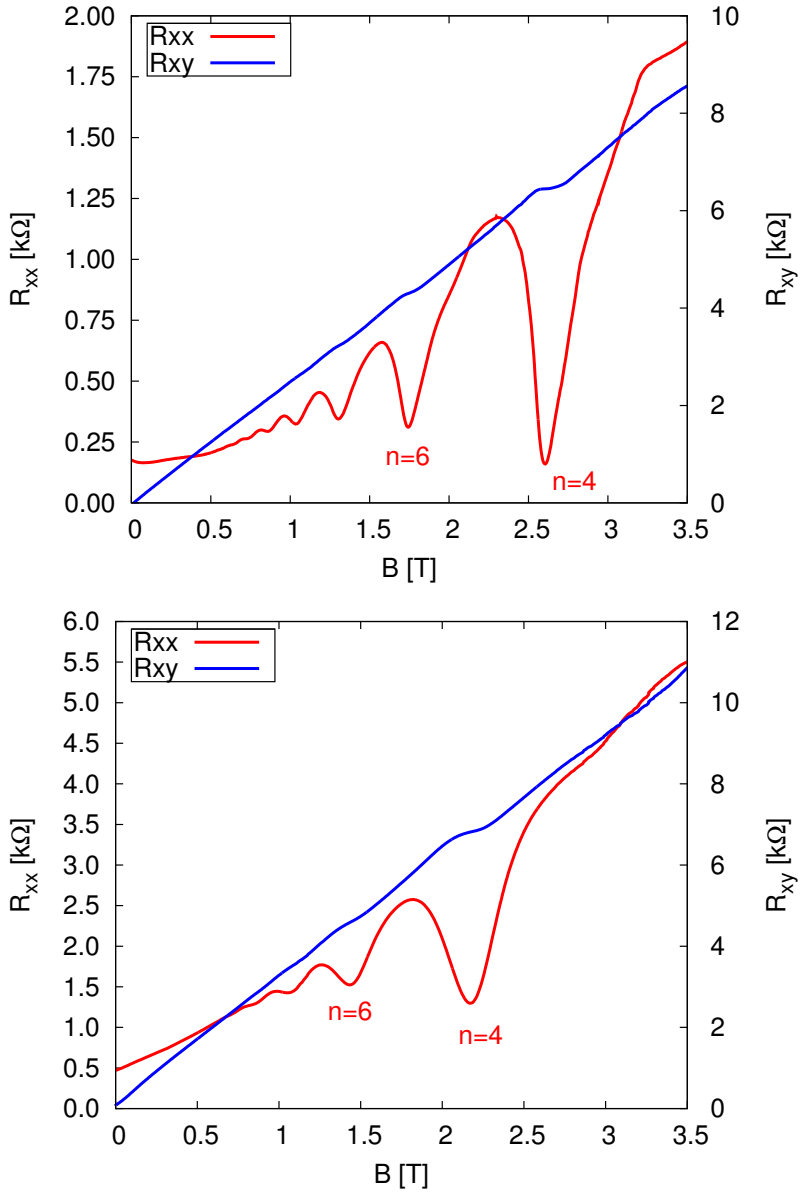

Figure 4.10: Electronic transport measurement on sample 1E5 before (upper) and after hole-processing (bottom). Blue lines designate QHE evolution in B, the red ones the SdHO. The magnetic fields at the fourth minimum indicate the actual electron density, while the value of SdHO at $B = 0$ corresponds tightly with 2DEG mobility. The slope of QHE evolution, disregarding plateaux, contributes carrier density as well. Comparing two graphs, a considerable decrease of the concentration is remarkable, as well as the change of mobility (see the corresponding text).

lead by electrons in edge states, creating oriented ballistic channels, without real possibility to get to the opposite channel. That results in the absence of electron backscattering which, in general, produces a non-zero resistivity (as is typical in diffusive transport). The condition for such a regime is similar as in case of QHE, see equation 1.6 on page 6 – it appears when the Fermi level is between Landau level, lying on localized states. Since the density of states for one level is eB/h, the filling factor (without spin degeneracy) can be written as

$$\nu = \frac{nh}{eB} \quad \Rightarrow \quad n = \frac{\nu e}{h} B. \tag{4.13}$$

For $\nu = 4$, the prefactor $\nu e/h \approx 10^{11}$ cm^{-2}T^{-1}. The fact means that the magnetic field in Tesla, corresponding to the fourth minimum of SdHO, indicates already the density of carriers in units of $\times 10^{11}$ cm^{-2}. The fourth minimum is easy to find since the ratio between magnetic field of each two neighbouring minima is the inverse ratio of their filling factors. One should note that we have to count the filling factor only in even numbers since the spin degeneracy fill each Landau level by a twice as large n. Another method how to find the density uses the Hall resistivity – at low magnetic fields, its slope is connected with n as follows

$$U_{xy} = R_H B I_{xx} = \frac{1}{ne} B I_{xx}. \tag{4.14}$$

All results were inferred using both methods, if the data are available.

Sample	n_{etch} ($\times 10^{11}$ cm^{-2})	n_{orig}	fall	h_{dots}/2DEG (nm)
1E2	1.9	2.8	32%	80/210
1E3	1.9	2.7	30%	85/210
1E5	2.1	2.6	20%	100/210

Table 4.3: Decrease of the electron density in three control samples – by 20–30% in all cases. However, the fall-down is not easily predictable since the relative depth of holes does not determine the effect properly. Probably, it depends on many other factors.

A typical example of magneto-transport experiment is shown in figure 4.10. In the upper part, a typical transport of unpatterned sample is presented – the red line corresponds to SdHO and blue one to QHE with obvious Hall plateaux. The fourth minimum indicates $n \approx 1.6 \times 10^{11}$ cm^{-2}. In the lower panel, the same sample with 100 nm deep holes (and 210 nm deep 2DEG) occurs very similar behaviour. The equivalent density is lower, as the partial etching of the Si-δ layer leads to a lower doping. The effect of nearer surface (bottoms of holes) and of its surface states is also considered. In summary, three samples from different wafers were probed and in each of them a serious decrease of concentration was observed, as table 4.3 reports. Concerning optical samples, the etching could create the same depletion (non suitable for FIR experiments) and thus we had to increase the density by illumination.

Focusing on the second accessible parameter, at zero magnetic field the mobility of 2DEG layer can be expressed as

$$\mu = R_H \sigma = \frac{1}{ne} \frac{I_{xx}}{U_{xx}} \frac{l}{d} \tag{4.15}$$

where l is the distance of longitudinal Hall bar contacts and d the width of Hall bar. Regarding the data in figure 4.10, we immediately see that the mobility has decreased since at $B = 0$ the R_{xx} increased more than twice but the concentration decreased only by small tens of percents. In the same way, we present table 4.4 summarizing results. The transport method of determination (upper part) nicely match with the determination from spectral shape made for optical samples (bottom part). In all cases, the decrease of mobility was around 30%. This fact directly states that the mobility in optical sample should be high enough to fulfill the criterion 4 ($\mu \sim 10^5$ cm^2/Vs, section 2.4).

Sample	μ_{etch} ($\times 10^6$ cm^2/Vs)	μ_{orig}	fall	h_{dots}/2DEG (nm)
1E2	0.7	1.8	61%	80/210
1E5	0.6	1.3	53%	100/210
A, B	0.13–0.2	?	–	20-25/100
C	0.1	0.5	80%	48/115

Table 4.4: Fall in mobility before and after the patterning. As can be seen, the etching produces a considerable decrease of mobility. In this meaning, a gated needle electrode can provide better samples since it does not affect the sample surface and neither its volume.

Unfortunately, we cannot conclude that the performed transport measurement showed any non-standard behaviour that could have been interpreted as an effect of the superlattice (or Dirac fermions). Although presented samples were not carefully designed especially for the purpose of "artificial graphene" measurement, even a slight perturbation would have been highly motivating. In all three hole-patterned sample, there was no special evidence of such behaviour (as presented in FIR experiments). However, the constitution of these samples was considerably different – the depth of 2DEG was 210 nm and the contacting process was not ideal (many of contacts broke down and were not usable). One can rationally hope that using the special needle-electrode designed samples, now in preparation, will bring more pleasant results.

Conclusions

The Master thesis covers three steps necessary to realize artificial graphene – the theoretical estimates and prognosis, technological preparation of samples, and finally, the experiments aimed at direct demonstration of massless Dirac fermions, possibly created in the system. In such terms, the thesis represents a comprehensive report on artificial graphene ideas developed by author, his supervisor, advisor and other team members mentioned in acknowledgments. It introduces, in summary, the reader into first steps on far-from-easy way towards artificial graphene.

In the theoretical part, devoted to finding numerical estimates of basic technological parameters, we studied the creation of Dirac cones and Dirac fermions in classical 2DEG perturbed by a hexagonal lateral potential. Two Dirac cones were found in lowest six minibands, whereof the second one performs more favourable dimensions and energy position. The true Dirac nature of both of them was demonstrated by the evolution of their eigen-functions in the first Brillouin zone and by other numerical methods. The effective radius of Dirac cones was estimated as $1/5 - 1/3$ of "the radius of first Brillouin zone", thus of the distance $|\Gamma K|$. This fact leads to the request for more than 1 meV precision in the adjusting of the Fermi level. Finally, the theoretical work formulated four crucial criteria for technologists and experimentalists – the parameter ζ (connected to the value of potential V_0) has to be set in ranges $0.5 - 4.0$, or better in a narrower range $0.7 - 1.0$ with the concentration about $n \approx 7 \times 10^{10}$ cm^{-2}. The most demanding, in our case, was the criterion 4 that calls for very low magnetic field, which prints towards low energies of probing light and low temperatures.

The technology of the preparation was described in details and contains all necessary parameters and used methods. Besides the fabrication of optical or transport samples, based on dry etching of holes in hexagonal symmetry, other used or still designing devices were presented. The most sophisticated one, the concept of needle-shaped electrode gated over a classical Hall bar geometry, was shown and several technological troubles were indicated. According to the main sense of this chapter, we hope that mentioned information can help other fighters in the field of artificial graphene.

Concerning the experiments, three concepts of measurements were done – the far infrared spectroscopy and photoluminescence in magnetic field and low temperatures electronic transport measurements. Results, providing by main FIR experiments, show a non-conventional phenomenon, nevertheless they assertively suggest that we have broken the fourth criterion – we work in too high energies. Notwithstanding that other sample parameters match well or are not far from the requested values, we have to, unfortunately, state that no direct signature of Dirac fermions was observed. However, the results were used to find an important correlation. Since the effect of superlattice was weak compared to Landau level quantization (too high energies and magnetic field), we used a perturbation theory to explain the observed deviations. Thanks to it, we found the correlation between the depth of etched holes and the effective potential V_0, created in such way in the 2DEG layer. As realized during measurements in Pisa, other teams in world are solving the very similar problems – so that we hope this will be considerably

useful for our colleagues.

The possible future work will be certainly connected with needle electrode concept presented in the second chapter. Such a proposal combines many advantages, as is the continuous control of two crucial parameters, ζ and V_0, during transport experiments. Of course, the cost of these positive aspects is just the complicated fabrication of the electrode – but on the other hand, it might lead to significant discoveries.

As met during presentations of our work, there are fair critics of the artificial graphene concept. Some of them simply look at the theme as at an eye-taking, stylish or fashionable topic only, but a few of them see the inner conflict – the disagreement between the simplicity and closeness-to-human of graphene and the sophisticated, unimaginably precise processing of artificial graphene. In case of artificial graphene, I completely agree that the use of the tempting motivation, originated from natural graphene, causes something uneasy to solve. However, if the work provokes questions concerning the relation between the natural and the artificial, nature and technology, or originality (tradition) and change (modernity), I am glad to contribute.

Bibliography

[1] A. H. Castro Neto, F. Guinea, N. M. R. Peres, K. S. Novoselov, and A. K. Geim, Rev. Mod. Phys. **81**, 109 (2009).

[2] M. Orlita and M. Potemski, Semicond. Sci. Technol. **25**, 063001 (2010).

[3] S. Bae, H. Kim, Y. Lee, X. Xu, J.-S. Park, Y. Zheng et al., Nature Nanotechnology **5**, 574 (2010).

[4] Ch.-H. Park and S. G. Louie, Nano Lett. **9**, 1793 (2009).

[5] X. F.Wang, P. Vasilopoulos, and F. M. Peeters, Phys. Rev. B **69**, 035331 (2004).

[6] A. Bermudez, N. Goldman, A. Kubasiak, M. Lewenstein, and M. A. Martin-Delgado, New J. Phys. **12**, 033041 (2010).

[7] B. Wunsch, F. Guinea, and F. Sols, New J. Phys. **10**, 103027 (2008).

[8] W. Zhang, P. Zhang, S. Duan, and X.-g. Zhao, New. J. Phys. **11**, 063032 (2009).

[9] M. Gibertini, A. Singha, V. Pellegrini, M. Polini, G. Vignale, A. Pinczuk, L. N. Pfeiffer, and K. W. West, Phys. Rev. B **79**, 241406 (2009).

[10] G. de Simoni, A. Singha, M. Gibertini, B. Karmakar, M. Polini, V. Piazza, L. N. Pfeiffer, K. W. West, F. Beltram, and V. Pellegrini, Appl. Phys. Lett. **97**, 132113 (2010).

[11] A. Singha, M. Gibertini, B. Karmakar, S. Yuan, M. Polini, G. Vignale, M. I. Katsnelson, A. Pinczuk, L. N. Pfeiffer, K. W. West, and V. Pellegrini, Science **332**, 1176–1179 (2011).

[12] L. Nádvorník, Optická spektroskopie grafenových multivrstev v magnetickém poli, Bachelor thesis, Faculty of Mathematics and Physics of Charles University, Prague (2009).

[13] P. R. Wallace, Phys. Rev. **71**, 622 (1947).

[14] A. K. Geim and K. S. Novoselov, Nature Materials **6**, 182 (2007).

[15] M. L. Sadowski, G. Martinez, M. Potemski, C. Berger and W. A. de Heer, Phys. Rev. Lett. **97**, 266405 (2006).

[16] K. v. Klitzing, G. Dorda and M. Pepper, Phys. Rev. Lett. **45**, 494 (1980).

[17] D. C. Tsui, H. L. Stormer and A. C. Gossard, Phys. Rev. Lett. **48**, 1559 (1982).

[18] K. S. Novoselov, A. K. Geim, S. V. Morozov, D. Jiang, M. I. Katsnelson, I. V. Grigorieva, S. V. Dubonos and A. A. Firsov, Nature **438**, 197 (2005).

[19] L. Nádvorník, M. Orlita, N. A. Goncharuk, L. Smrčka, V. Novák, V. Jurka, K. Hruška, Z. Výborný, Z. R. Wasilewski, M. Potemski, and K. Výborný, Arxiv:1104.5427 (2011).

[20] I. S. Gradshteyn and I. M. Ryzhik, Table of Integrals, Series, and Products, Academic, New York, (1980).

[21] V. Y. Demikhovskii and A. A. Perov, J. Exp. and Theor. Phys. **87**, 973 (1998).

[22] O. M. Fedorych, S. A. Studenikin, S. Moreau, M. Potemski, T. Saku, and Y. Hirayama, Int. J. Mod. Phys. B **23**, 2698 (2009).

[23] F. Stern, Phys. Rev. Lett. **18**, 14 (1967).

[24] S. A. Mikhailov, Phys. Rev. B **70**, 165311 (2004).

[25] S. A. Mikhailov and N. A. Savostianova, Phys. Rev. B **71**, 035320 (2005).

[26] M. Byszewski, Optical properties of a two-dimensional electron gas in magnetic fields, Ph.D. thesis, Université Joseph Fourier, Grenoble (2005).

[27] K. W. Chiu, T. K. Lee, and J. J. Quinn, Surface Science **58**, 182 (1976).

List of Figures

List of Tables

A. Estimate of concentration and mobilities

The method how to calculate the electron density in 2DEG according to its FIR transmission spectrum [27], assumes a 2DEG layer with conductivity σ, enfolded between two same materials with permittivity ε. The wave equation on boundary at $z = 0$ is

$$\frac{\partial^2 E}{\partial z^2} - \frac{1}{c^2}\frac{\partial^2 E}{\partial t^2} - \frac{\sigma}{\varepsilon c^2}\frac{\partial E}{\partial t} = 0. \tag{A.1}$$

Assuming the the incident light in form $\exp i\omega t$, we obtain

$$\frac{\partial^2 E}{\partial z^2} + \frac{1}{c^2}\omega^2 E + i\omega\frac{1}{\varepsilon c^2} j\delta(z) = 0. \tag{A.2}$$

At $z \neq 0$, the solution for the incident light $E_i(r,t) = E_i \exp(ikz - i\omega t)$ and for reflected one $E_r(r,t) = E_r \exp(-ikz - i\omega t)$, for $z < 0$, and the transmitted light $E_t(r,t) = E_t \exp(ikz - i\omega t)$, for $z > 0$.

From the boundary conditions at $z = 0$ [27], we find the transmission coefficient $t = E_t/E_i$ as follows

$$t_\pm = \frac{1}{1 + \frac{\sigma_\pm}{2\tilde{n}\varepsilon_0 c}} \tag{A.3}$$

where $\tilde{n}$ is refractive index of the material and $\sigma_\pm$ originates from circularly polarized coordinates describing $j_\pm = j_x + ij_y = \sigma_\pm(E_x + iE_y) = \sigma_\pm E_\pm$. According to semi-classical Drude model, we express the conductivity

$$\sigma_\pm \approx \sigma_0 \frac{1}{1 + i\tau(\omega - \omega_c)}. \tag{A.4}$$

where $\sigma_0 = \frac{ne^2\tau}{m^*}$. Now, for a detector insensitive to polarization of radiation we write the transmittance for linearly polarized light

$$T = \frac{1}{2}(|t_+|^2 + |t_-|^2). \tag{A.5}$$

Since we measured cyclotron resonance absorption, only one circular polarization can be absorbed – the other one is transmitted nearly completely, thus $|t_-|^2 \approx 1$. Applying the expansion to power series $\frac{1}{1+x} \approx 1 - x$ on equation A.3, we obtain

$$\begin{aligned} &|t_+|^2 \approx |1 - \tfrac{\sigma_+}{2\tilde{n}\varepsilon_0 c}|^2 = \\ &= \left(1 - \tfrac{\sigma_0}{2\tilde{n}\varepsilon_0 c}\tfrac{1}{1+\tau^2(\omega-\omega_c)^2}\right)^2 + \left(\tfrac{\sigma_0}{2\tilde{n}\varepsilon_0 c}\tfrac{\tau(\omega-\omega_c)}{1+\tau^2(\omega-\omega_c)^2}\right)^2 \end{aligned} \tag{A.6}$$

Since we work in approach of weak absorption, thus the term $\frac{\sigma_0}{2\tilde{n}\varepsilon_0 c}$ is considerably smaller than 1, we neglect all quadratic terms in equation A.6 and hence, we get

$$|t_+|^2 \approx 1 - \frac{\sigma_0}{\tilde{n}\varepsilon_0 c}\frac{1}{1 + \tau^2(\omega - \omega_c)^2}. \tag{A.7}$$

Equation A.5 then leads to

$$T = 1 - \frac{e^2 n\tau}{2\tilde{n}\varepsilon_0 c m^*}\frac{1}{1 + \tau^2(\omega - \omega_c)^2}. \tag{A.8}$$

In equation A.8, there are only two unknown variables: electron density n and mean life time τ. The equation has already form convenient for two parametric fitting of Lorentzian peaks in FIR spectra. Since the mobility is often written as $\mu = e\tau/m^*$, the presented method provide us both parameters n and μ necessary for the sample characterization upon experimental conditions.

B. Eigenfunction evolution in first BZ

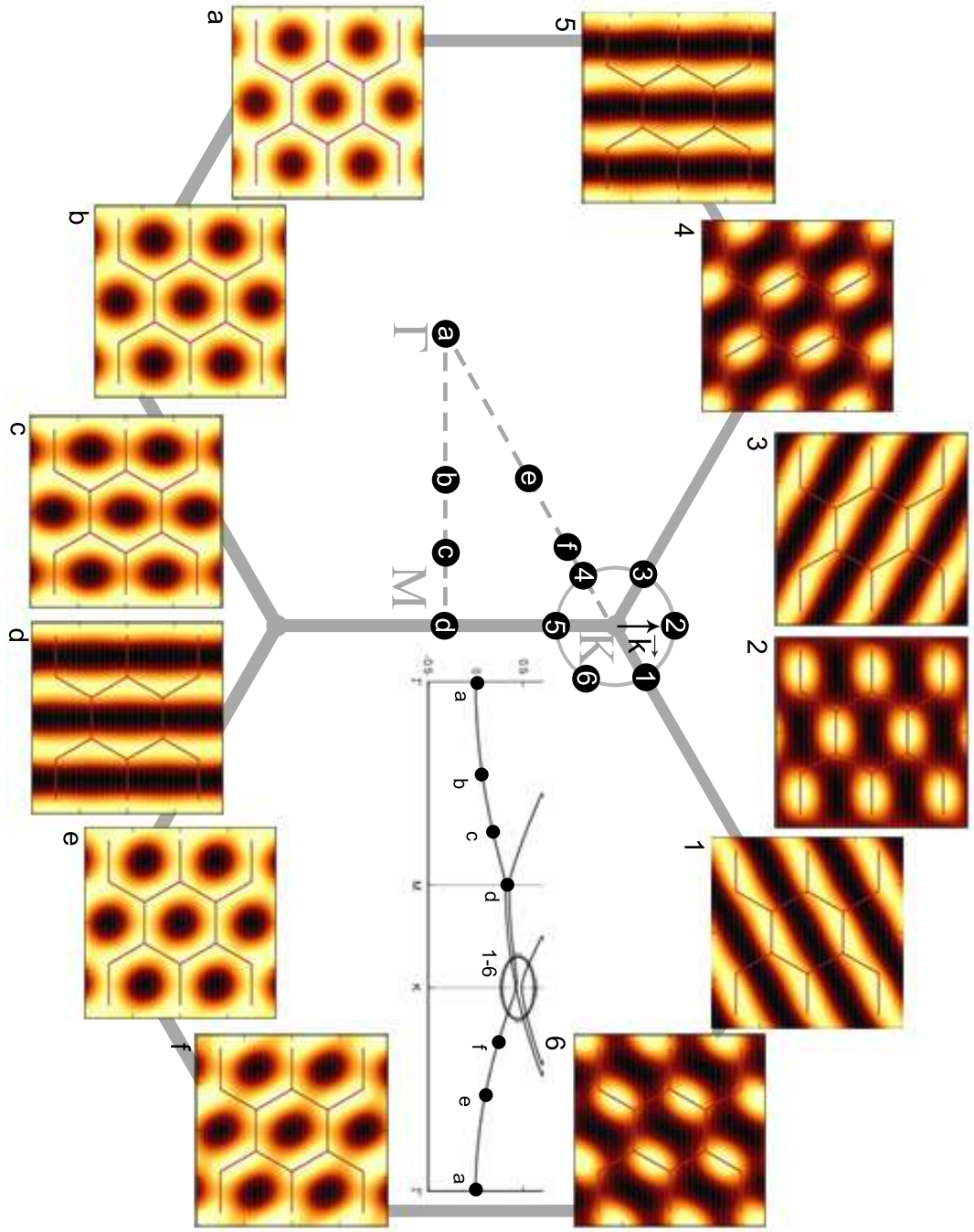

C. Towards artificial graphene (paper)

TOWARDS ARTIFICIAL GRAPHENE

L. Nádvorník, M. Orlita, N. A. Goncharuk, L. Smrčka, V. Novák, V. Jurka, K. Hruška, Z. Výborný, Z. R. Wasilewski, M. Potemski, and K. Výborný

Towards engineering artificial graphene

L. Nádvorník,[1,2,*] M. Orlita,[3,2,1] N. A. Goncharuk,[2] L. Smrčka,[2] V. Novák,[2] V. Jurka,[2]
K. Hruška,[2] Z. Výborný,[2] Z. R. Wasilewski,[4] M. Potemski,[3] and K. Výborný[2,5]

[1] *Faculty of Mathematics and Physics, Charles University, Ke Karlovu 3, 121 16 Praha 2, Czech republic*
[2] *Institute of Physics, ASCR, v.v.i., Cukrovarnická 10, 162 53 Praha 6, Czech Republic*
[3] *Laboratoire National des Champs Magnétiques Intenses, CNRS-UJF-UPS-INSA, 25, avenue des Martyrs, 38042 Grenoble, France*
[4] *Institute for Microstructural Sciences, NRC, Ottawa, Ontario, Canada K1A 0R6*
[5] *Department of Physics, State University of New York at Buffalo, New York 142 60, USA*

We report on a measured non-linear in magnetic field dependence of cyclotron resonance absorption as well as its splitting into several modes in GaAs/Al_xGa_{1-x}As heterostructures with an etched hexagonal lateral superlattice, i.e., in artificial graphene. Our explanation, based on the perturbation theory, describes the observed phenomena as a weak effect of the lateral potential on the two-dimensional electron gas (2DEG). In addition, we propose a set of four criteria that one has to satisfy to realize graphene-like physics in materials containing 2DEG with a tunable hexagonal modulation.

PACS numbers: 73.22.Pr, 73.21.Cd, 78.67.Pt

I. INTRODUCTION

The range of paths to explore Dirac fermions has recently been (once again) extended beyond the standard field of graphene[1,2] to a completely new class of systems. The artificial graphene (AG) concept is based on the idea of creating massless fermions in semiconductor heterostructures by modulating the two-dimensional electron gas (2DEG) with a lithographically created superlattice. If the introduced potential reflects the hexagonal symmetry of natural graphene and it is strong enough, the electronic structure changes towards a graphene-like one.[3,4] A lateral modulation of the surface by etching[5–7] or by placing a gate electrode represent two possible techniques. Lithographical fabrication offers more freedom in creating artificial crystals than preparation of structures from real atoms and consequently the electronic properties of the AG, such as the slope of the Dirac cone (that is the Fermi velocity), can be widely tuned.[8] Moreover, various proof-of-principle device prototypes[9] (filters, valves,[10] Veselago lens,[11] splitters[12] etc.) could be more easily tested on AG basis owing to the larger versatility of electron beam lithography compared to an atom-by-atom manipulation required for fabrication of natural graphene devices. In the present work, with help of a simplified AG model, we first formulate four basic criteria to make graphene-like characteristics observable and then show how they can be tested using magneto-optical experiments. We conclude that AG with the desired hallmarks of Dirac-fermions may be technologically attainable but their actual observation is missing so far.

II. THEORY

Compared to previous works,[4,8] we use a simplified AG model that allows for a better insight into how the individual parameters of the modulation potential $V(\vec{r})$, $\vec{r} = (x, y)$ govern the miniband structure. We consider V comprising of three cosine functions

$$V(\vec{r}) = V_0(\cos \vec{g_1}\vec{r} + \cos \vec{g_2}\vec{r} + \cos \vec{g_3}\vec{r}), \qquad (1)$$

where $\vec{g_1} = 2\pi/a(1/\sqrt{3}, 1)$, $\vec{g_2} = 2\pi/a(2/\sqrt{3}, 0)$, $\vec{g_3} = \vec{g_2} - \vec{g_1}$ are the basis-vectors of the graphene reciprocal space, a is the distance between two minima of the applied potential [Fig. 1(a)] and V_0 is the potential amplitude. If we construct the Hamiltonian matrix in basis $\mathcal{B}$ of plain waves,

$$\mathcal{B} = \left\{ e^{i(\vec{k}+\vec{K}_{n_1 n_2})\vec{r}},\ \vec{K}_{n_1 n_2} = n_1\vec{g}_1 + n_2\vec{g}_2 \right\}, \qquad (2)$$

the ratio of diagonal to off-diagonal matrix elements is determined by V_0 and a. Except for an overall scaling, the eigenvalues depend on a single dimensionless parameter

$$\zeta = \frac{m^*}{h^2} V_0 a^2, \qquad (3)$$

where m^* is the electron effective mass (in GaAs, 0.067 of the electron vacuum mass m_0). Up to a factor of the order of unity, it is $\zeta \simeq V_0/E_0$ where E_0 is the kinetic energy of a free electron at the K-point of the Brillouin zone.

Depending on ζ, we obtain miniband spectra continuously varying from the free 2DEG, through nearly-free and tight-binding models, up to completely flat bands corresponding to isolated (artificial) atoms. We point out that *two* Dirac cones can be found (within the lowest six minibands, see Fig. 2(b),(c) with Fermi velocities $v_F = 2.4 \times 10^4$ and 4.8×10^4 m.s^{-1} when $a = 200$ nm. Both Dirac cones were numerically explored and their Dirac-fermion-like nature was confirmed in terms of spectral properties (cone-like character with trigonal warping) and wavefunctions.[4] Maximum Dirac cones size is of the order of E_0. Further quantitative studies of the

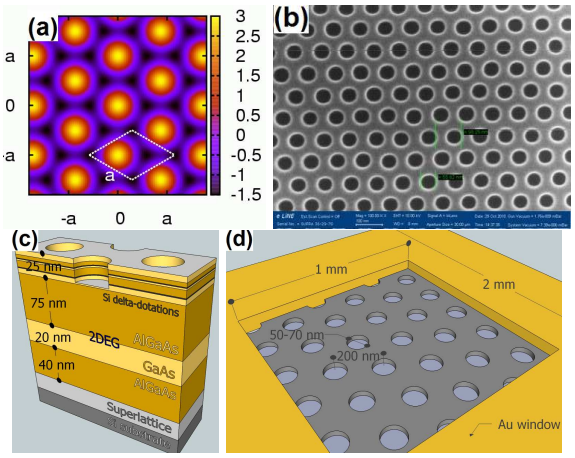

FIG. 1. (color online) Artificial graphene: Part (a): hexagonal potential of Eq. (1) defining the AG (in units of V_0). Dark regions correspond to "atom positions" in the real graphene; the primitive cell is indicated. (b): Scanning electron microscope image of the surface of one of the samples, (c): its atomic layer structure (2DEG depth ≈ 100 nm) and (d): the sample layout (not at scale).

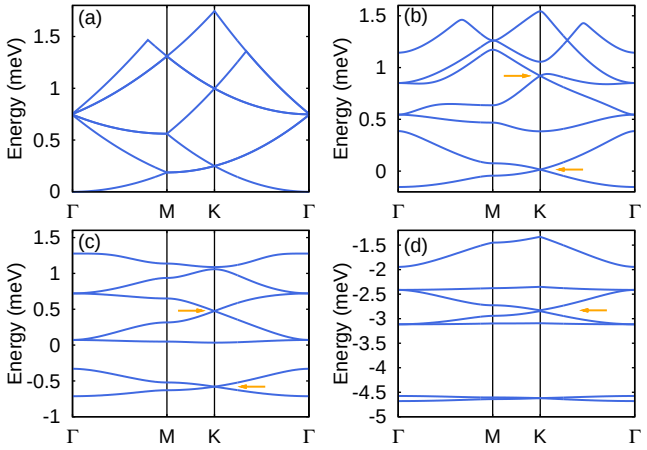

FIG. 2. (color online) Minibands generated for several values of the parameter ζ. (a): $\zeta = 0$, dispersion of a free 2DEG. (b): $\zeta = 0.3$, first Dirac cones develops (indicated by arrow), the second one appears but remains covered by other bands. (c): $\zeta = 0.9$, both Dirac cones fully develop. (d): $\zeta = 4.0$, tight-binding type narrow minibands form and Dirac cones gradually flatten, ultimately becoming again unobservable. For $a = 200$ nm, a,b,c, and d correspond to $V_0 = 0$, 0.4, 1 and 4 meV in GaAs.

Dirac cones characteristics seem of less use with regard to the simplicity of the model; in the following we show how it, nevertheless, can be employed as a guide for AG fabrication.

Four criteria shall now be stated necessary to observation of graphene-like physics in AG. (i) *Suitable miniband structure* — looking at Fig. 2, the obvious first criterion is to appropriately adjust the ζ parameter lest the desired Dirac cones be not "covered" by other branches of the miniband structure. For the second Dirac cone, we find the range $0.5 < \zeta < 4.0$ corresponding to V_0 between 0.6 and 4.5 meV (for $a = 200$ nm as in our samples described below). (ii) *Fermi level positioning* – to observe graphene-like properties, the Fermi level, E_F, should cross the linear part of the spectrum. Estimated values of E_F for the first and second Dirac cones for $\zeta = 0.9$ are 0.15 and 1.2 meV approximately corresponding to carrier concentrations $n \approx 0.5 \times 10^{10}$ and 3.3×10^{10} cm^{-2}, respectively, and for $\zeta = 4$ then $n \approx 6 \times 10^{10}$ cm^{-2} (see Appendix A), suggesting that the second Dirac cone would be better accessible from technological point of view. Although the first Dirac cone develops already for smaller V_0 it would force the experimentalist to work at too low n. If a is reduced with ζ remaining the same, the system offers somehow more favourable perspectives: $\zeta = 0.9$, $V_0 = 4$ meV and $a = 100$ nm implies $n \approx 1.7 \times 10^{10}$ and $n \approx 1.4 \times 10^{11}$ cm^{-2}, for the first and second Dirac cone, and the identical shape of minibands (including the Dirac cones) as in Fig. 2(c), only moved to higher energies. (iii) *Low disorder* – the idealized miniband structure, as suggested in Fig. 2, will be smeared by various irregularities of the system: both by impurities present in the unmodulated heterostructure and imperfections of the modulation potential. The minimal requirement to meet is that the mean free path $l_e = \hbar\mu\sqrt{2\pi n/e^2} \gg a$. This criterion is not too stringent since $l_e \approx 500$ nm for $\mu = 10^5$ cm^2/(V.s) and $n = 10^{11}$ cm^{-2} but it only constitutes a necessary and not a sufficient condition for tracing AG physics. (iv) *Careful probing* – the last important aspect is that the measurement conditions must not affect too strongly the AG system. Typically, this means that both the temperature, T, and magnetic field, B, are low enough. To preserve graphene-like behaviour, the system has to be governed by the modulation potential, and the cyclotron quantization has to play only the role of a scanning means. Hence, $\hbar\omega_c \ll E_{DC}$ with E_{DC} denoting the Dirac cone size in energy, and since the cyclotron energy $\hbar\omega_c = \hbar eB/m^*$ equals ~ 1.7 meV at $B = 1$ T, the quest for Dirac fermions in AG should aim at relatively weak magnetic field. Miniband structures in Fig. 2 show $E_{DC} \sim 0.3$ meV (note that a good general estimate of E_{DC} is E_0) therefore tolerable magnetic fields are hundreds of mT at the most. Similarly, to keep $kT \ll \hbar\omega_c$, temperatures in sub-kelvin range may be needed.

III. EXPERIMENT

To create the required type of potential on the surface of our samples, we fabricated a pattern formed by holes in triangular symmetry, etched into material. Electron beam lithography and dry etching processes (Ar^+ + $SiCl_4$) were used to obtain the three samples under study (A, B and C, see Table I) which have holes etched to 15-25, 20 and 48 nm in depth. The diameter of

holes was always 50-70 nm and nearest-neighbour distance $a = 200$ nm. Two types of GaAs/AlGaAs heterostructures have been used as a starting material: the first one for the samples A and B, containing a 100 nm deep 2DEG formed in the 20 nm wide quantum well and charged by two Si delta-doped layers, 14 nm and 24 nm under the surface (Fig. 1(c); the second one for the sample C, which consists of the 115 nm deep 2DEG confined in a triangular quantum well under one 50 nm wide Si-doped layer. Modulated areas were covered by a 50 nm thin layer of gold with a 1×1 mm^2 window [Fig. 1(d)].

The samples were placed into a helium-pumped cryostat at $T = 2$ K, equipped with a superconducting coil producing the magnetic field up to 13 T. The Fourier transform spectrometer working down to photon energies of $\hbar\omega \approx 4$ meV, with a globar and mercury lamp as the radiation sources, was coupled to the cryostat. The signal was detected using bolometer kept at $T = 2$ K. Transmission spectra have been collected with resolutions down to 0.125 meV. The initial concentration of carriers in samples before processing was changed as a result of etching as well as of illumination by visible parts of globar/mercury lamp emission spectra. Therefore, the actual concentration has been finally estimated from area of CR peak as $n_{A,B} \sim 0.8\times10^{11}$ cm^{-2} and $n_C \sim 1.8\times10^{11}$ cm^{-2} (see Appendix A for details). The carrier mobility after processing was estimated to be somewhat in excess of 10^5 cm^2/(V.s) for all three samples and similar mobilities were inferred also from magneto-transport measurements on samples parent to C.

The electronic bands in our samples have been studied using methods of Landau level (LL) spectroscopy in far infrared spectral range. The magneto-transmission spectra of a set of three patterned samples and one reference sample have been measured. In Fig. 3, typical spectra, i.e., the transmission of the samples normalized to the response at $B = 0$, are presented for fields $B = 3-7.5$ T. Transmission spectrum measured on the reference sample (an unpatterned wafer, the same as used for samples A and B) exhibited only a single cyclotron-resonance (CR) mode of the Lorentzian shape having energy of $\hbar\omega_c$. As shown in Figs. 3a-c, the transmission spectra measured on the patterned samples exhibit double- or multi-mode CR response at low magnetic fields. Characteristically, these additional modes appears at energies above $\hbar\omega_c$. This splitting of the CR mode into more components vanishes with the increasing B, but at different fields in different samples, i.e., this splitting depends on the strength of the modulation potential or the depth of etched holes. For stronger modulation potential (deeper holes), the multi-mode CR is visible up to higher magnetic fields (see Fig. 4).

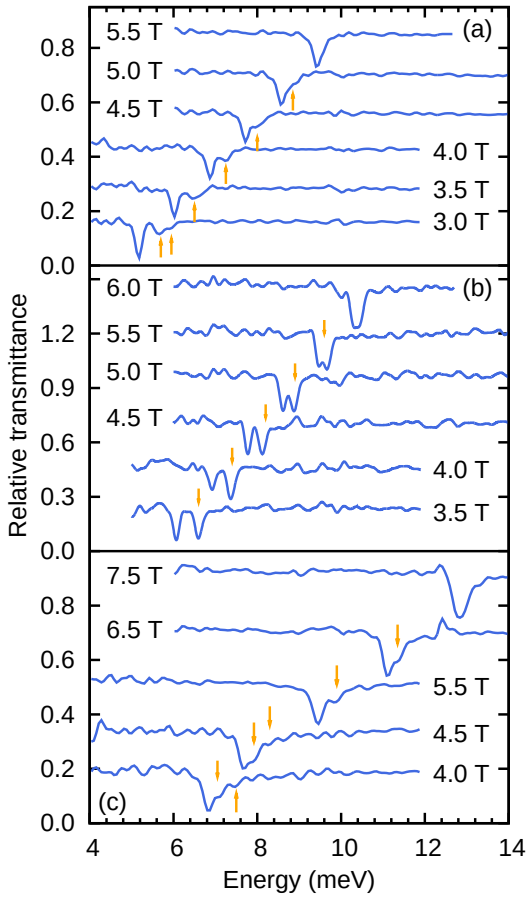

FIG. 3. (color online) Relative magneto-transmission spectra of studied samples A ($d_{\rm holes} \approx 15-25$ nm, $d_{\rm 2DEG} = 100$ nm), B ($d_{\rm holes} = 20$ nm, $d_{\rm 2DEG} = 100$ nm) and C ($d_{\rm holes} = 48$ nm, $d_{\rm 2DEG} = 115$ nm) in parts (a), (b) and (c), respectively. The multi-mode character of cyclotron resonance absorption vanishes with the increasing magnetic field at $B \approx 5, 6$ and 7 T in the sample A, B and C, respectively. All spectra are shifted vertically for clarity.

INTERPRETATION

The question raised now is what we can learn from present experiment and whether signatures of Dirac bands have been observed or how far are we from their observation. As can be sen in Fig. 3, the patterned structures show noticeably modified spectra, but observed changes are not as dramatic as we could, even intuitively, expect in case of a clear formation of Dirac-like electronic bands. The modulation potential seems to be not strong enough to incite Bloch waves mimicking Dirac-fermion physics. Main absorption features still occur close to $\hbar\omega_c$ but in contrast to the cyclotron peak of the unmodulated 2DEG, they exhibit internal structure which disappears roughly as $1/B$ (see Fig. 4) in the limit of high magnetic fields. Such behavior is suggestive of a perturbative effect of a potential whose strength becomes gradually weaker relative to the spacing of LLs. This spacing, the cyclotron energy $\hbar\omega_c$, then provides the dominant energy scale and the modulation potential V_0 is only a perturbation described by the small parameter $V_0/\hbar\omega_c$. Data

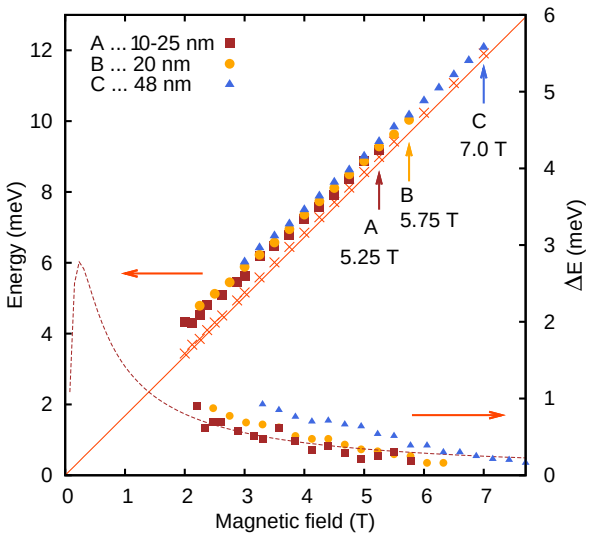

FIG. 4. (color online) Fanchart of transitions observed in studied specimens A, B and C, cf. Fig. 3 (left vertical axis): Vertical arrows depict magnetic fields at which the multimode character of CR absorption vanishes. The position of the main CR peak in spectra taken on the sample A is marked by crosses. The straight line corresponds to the theoretical CR-line position with an effective mass of $m^* = 0.067m_0$, which has been derived from measurements on reference (unpatterned) sample (not shown in this paper). Lower part of the figure (right vertical axis) shows derived values of CR-line splitting ΔE. The dashed line corresponds to the fit of ΔE for the sample A based on the theoretical model discussed in the text.

presented in Fig. 3 therefore bear witness to an overly strong effect of magnetic field that almost washes up the effect of the modulation potential and, similar to previous works, e.g., Ref. 8, we fail to observe graphene-like behavior on grounds of violating the forth criterion (as defined in Sec. II).

To remedy this shortcoming, measurements at lower magnetic fields are needed. This is in principle possible yet beyond the low-energy limit of the employed Fourier transform spectroscopy. Still, we can draw conclusions from our experiments regarding the first two criteria described in Sec. II. This way we first find how our samples need to be optimized in the future and second, what maximum magnetic fields can be employed for studying the projected graphene features. According to the first-order perturbation approach,[14] the unperturbed energies $E_n = \hbar\omega_c(n+1/2)$ are broadened into bands

$$E_{n,\kappa_x,\kappa_y} = E_n + V_0 e^{-2\beta^2/3} L_n(4\beta^2/3)\times \\ \times\left\{2\cos\beta^2(\kappa_x+\tfrac{1}{\sqrt{3}})\cos\tfrac{\beta^2\kappa_y}{\sqrt{3}} + \cos\tfrac{2\beta^2\kappa_y}{\sqrt{3}}\right\} \quad (4)$$

where $\beta^2 = 2\pi^2\ell_0^2/a^2$, $\ell_0^2 = \hbar/eB$ and $\vec{\kappa}$ belongs to the hexagonal first magnetic Brillouin zone. Owing to special properties of Laguerre polynomials L_n,[15] optical transition energies, that are $E_{n+1,\kappa_x,\kappa_y} - E_{n,\kappa_x,\kappa_y}$, can be rewritten in a simple way. Since we deal with low carrier concentrations at which only the lowest LL is occupied, we can restrain ourselves to $n = 0$,

$$\Delta E_{1,0} = E_{1,\kappa_x,\kappa_y} - E_{0,\kappa_x,\kappa_y} = \hbar\omega_c - \frac{4}{3}V_0\beta^2 e^{-2\beta^2/3} b(\kappa_x,\kappa_y) \quad (5)$$

where $b(\kappa_x,\kappa_y)$ denotes the curled bracket of Eq. (4).

The optical transition energy $\Delta E_{1,0}$ enters the absorption probability $\alpha(\omega)$ at a photon frequency ω, see, e.g., Ref. 16, upon a transition between $n = 0$ and $n = 1$ LLs measured in our experiments

$$\alpha_{1,0} = \frac{2\pi}{\hbar}\int\frac{d^2\kappa}{(2\pi)^2}|\langle 1,\kappa_x,\kappa_y|p_x|0,\kappa_x,\kappa_y\rangle|^2\delta(\Delta E_{1,0}-\hbar\omega). \quad (6)$$

If we neglect the dipole transition matrix element for the moment, the characteristics spectral features corresponds to the van Hove singularities, see Fig. 5, in the the joint density of states (jDOS):

$$a(\omega) = \int\frac{d^2\kappa}{(2\pi)^2}\delta(\Delta E_{1,0}-\hbar\omega) f_{0,\kappa_x,\kappa_y}(1-f_{1,\kappa_x,\kappa_y}),$$

in which all those transitions at a given energy $\hbar\omega = \Delta E_{1,0}$ count where the initial ($n = 0$) state is occupied and the final ($n = 1$) state is empty, as expressed by the Fermi-Dirac occupation factors f. At a filling factor $\nu = nh/eB = 2$, which was assumed in Eq. (6), $a(\omega)$ is a band of the width

$$w(B) = 6V_0\beta^2 e^{-2\beta^2/3} \quad (7)$$

situated close to $\omega = \omega_c$. The width of the band decreases with decreasing ν, as the filling of the $n = 0$ LL decreases and smaller portions of the magnetic Brillouin zone become available for transitions. In the limit of very large B, $a(\omega)$ turns into a delta-peak at exactly $\omega = \omega_c$.

Eq. (7) provides a reasonable basis for interpretation of experimental data presented in Figs. 3(a)-(c). The peak-to-peak distance shown as the lower data sets in Fig. 4 follows the magnetic field dependence of $w(B)$ allowing to extract the values of V_0 for the particular sample. It should be noted that the peak splitting observed in experiments probably does not correspond to the full width w as calculated using Eq. (7) because the lower edge of

Sample	d_{holes}	d_{2DEG}	V_0	ζ
A	15-25	100	2.5 meV	2.4
B	20	100	3.5 meV	2.9
C	48	115	4 meV	4.0

TABLE I. Potential amplitude V_0 and the corresponding dimensionless parameter ζ for samples A, B and C as derived by fitting our data using Eq. (7), see text for details. The etching depths and the distances from 2DEG to the sample surface are also listed. Following relatively high ζ values, the lattice parameter reduced down to $a \approx 100$ nm would be more appropriate to achieve better defined Dirac cones for the given modulation strengths V_0, see Sec. II.

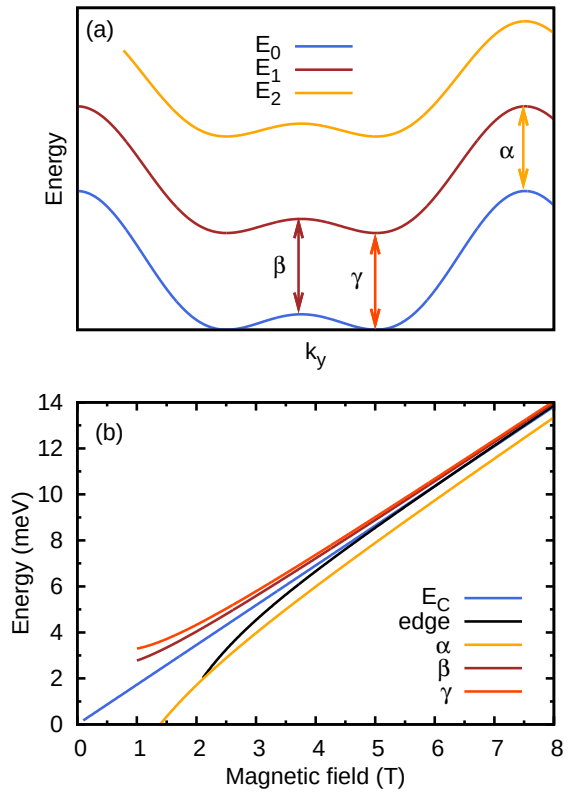

FIG. 5. (color online) Part (a): Schematic plot of three lowest lying LLs broadened into bands due to the lateral hexagonal modulation. Transitions originating in van Hove singularities in the joint density of states $a(\omega)$ are marked by α, β and γ. Whereas α and γ are the band edges, β is the logarithmic singularity corresponding to the saddle point between two neighbouring minima of ΔE_{10} in $\vec{\kappa}$-space (as shown in the top panel). Part (b): Magnetic field dependence of α, β, γ jDOS singularities. "Edge" shows the lowest in energy allowed transition, as defined by the position of the Fermi level (for $n = 5.0 \times 10^{10}$ cm^{-2}). $E_c = \hbar\omega_c$ is the cyclotron energy.

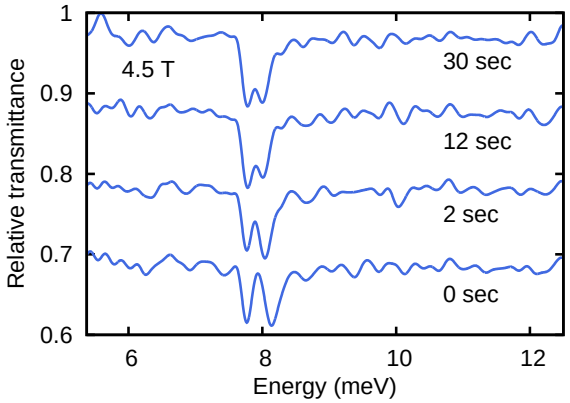

FIG. 6. (color online) Magneto-transmission spectra taken on the sample C at $B = 4.5$ T and four different carrier concentrations. The density has been subsequently increased by exposing the sample to visible light for the indicated times. The spacing of observed modes clearly decreases with the carrier density. The spectra are shifted vertically for clarity.

the absorption band is suppressed for $\nu < 2$ (this is the case of $B > 2$ T and $n < 10^{11}$cm^{-2}).

However, other features of the absorption band also scale as $cw(B)$, where $0 < c < 1$ is a constant. These features are shown in Fig. 5 and correspond to the indicated transitions of the broadened Landau bands E_{n,κ_x,κ_y}. The first states that become depopulated upon the filling factor dropping below two (that is when the magnetic field is increased) are those close to the top of the band. Hence, the transitions α are the first ones to disappear from the absorption spectra. We note that the Zeeman splitting ε_z is roughly $50\times$ lower than the LL broadening at $B = 2$ T, $\varepsilon_z = ge\hbar/2m_0B \approx 0.05$ meV.

For the remaining two features β and γ, our form of the potential $V(x, y)$ would imply $c = 1/9$. However, we believe that the feature β which leads to a logarithmic van Hove singularity in the jDOS, may be easily smeared out. Another candidate for an absorption feature is the Fermi edge (transitions from the states close to E_F to the next Landau band) which is also shown in the lower panel of Fig. 5. Although the Fermi edge does not precisely scale with $w(B)$, it always appears at frequencies $\omega \approx \omega_c$ hence $c \approx 1/3$. The values of V_0 inferred from fitting our data, assuming that the splitting of the CR mode corresponds to $\frac{1}{3}w(B)$, are shown in Tab. I alongside with the corresponding ζ.

Splitting of the cyclotron peak in diminishing magnetic fields shown in Fig. 3 is also reminiscent of confined magneto-plasmons (CMP),[17] and this circumstance motivated us to perform a control experiment that excludes the effect of CMP, as described below. An infinite system with the 2DEG at zero magnetic fields can sustain plasma oscillations[18] of wavelength $2\pi/q$ at frequency $\omega_p(q) = \sqrt{e^2nq/2m^*\varepsilon_r\varepsilon_0}$. Under the combined effect of the confinement and perpendicular magnetic field, the usual cyclotron resonance mode is experimentally found to shift from ω_c to higher frequencies $\sqrt{\omega_c^2 + \omega_p^2(q)}$; in a metallic stripe (quantum wire) of width W, the wavevector is given by $q = \pi/W$ (see references in Sec. III of Ref. 20). Numerical simulations based on classical electrodynamics[21] in fact show a whole series of CMP peaks at frequencies $\omega > \omega_c$ that correspond to integer multiples of the fundamental wave vector $q = \pi/W$.

Viewing our hexagonal modulation as (an array of) quantum wires with $W = a$ is, of course, a bold approximation, nevertheless, it can provide us with a rough estimation of the energy of the lowest confined magneto-plasmon mode:

$$\omega_{CPM} = \sqrt{\omega_c^2 + \frac{\pi e^2 n}{2m^* a\varepsilon_r\varepsilon_0}} \approx \omega_c + \frac{\pi en}{4Ba\varepsilon_r\varepsilon_0}. \qquad (8)$$

Taking $n \sim 2.5\times10^{10}$ cm^{-2}, i.e., the carrier density three times smaller than estimated above, we can reproduce

our experimental data surprisingly well. Nevertheless, this agreement is probably only incidental, as the concept of magneto-plasmons fails to explain experimental data in Fig. 6. Here we, using external illumination, varied the electron density in the sample C and observed a clear decrease of the splitting of modes with the increasing carrier concentration, which directly contradicts Eq. (8). In addition, one does not expect ω_{CMP} to change with the strength of the modulation, but just opposite behavior is clearly observed experimentally, see Fig. 4. We thus conclude that CMP do not underlie the observed splitting of the absorption peak.

CONCLUSION

In conclusion, we stated four basic criteria that need to be met in order to achieve the proposed graphene-like bands in modulated semiconductor heterostructures, and thus earn them the name *artificial graphene*. Splitting of the cyclotron resonance line observed in far infrared magneto-optical experiments on laterally patterned samples allowed us to estimate the strength of the modulation potential. We found that the samples under study may be close to meeting criteria (i-iii) formulated in Section II and in order to comply also with criterion (iv), much lower magnetic fields ($\sim$ 50 mT) and preferably also somewhat lower temperatures (below 1 K) should be employed. This criterion does not seem to be fulfilled (magnetic fields too high) in the most recent experiments[23] thereby postponing still the first observation of Dirac fermion physics in artificial graphene to (possibly not too distant) future.

ACKNOWLEDGEMENTS

The authors would like to sincerely thank P. Hubík and J. Čermák for technological assistance and J. Wunderlich for valuable critical remarks. Moreover, the support of the following institutions is acknowledged: the Ministry of Education of the Czech Republic projects LC510 and MSM0021620834, GAUK No. 250251, GACR No. P204/10/1020, the Academy of Sciences of the Czech Republic via Institutional Research Plan No. AV0Z10100521, GAAV contract KJB100100802, Fondation *NanoScience* via project Dispograph and Præmium Academiæ and last but not least, EC-EuroMagNetII under Contract No. 228043.

Appendix A: Carrier concentration

Theoretical estimates. For the criterion (ii) to be met, the carrier concentration n must be adjusted appropriately to match the Fermi energies of the first and second Dirac cones. Taking Fig. 2(c) as an example, $E_F - E_0 \approx 0.15$ and 1.2 meV, we estimate the carrier concentration quoted in the main text by $n \approx (E_F - E_0)m^*/\pi\hbar^2$ where $E_0 \approx -0.75$ meV is the bottom of the miniband structure. Strictly speaking, density of states belonging to the miniband structure will fluctuate around the free-2DEG value $m^*/\pi\hbar^2$ but it will only lead to corrections of the desired n that are small compared to the precision with which we can estimate n experimentally.

Experimental estimate. We assume that the 2D electron gas is embedded in between two insulating GaAs layers with a refractive index of $\tilde{n} \approx 3.0$ in the relevant spectral range. For a detector which is insensitive to polarization of radiation and high-quality sample ($\omega_c\tau \gg 1$), the transmittance is given by $T = \frac{1}{2}(|t_+|^2 + |t_-|^2)$, where $t_+ = 1/(1 + \sigma_+/2\tilde{n}\varepsilon_0 c)$ and $t_- \approx 1$, see, e.g., Refs. 19 and 22. If we remain in the limit of weak absorption, we obtain the sample transmission:

$$T \approx 1 - \frac{\mathrm{Re}\ \sigma_+}{2\tilde{n}\varepsilon_0 c} = 1 - \frac{e^2 n\tau}{2\tilde{n}\varepsilon_0 c m^*} \frac{1}{1 + \tau^2(\omega - \omega_c)^2},$$

in terms of optical conductivity σ_+, which allows us to easily estimate the carrier density n in the studied samples.

* nadvl@fzu.cz

[1] K. S. Novoselov, A. K. Geim, S. V. Morozov, D. Jiang, M. I. Katsnelson, I. V. Grigorieva, S. V. Dubonos, and A. A. Firsov Nature **438**, 197 (2005).
[2] A. K. Geim and K. S. Novoselov, Nature Mat. **6**, 183 (2007).
[3] B. Wunsch, F. Guinea, and F. Sols, New J. Phys. **10**, 103027 (2008).
[4] Ch.-H. Park, and S. G. Louie, Nano Lett. **9**, 1793 (2009).
[5] T. Ando, A. B Fowler, and F. Stern, Rev. Mod. Phys. **54**, 437 (1982).
[6] M. C. Geisler, S. Chowdhury, J. H. Smet, L. Höppel, V. Umansky, G. G. Gerhardts, and K. von Klitzing, Phys. Rev. B **72**, 045320 (2005).
[7] S. Hugger, T. Heinzel, and T. Thurn-Albrecht, Appl. Phys. Lett. **93**, 102110 (2008).
[8] M. Gibertini, A. Singha, V. Pellegrini, M. Polini, G. Vignale, A. Pinczuk, L. N. Pfeiffer, and K. W. West, Phys. Rev. B **79**, 241406 (2009).
[9] M.S.-M. Dubois, Z. Zanolli, X. Declerck, and J.-C. Charlier, Eur. Phys. J. B **72**, 1–24 (2009).
[10] A. Rycerz, J. Tworzydło, and W. J. Beenakker, Nature Phys. **3**, 172 (2007).
[11] V. V. Cheianov, V. Fal'ko, and B. L. Altshuler, Science **315**, 1252 (2007).
[12] J.-L. Garcia-Pomar, A. Cortijo, and M. Nieto-Vesperinas, Phys. Rev. Lett. **100**, 236801 (2008).

[13] G. De Simoni, A. Singha, M. Gibertini, B. Karmakar, M. Polini, V. Piazza, L. N. Pfeiffer, K. W. West, F. Beltram, and V. Pellegrini, Appl. Phys. Lett. **97**, 132113 (2010).
[14] X. F. Wang, P. Vasilopoulos, and F. M. Peeters, Phys. Rev. B **69**, 035331 (2004).
[15] I. S. Gradshteyn and I. M. Ryzhik, Table of Integrals, Series, and Products, Academic, New York, (1980).
[16] V. Y. Demikhovskii and A. A. Perov, J. of Exp. and Theor. Phys. **87**, 973 (1998).
[17] O. M. Fedorych, S. A. Studenikin, S. Moreau, M. Potemski, T. Saku, and Y. Hirayama, Int. J. of Mod. Phys. B **23**, 2698 (2009).
[18] F. Stern, Phys. Rev. Lett. **18**, 14 (1967).
[19] K. W. Chiu and T. K. Lee, Surface Science **58**, 182–184 (1976).
[20] S. A. Mikhailov, Phys. Rev. B **70**, 165311 (2004).
[21] S. A. Mikhailov and N. A. Savostianova, Phys. Rev. B **71**, 035320 (2005).
[22] M. L. Sadowski, G. Martinez, M. Potemski, C. Berger, and W. A. de Heer, Int. J. Mod. Phys. B **21**, 1145 (2007).
[23] G. de Simoni, A. Singha, M. Gibertini, B. Karmakar, M. Polini, V. Piazza, L. N. Pfeiffer, K. W. West, F. Beltram, and V. Pellegrini, Appl. Phys. Lett. **97**, 132113 (2010).